Master's Thesis

Katharina Theresa Scheidt

Modeling Paleotemperatures from Stable Nitrogen Isotopes with the Community Firn Model
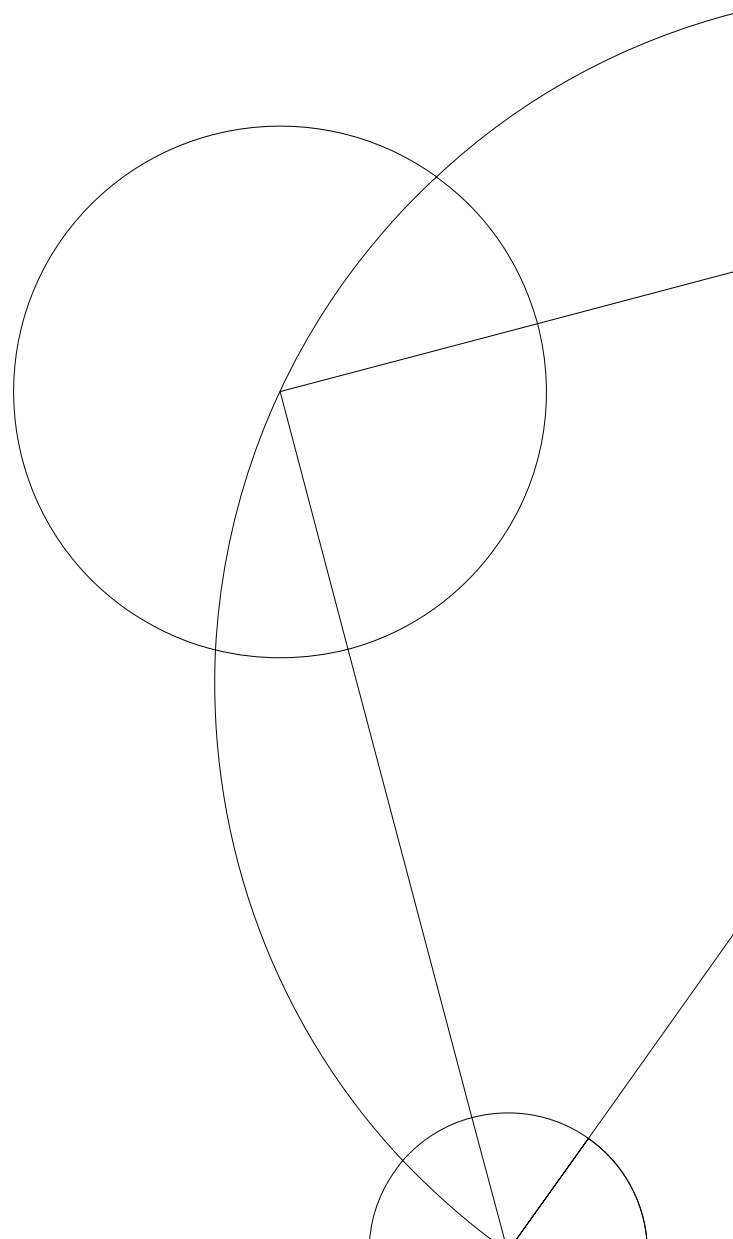
Supervisors:

Dr. Vasileios Gkinis
Dr. Michael Döring
Dr. Guido Vettoretti

External censor:

Dr. Sebastian Bjerregaard Simonsen

15th August, 2022

Abstract

Stable oxygen isotopes from water molecules in polar ice ($\delta^{18}O_{ice}$) and stable nitrogen isotopes enclosed in gas bubbles of ancient ice ($\delta^{15}N$) are quantifiable indicators for paleotemperatures. Paleotemperatures can be reconstructed by forcing firn densification models coupled to heat diffusion and firn air diffusion models with past surface temperature and snow accumulation rate histories and fitting the output $\delta^{15}N$ to measured $\delta^{15}N$ data. The firn community uses a variety of firn models suitable for various ice core sites. However, different firn models predict different surface temperatures. In order to estimate the uncertainty in reconstructed temperatures resulting from using different firn models, various firn models provided by the Community Firn Model (CFM) - an open-source framework providing several modules for the simulation of firn physics processes - are inverted. An automated inversion procedure was implemented with commonly used SciPy minimizers in order to avoid manual parameter search for minimization. Paleotemperatures were reconstructed from $\delta^{18}O_{ice}$ and $\delta^{15}N$ at NorthGRIP, Greenland for different combinations of firn densification and gas diffusion models. Furthermore, run times of the CFM were reduced and a second spin run was implemented within the CFM to make the inversion procedure more feasible. In addition, this thesis provides an overview of the architecture of the CFM and the main modules used for this project.

Acknowledgements

First of all I would like to thank my supervisors Vasileios Gkinis, Michael Döring and Guido Vettoretti for their guidance and their many valuable ideas and inputs throughout this project. I truly appreciated our long and lively discussions even though we did not always share the same opinion. Thanks Vasileios for introducing me to exciting firn physics and your confidence in my programming skills which made me finally be confident about them, too! Thank you Michael for your truthfully never ending patience and excitement to talk about firn air diffusion in the late afternoon hours. Thank you Guido for your inspirations to analyze my code and ideas to make it work faster. Furthermore, I would like to thank the three of you for your support throughout my search for next steps to come, I really appreciated your help and encouragement.

Many thanks also to all the people working and studying at PICE for the friendly and warm environment, for your inspiring pure excitement for your work, Friday lunches and Feierabend-bier.

I would also like to thank my friends Ying, Emily, Dana and Julia for all the funny times we spent together in Copenhagen with winter bathing, climbing and cooking evenings and much more. Thank you for your emotional support and open ear throughout the longest bike rides ever with rough wind and annoying mirrors, thesis crisis and throughout tough times.

Lastly, I would like to thank my family and friends back home for all your support and love. Especially to you, Mom and Dad, who made this all possible, your never ending love, support and confidence in me and for giving me the opportunity to find my own way. Thank you Dominik for being so patient with me and all my crazy ideas, and for all the encouragement, love and support from far away and close.

Contents

List of Figures

List of Tables

List of Abbreviations

CFM	Community Firn Model
BAR	Firn densification model according to Barnola et al. (1991)
GOU	Firn densification model according to Goujon et al. (2003)
HLD	Firn densification model according to Herron and Langway (1980)
HLS	Firn densification model according to Herron and Langway (1980) with Sigfus Johnsen formulation
Christo	Activated firn air diffusion module with firn air advection formulation according to Buizert et al. (2012)
Darcy	Activated firn air diffusion module with firn air advection formulation according to Darcy
zero	Activated firn air diffusion module without firn air advection
FA-off	Disabled firn air diffusion module
DO event	Dansgaard-Oeschger event
NM	Nelder-Mead
LS	Least squares

Chapter 1

Introduction

Changes of the Earth's climate span over timescales from several hundred million years to several thousand to hundred years [2]. Thereby, the causes of climate changes are very diverse and range from plate tectonics [2], the Earth's orbit around the Sun [3], [4], or solar cycles [5] to volcanic eruptions [6], asteroid impacts [7] and lastly the evolution of mankind [8].

The reconstruction of past climatic conditions was conducted in various studies by investigating various so-called climate proxies, indicators of climate change found in climate archives such as sediments, trees, corals or ice [8]. Paleo records are very important to understand past climate but to also be able to make predictions for the present and future climate changes - not only on a natural scientific basis but also to estimate the vulnerability and ability of adaption of human societies and the environment to climate changes.

One of the most fundamental climate variables is temperature which is a driving force of the general circulation of the atmosphere. Thus, in order to better understand past climates and mechanisms of climate change it is important to yield an accurate temperature history.

Past surface temperatures in polar regions are often inferred from stable isotope ratios of oxygen and hydrogen in water molecules of polar ice [9], [10], [11]. The fractionation of oxygen and hydrogen isotopes thereby strongly depends on the temperature of formation of precipitation but also on the site temperature of evaporation or the path way the air masses take until the water condensates and precipitates. Many studies assume a linear or quadratic correlation between stable oxygen isotopes from water molecules in polar ice ($\delta^{18}O_{ice}$) and temperature [12], [10]. However, due to other processes contributing to the isotope fractionation such as the atmospheric pathway or site temperature of evaporation, this relation varies over time and $\delta^{18}O_{ice}$ needs to be calibrated by an independent temperature measurement, e.g. borehole temperatures [10], [11]. Borehole temperature measurements provide a long-term record of surface temperature changes but do not resolve high-frequency temperature changes.

These temperature reconstruction methods can be complemented by measurements of stable isotopes of inert gases such as nitrogen ($\delta^{15}N$) and argon ($\delta^{40}Ar$) enclosed in air bubbles in ancient ice. The isotopic ratios of atmospheric argon and nitrogen remained approximately constant over orbital timescales [13], [14] and their isotopic ratios are assumed to mainly being altered by diffusion processes happening in firn [15] such as gravitational fractionation [16], [14], diffusive smoothing [17] and thermal fractionation caused by changes in temperature [18], [19], [20]. By forcing a firn densification model coupled to heat and

gas diffusion with surface temperature and snow accumulation rate histories, modeled δ^{15}N or δ^{40}Ar can be fitted to measured stable isotope data to reconstruct paleotemperatures [21], [15], [22], [23], [1], [24]. Thereby, many studies assume a linear correlation between δ^{18}O$_{ice}$ and temperatures in a small time interval of several thousand years and find the corresponding optimum slope α and intercept β resulting in the best fit of modeled to measured δ^{15}N or δ^{40}Ar. The parameters α and β are often found by a manual search which makes the whole procedure very time consuming. Furthermore, the firn community uses a variety of firn models suitable for various ice core sites but the choice of firn model introduces an additional uncertainty on the reconstructed paleotemperatures.

The aim of this thesis is to address these issues by assessing the sensitivity of reconstructed temperatures to the choice of different firn models implemented in the Community Firn Model (CFM) and by automating the firn model inversion procedure.

The CFM is an open-source framework providing several modules for the simulation of various physical processes in firn, including among others a set of different firn densification and gas diffusion models that can be coupled to heat diffusion [25]. Greenlandic paleotemperatures are reconstructed by forcing the CFM with temperature histories linearly correlated to stable oxygen isotopes from NorthGRIP and a snow accumulation rate history provided by [1] during a time span lasting from 120,000 years to 10,000 years b2k. A combination out of a set of four firn densification models and four gas diffusion models is used to model δ^{15}N in firn. An automated firn model inversion technique is developed exploiting two commonly used open-source minimizers provided by SciPy to find optimum values of the slope and intercept relating temperature and stable oxygen isotopes in order to fit modeled to measured δ^{15}N. It is furthermore investigated how well the selected minimizers perform to find an optimum temperature curve.

A short overview of the structure and contents of this thesis is given in the following:

In Chapter 2, firn processes such as firn densification, gas diffusion and fractionation processes altering abundances of stable oxygen isotopes form water molecules in ice and stable nitrogen isotopes in gas bubbles are explained. Furthermore, the used firn densification models and gas diffusion models provided by the CFM are described in more detail. Next to firn processes and used firn models, a short overview of used the minimization methods is given.

Chapter 3 presents the used data sets and data pre-processing techniques. It is furthermore explained how the CFM works and which settings are specified for the model runs, how model outputs are obtained and which attempts were made to speed up the model after the identification of bottlenecks. Besides that, it is described how the setup of a second so-called Spin-up run improves run times and avoids data loss. Section 3.3 in Chapter 3 describes the optimization procedure and Section 3.4 the conducted experiments to investigate temperature sensitivities with respect to the choice of firn models.

Chapter 4 presents the results and discussion of the experiments described in Section 3.4.

A concluding summary and outlook is given in Chapter 5.

Chapter 2

Theoretical Background

Climate archives such as sediments, trees, corals or ice give us important information about past climate variability through various so-called climate proxies. Climate proxies are "quantifiable indicators of climate change contained in a climate archive" [2], e.g. tree rings or diatoms, foraminifera and pollen found in sediment cores, or varying abundances of isotopes in sediment or ice cores. In this thesis, the focus lies on abundances of stable oxygen isotopes of water samples from ice cores and stable isotopes of molecular nitrogen from ancient atmosphere trapped in polar ice where these climate signals can date back several hundred thousands of years [2]. Varying abundances of stable isotopes are caused by different fractionation processes in the polar ice which will be explained in this chapter.

2.1 δ - Notation

Isotopes are defined as atoms with the same number of protons but different number of neutrons. Changes in abundances of stable isotopes present in polar ice or gas bubbles enclosed in polar ice occur due to various fractionation processes caused e.g. by temperature and precipitation changes and are thus important indicators of past climate variability.

In the following, isotopes will be denoted as:

$$^{Z+N}X,\tag{2.1}$$

with Z the number of protons and N the number of neutrons. X denotes the element. Stable isotope ratios are generally indicated by the so-called δ-notation:

$$\delta^{Z+N}X = \frac{R_{\text{sample}} - R_{\text{reference}}}{R_{\text{reference}}},\tag{2.2}$$

where R_{sample} denotes the ratio of heavy isotopes of X to light isotopes ($R_{\text{sample}} = {}^{15}\text{N}_{\text{sample}}/{}^{14}\text{N}_{\text{sample}}$) in the specimen, and $R_{\text{reference}}$ denotes the very same ratio for a standard reference.

In this project, the focus lies on the change of stable isotope ratios of oxygen in water molecules of polar ice ($\delta^{18}\text{O}$), and atmospheric nitrogen in gas bubbles enclosed within the ice matrix

(δ^{15}N). The underlying fractionation processes for oxygen and nitrogen stable isotopes will be explained in Sections 2.3 and 2.2.2.1.

2.2 Firn Physics

Firn is denoted as the upper 40 - 120 m of the ice sheet accumulation zones and can be understood as intermediate stage between snow and ice [26], [27]. It is unconsolidated snow that gradually densifies under the weight of overlying precipitation until it approaches pure ice density $\rho_{ice} \approx 920\,kg/m^3$. Pores within the firn are connected and exchange air with the overlying atmosphere, which keeps the firn air younger than the surrounding ice. The difference between the age of the ice and the age of the gas at the so-called lock-in depth (lid, depth where first sealing layers of ice hamper the vertical motion of gas molecules) is the Δage:

$$\Delta age = ice\ age_{lid} - gas\ age_{lid} \tag{2.3}$$

At the bottom of the firn the pores are closed and cannot exchange air with overlying layers anymore. The volume fraction not occupied by ice is defined as the porosity $s = 1 - \rho/\rho_{ice}$. The total porosity consists of the open porosity s_{op} and closed porosity s_{cl}. The open porosity refers to pores that are still connected to the atmosphere and it decreases with depths as gas bubbles gradually close-off. The closed porosity refers to the closed-off air bubbles and thus increases with the depth of the firn column [26].

Firn can be divided into three zones which are related to the modes of firn air transport. The **convective zone** (CZ) refers to the upper part of the firn. Its depth depends among others on the local accumulation rate, local temperature and wind strength. Particularly deep convective zones are found at sites with very low accumulation rates and strong wind [29]. Firn air in the CZ has approximately atmospheric composition due to the continuous ventilation, so δ^{15}N $= 0$. The zone below the CZ is the **diffusive zone** (DZ). The mass transfer in the DZ is dominated by molecular diffusion. In diffusive equilibrium heavy isotopes and heavy molecules are enriched with increasing depth due to gravitational fractionation [30]. Furthermore, the diffusivity decreases with depth due to the gradual pore compaction (decreasing open porosity). At the lock-in depth the air gets isolated from the atmosphere, which defines the Δage between the trapped air and the surrounding ice. The lower zone of the firn is the **non-diffusive zone** or **lock-in zone**. It is characterized by sealing ice layers which hamper the vertical motion of firn air and thus further fractionation of gas isotopes. The downward transport is dominated by advection (motion with the ice matrix). The close-off depth z_{cod} is defined as the depth where all bubbles are occluded and thus $s_{op} = 0$. The corresponding close-off density ρ_{cod} depends on temperature but is also influenced by insolation and wind strength [26]. The mean close-off density $\bar{\rho}_{cod}$ is found within the interval 795 - 830 kg/m^3. Martinerie et al. (1992, 1994) described the mean close-off density as a function of the site temperature T [27], [31]:

$$\bar{\rho}_{cod} = \left(\frac{1}{\rho_{ice}} + 6.95 \cdot 10^{-7}T - 4.3 \cdot 10^{-5} \right)^{-1}. \tag{2.4}$$
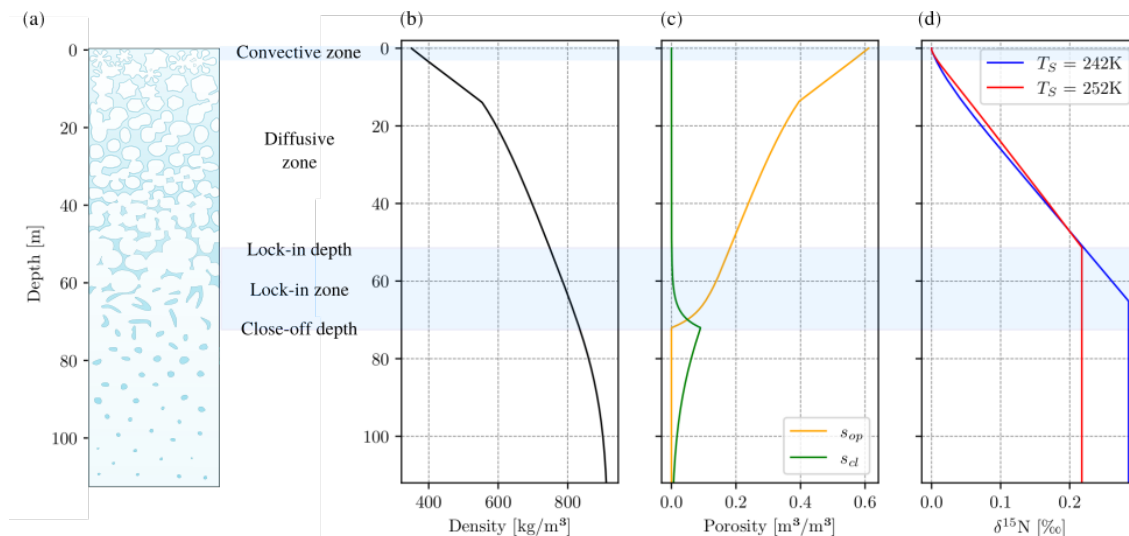
Figure 2.1: *Firn characteristics.* *(a) Sketch of a firn column with transformation of snow to ice. Adapted from [28]. (b) Firn densification modeled using the Barnola model implemented in the CFM for a temperature forcing of $242\,\mathrm{K}$. (c) Open and closed porosity modeled with the CFM. (d) $\delta^{15}N$ distributions with depth for two different temperature forcings T_S modeled using the CFM's firn air diffusion module. The deviation from a linear distribution within the firn due to gravitational fractionation stems from thermal fractionation. Furthermore, higher temperatures lead to a more shallow firn column which is also visible in (d) Adapted and modified from [28], [24]*

However, air exchange stops already at lower densities than the close-off density due to the sealing ice layers. The lock-in density ρ_{lid}, which marks the beginning of the non-diffusive zone and thus the location/density where enrichment of nitrogen isotopes stops, was empirically defined as [28]:

$$\rho_{\mathrm{lid}} = \bar{\rho}_{\mathrm{cod}} - 14\,\mathrm{kg/m^3}. \qquad (2.5)$$

The relevant processes occurring in the firn that influence the stable nitrogen isotope distributions are introduced in more detail in the following.

2.2.1 Firn Densification Models

Firn densification models describe the firn densification in mainly three stages. The first stage ranges from snow to firn of the "critical density" $\rho_{\mathrm{crit}} = 550\,\mathrm{kg/m^3}$. In this stage, firn densification is dominated by grain settling and packing and the densification rate is the most rapid of the three stages. The second densification stage ranges from densities between the critical density ($550\,\mathrm{kg/m^3}$) and $820 - 840\,\mathrm{kg/m^3}$, where individual bubbles are formed. The densification in this stage takes place more slowly. In the third densification stage, ranging from $820 - 840\,\mathrm{kg/m^3}$ to $950\,\mathrm{kg/m^3}$, gas bubbles are further compressed. With increasing depth the volumes of the gas bubbles are further compressed and single air molecules are settled within the ice matrix due to the increasing pressure. [32]

Several firn densification models describing the densification in the first two stages, which are the most crucial ones, have been developed. In this thesis, the densification models by Herron and Langway [32], Sigfus, Goujon [33] and Barnola [34] are used/investigated. The four models are shortly introduced in the following.

2.2.1.1 The Herron and Langway Model

The Herron and Langway model is an empirical model based on the assumption that a "change in air space is linearly related to the change in stress due to the weight of overlying snow" [32]:

$$\frac{\mathrm{d}\rho}{\rho_\mathrm{ice} - \rho} = C \cdot \rho \, \mathrm{d}h, \tag{2.6}$$

with $\rho_\mathrm{ice} = 917 \, \mathrm{kg/m^3}$ and C is a constant. Herron and Langway derived equations for the densification rate for the first two stages of densification. The first densification stage ranges from the surface (snow density) to the critical density of $550 \, \mathrm{kg/m^3}$ and is characterized by rapid densification rates. The second densification stage ranges from the critical density to the close-off density $(820 - 840 \, \mathrm{kg/m^3})$. Equation (2.6) implies that $\ln\left(\rho/_{\rho_\mathrm{ice}-\rho}\right)$ and depth are linearly related, which is also observed in plots of $\ln\left(\rho/_{\rho_\mathrm{ice}-\rho}\right)$ versus depth from depth-density information available from various sites:

$$h \propto \ln\left(\rho/(\rho_\mathrm{ice} - \rho)\right). \tag{2.7}$$

The slopes of these segments can be expressed as:

$$C^* = \frac{\mathrm{d}\ln\left(\rho/(\rho_\mathrm{ice} - \rho)\right)}{\mathrm{d}h} \qquad \text{for} \qquad \rho < 550 \, \frac{\mathrm{kg}}{\mathrm{m^3}}, \tag{2.8}$$

$$C^{**} = \frac{\mathrm{d}\ln(\rho/(\rho_\mathrm{ice} - \rho))}{\mathrm{d}h} \qquad \text{for} \quad 550 \, \frac{\mathrm{kg}}{\mathrm{m^3}} < \rho < 800 \, \frac{\mathrm{kg}}{\mathrm{m^3}}. \tag{2.9}$$

One can solve for the densification rate $\frac{\mathrm{d}\rho}{\mathrm{d}t}$ by introducing the substitution $\mathrm{d}h/\mathrm{d}t = A/\rho$ where A denotes the accumulation rate in water equivalents:

$$\frac{\mathrm{d}\rho}{\mathrm{d}t} = \begin{cases} \dfrac{C^* A}{\rho_\mathrm{ice}}(\rho_\mathrm{ice} - \rho) & \text{for} & \rho < 550 \, \dfrac{\mathrm{kg}}{\mathrm{m^3}}, \\[2ex] \dfrac{C^{**} A}{\rho_\mathrm{ice}}(\rho_\mathrm{ice} - \rho) & \text{for} \quad 550 \, \dfrac{\mathrm{kg}}{\mathrm{m^3}} < \rho < 800 \, \dfrac{\mathrm{kg}}{\mathrm{m^3}}. \end{cases} \tag{2.10}$$

For the following derivations, Herron and Langway assumed that temperature and accumulation rates are not correlated and that Equations (2.10) can be rewritten as Arrhenius type equations:

$$\frac{\mathrm{d}\rho}{\mathrm{d}t} = \begin{cases} k_0 A^a(\rho_\mathrm{ice} - \rho) & \text{for} & \rho < 550 \, \dfrac{\mathrm{kg}}{\mathrm{m^3}}, \\[2ex] k_1 A^b(\rho_\mathrm{ice} - \rho) & \text{for} \quad 550 \, \dfrac{\mathrm{kg}}{\mathrm{m^3}} < \rho < 800 \, \dfrac{\mathrm{kg}}{\mathrm{m^3}}, \end{cases} \tag{2.11}$$

with k_0 and k_1 temperature dependent Arrhenius-type rate constants, and a and b are constants related to densification mechanisms. a and b can be determined by comparing the slopes for the two densification stages ($C^* = k_0 A^a$ and $C^{**} = k_1 A^b$) of two different sites (1 and 2) with similar temperatures but different accumulation rates such that:

$$a = \frac{\ln(C_1^*/C_2^*)}{\ln(A_1/A_2)} + 1 \quad \text{and} \quad b = \frac{\ln(C_1^{**}/C_2^{**})}{\ln(A_1/A_2)} + 1. \tag{2.12}$$

Using this approach for various sites, the values for the constants a and b were determined to $a \approx 1$ and $b \approx 0.5$. The Arrhenius type rate constants k_0 and k_1 were determined from Arrhenius plots of $\ln k$ against $1/T$ resulting in:

$$k_0 = 11 \exp\left(-\frac{10160}{RT}\right) \quad \text{and} \quad k_1 = 575 \exp\left(-\frac{21400}{RT}\right). \tag{2.13}$$

From the densification rate it is then possible to derive equations for depth-density and depth-age relations. Using again the relation $\mathrm{d}h/\mathrm{d}t = \frac{A}{\rho}$ and integrating $\mathrm{d}\rho$ over depth h with the boundary conditions $h_0 = 0$ and $\rho = \rho_0$ at the surface one obtains for the first stage of densification:

$$\rho_{\mathrm{h}} = \frac{\rho_{\mathrm{ice}} Z_0}{1 + Z_0}, \tag{2.14}$$

with $Z_0 = \exp\left(\rho_{\mathrm{ice}} k_0 h + \ln\left(\frac{\rho_0}{\rho_{\mathrm{ice}} - \rho_0}\right)\right)$.

The critical density depth $h_{0.55}$ and critical density age $t_{0.55}$ can then be expressed as:

$$h_{0.55} = \frac{1}{\rho_{\mathrm{ice}} k_0} \left(\ln\left(\frac{0.55\,\mathrm{Mg/m}^3}{\rho_{\mathrm{ice}} - 0.55\,\mathrm{Mg/m}^3} \right) - \ln\left(\frac{\rho_0}{\rho_{\mathrm{ice}} - \rho_0} \right) \right), \tag{2.15}$$

$$t_{0.55} = \frac{1}{k_0 A} \ln\left(\frac{\rho_{\mathrm{ice}} - \rho_0}{\rho_{\mathrm{ice}} - 0.55\,\mathrm{Mg/m}^3} \right). \tag{2.16}$$

Densities and ages in the second densification stage are determined accordingly:

$$\rho_{\mathrm{h}} = \frac{\rho_{\mathrm{ice}} Z_1}{1 + Z_1}, \tag{2.17}$$

$$t_\rho = \frac{1}{k_1 A^{0.5}} \ln\left(\frac{\rho_{\mathrm{ice}} - 0.55\,\mathrm{Mg/m}^3}{\rho_{\mathrm{ice}} - \rho} \right) + t_{0.55}, \tag{2.18}$$

with $Z_1 = \exp\left(\frac{\rho_{\mathrm{ice}} k_1 (h - h_{0.55})}{A^{0.5}} + \ln\left(\frac{0.55\,\mathrm{Mg/m}^3}{\rho_{\mathrm{ice}} - 0.55\,\mathrm{Mg/m}^3}\right)\right)$, and A the mean accumulation rate $A = \left(\frac{\rho_{\mathrm{ice}} k_1}{C^{**}}\right)^2$ [32].

2.2.1.2 The Sigfus Model

The Sigfus model uses basicallly the Herron and Langway formulation. The densification in the first densification zone is calculated identically. The second densification zone includes

stress σ and the Arrhenius type rate constant for the second zone is slightly altered to:

$$k_{\text{Sig}} = \left[k_1 \cdot \exp\left(-\frac{21400}{RT} \right) \right]^2, \tag{2.19}$$

where k_1 is the Arrhenius type rate constant calculated in Herron and Langway according to Equation (2.13).

The densification rate in the second zone is then calculated according to:

$$\frac{\mathrm{d}\rho}{\mathrm{d}t} = k_{\text{Sig}} \cdot \frac{(\sigma - \sigma_{550}) \cdot (\rho_{\text{ice}} - \rho)}{g \cdot \ln\left(\frac{\rho_{\text{ice}} - 0.55\,\text{Mg/m}^3}{\rho_{\text{ice}} - \rho} \right)}, \tag{2.20}$$

with σ_{550} the stress at the transition between first and second densification zone.

2.2.1.3 The Barnola Model

The Barnola model uses the Herron and Langway model for the first densification zone and applies the Pimienta model for the second and third densification zone [25], [34].
The Pimienta model describes densification of ice below the close-off as plastic deformation of ice around air bubbles and air channels. The densification rate is described as:

$$\frac{\mathrm{d}\rho}{\mathrm{d}t} = Af\Delta P^n = \rho_{\text{ice}} A_0 \exp\left(-\frac{Q}{RT} \right) f \Delta P^n, \tag{2.21}$$

where A_0 is a constant, Q is the activation energy for mechanical creep and ΔP is the effective pressure [34]. The exponent n is in the range between 1 and 3 and is stress dependent. Pimienta and Duval (1987) conducted stress tests on polar ice in order to determine the dependence of the strain rate $\mathrm{d}\varepsilon/\mathrm{d}t$ on the stress σ ($\mathrm{d}\varepsilon/\mathrm{d}t = A\sigma^n$) and found n to be 1 for stresses of $0.1\,\text{MPa}$ and lower, and 3 for stresses higher than $0.1\,\text{MPa}$ [35]. The function f is described by the spherical pore model of Wilkinson and Ashby (1975) who investigated the densification process of a powder compact during pressure sintering [36]:

$$f_{\text{s}}(\rho) = \frac{3}{16} \left(1 - \rho/\rho_{\text{ice}} \right) / \left(1 - (1 - \rho/\rho_{\text{ice}})^{1/3} \right)^3. \tag{2.22}$$

Barnola et al. deduced a function f for firn in the second densification zone (for the Barnola model: $550 - 800\,\text{kg/m}^3$) by analyzing Antarctic and Greenland density profiles with different temperature and accumulation histories using Equation (2.21):

$$f_{\text{e}}(\rho) = 10^{\alpha\rho^3 + \beta\rho^2 + \delta\rho + \gamma}, \tag{2.23}$$

where $\alpha = -37.455$, $\beta = 99.743$, $\gamma = 30.673$ and $\delta = -95.027$.

For the third densification zone ($\rho > 800\,\text{kg/m}^3$) the Barnola model uses the Pimienta model with $f = f_{\text{s}}(\rho)$. Thereby, $f_{\text{e}}(\rho)$ is constructed such that $f_{\text{e}}(\rho)$ and $f_{\text{s}}(\rho)$, as well as their derivatives are equal at the transition from the second to the third densification zone ($\rho =$

$800\,\text{kg/m}^3$). For both densification zones, n was chosen to be 3 since stress in firn "rapidly" becomes higher than $0.1\,\text{MPa}$.

The Pimienta model was included into the Barnola model since the Herron and Langway model in general reacts slower or does not react to shortly lasting climatic transitions and is less suitable to sites with a relatively high accumulation rate compared to the surface temperature. In the studies of Barnola et al. (1991) the Pimienta model provided more realistic results for a wider range of climatic conditions [34].

2.2.1.4 The Goujon Model

Goujon et al. (2003) coupled grain boundary sliding and grain deformation with heat diffusion. The Goujon model assumes that densification in the first zone ($D < 0.6$) is predominated by boundary sliding of grains, where $D = \frac{\rho}{\rho_{\text{ice}}}$ is the relative density. The densification rate in the first zone is described as:

$$\frac{\mathrm{d}D}{\mathrm{d}t} = \gamma \left(\frac{P}{D^2}\right)\left(1 - \frac{5}{3}D\right), \tag{2.24}$$

based on a grain-boundary sliding model by Alley (1987) where grain sliding depends on the number of neighbors. For a coordination number $Z < 6$, grains are able to slide whereas for $Z \approx 6$ a grain is supported by a tripod of bonds and the grain cannot slide anymore which means that the critical density $D_0 \approx 0.6$ is reached [37]. In Equation (2.24), P denotes the pressure due to the overlying snow/firn and γ is a scaling factor depending on the viscosity of grain boundaries and the geometry of grains. [37], [25].

In the second densification zone ($0.6 \leq D < 0.9$), boundary sliding becomes negligible and densification happens primarily via plastic and elastic deformation of grains due to pressure acting on the grain contact areas [33], [25]. With increasing contact areas the densification happens through a power-law creep mechanism described in Arzt (1982) who investigated densification processes on dense packed spherical powders. According to the cold compaction theory in Arzt (1982), Goujon et al. (2003) describe the densification rate in the second zone as:

$$\frac{\mathrm{d}D}{\mathrm{d}t} = 4.1817 \cdot 10^4 \exp\left(-\frac{E_A}{RT}\right)\left(D^2 D_0\right)^{1/3}\left(\frac{a}{\pi}\right)^{1/2}\left(\frac{4\pi P}{3aZD}\right)^3, \tag{2.25}$$

where E_A denotes the Arrhenius activation energy ($60\,\text{kJ/mol}$), P the pressure due to the ice column applied on an average contact area a between grains, R the gas constant and Z the coordination number [33], [38], [25]. The critical density D_0 is the relative density at the transition between the first and the second densification zone and it depends on the mean annual temperature T_{m} of the ice core sites [39]:

$$D_0 = 0.00226 \cdot T_{\text{m}}[K] + 0.03. \tag{2.26}$$

The densification process in the second zone proceeds until $D = D_{\text{cod}}$, the relative density at

the close-off. The close-off density is thereby calculated according to the relation derived by Martinerie et al. (1994) (see Equation (2.4)) [33].

The viscosity scaling factor γ in Equation (2.24) should be set such that the densification rate is constant at D_0.

Barnola et al. (2015) reported some issue in implementing the Goujon model as suggested in Goujon et al. (2003): For critical densities $D_0 > 0.6$ the densification rate $\frac{\mathrm{d}D}{\mathrm{d}t}$ according to Equation (2.24) becomes zero for $D = 0.6$ and negative for $D < 0.6$ which is physically not meaningful. Furthermore, at $D = D_0$ the densification rate according to Equation (2.25) becomes infinite because the contact area is equal to zero. In order to overcome these issues, Stevens et al. (2020) slightly altered the implementation of the Goujon model at the transition between the first and second densification zone in the CFM: D_0 is limited to a maximum value of 0.59 corresponding to $\rho = 541\,\mathrm{kg/m^3}$. This means that the transition between the two zones is in general predicted to occur at lower densities than the common value of $\rho = 550\,\mathrm{kg/m^3}$. The transition between the two zones is set to $D_0' = D_0 + \epsilon$, where ϵ is a small value. γ is then iterated to give a maximum value for $\frac{\mathrm{d}D}{\mathrm{d}t}$ at the bottom of the first zone and to not exceed $\frac{\mathrm{d}D}{\mathrm{d}t}$ at the top of the second zone [25].

The third densification zone ($0.9 \leq D < 1$) describes the densification of bubbly ice with the deformation of an ice matrix with cylindrical ($D < 0.95$) and spherical ($D \geq 0.95$) gas bubbles. The respective densification rates are [33]:

$$\frac{\mathrm{d}D}{\mathrm{d}t} = \begin{cases} 2A \left(\dfrac{D(1-D)}{[1-(1-D)^{1/3}]^3} \right) \cdot \left(\dfrac{2P_{\mathrm{eff}}}{3} \right)^3 & \text{for} \quad 0.9 < D < 0.95, \\ \dfrac{9}{4} \cdot A(1-D)P_{\mathrm{eff}} & \text{for} \qquad D \geq 0.95, \end{cases} \tag{2.27}$$

with

$$P_{\mathrm{eff}} = P + P_{\mathrm{atm}} - P_{\mathrm{b}}, \tag{2.28}$$

where P_{atm} is the atmospheric pressure at the altitude at the site, and P_{b} is the pressure of the bubbles in the ice, and

$$A = 7.89 \cdot 10^3 \exp\left(\frac{-E_{\mathrm{A}}}{RT} \right) [\mathrm{MPa^{-3}s^{-1}}]. \tag{2.29}$$

2.2.2 Gas Diffusion

The composition of the downward travelling air in the firn column is altered by several mechanisms such as gravitational separation [16], [14], diffusive smoothing [17] and thermal fractionation [18], [19], [20] caused by changes in temperature.
Next to these fractionation processes, stable gas isotope ratios in firn can be additionally altered by wind speed and surface pressure changes, but these mechanisms are assumed to be less relevant for the data used in this study [20]. Isotope signals of ancient air extracted
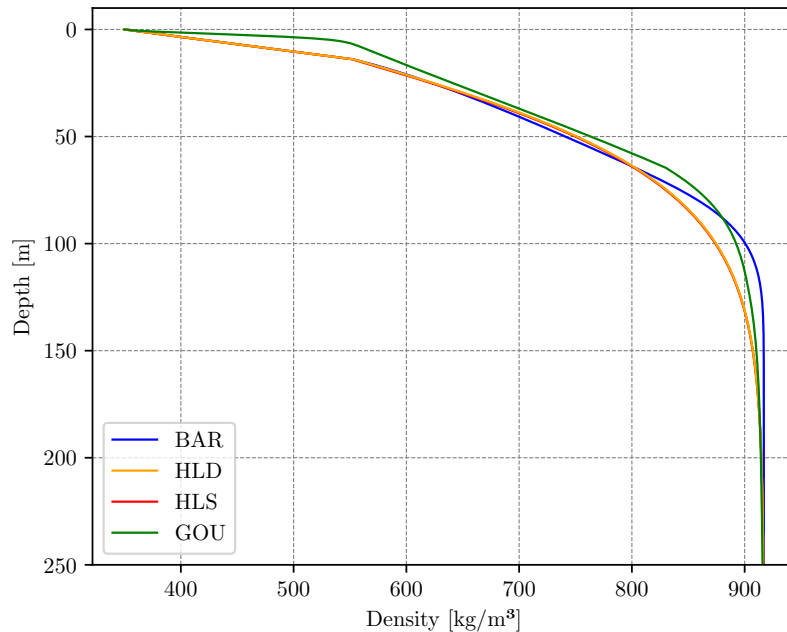
Figure 2.2: *modeled firn density versus depth for four different firn densification models. Model of the densification in the three densification zones using Barnola (BAR), Herron and Langway (HLD), Sigfus (HLS) and Goujon (GOU) with a constant forcing (T = 242 K and A = 0.19 m ice /yr).*

from the bubbles within the ice serve thus to draw conclusions about past climate if temperature changes are large and rapid enough. A common way to infer fast surface temperature changes are stable nitrogen isotope abundances in gas bubbles enclosed in the ice matrix. This is because the isotopic compositions of nitrogen are constant in the atmosphere at orbital timescales [13], [14] which means that $\delta^{15}N = 0$. Consequently, changes in the isotopic ratio are assumed to mainly reflect diffusion processes that are mostly dependent on site, firn temperature and snow accumulation [15]. $\delta^{15}N$ measurements thus complement borehole temperature reconstructions which are not suitable to detect temperature shifts on short timescales [40], [21].

In this thesis, $\delta^{15}N$ values are modeled using the CFM in order to determine surface temperature histories during the Last Glacial Period following two approaches. The first approach calculates the $\delta^{15}N$ values for gravitational enrichment and thermal diffusion according to [16], [30] and [41], [15]. The second approach exploits the `firn_air` module of the CFM which solves the firn-air transport equation. The `firn_air` module accounts for molecular diffusion, thermal and gravitational fractionation and firn air advection.

2.2.2.1 Gravitational and Thermal Fractionation

Gravitational fractionation means that heavier isotopes and heavier molecules enrich with increasing depth in the firn column. Assuming diffusive equilibrium, the enrichment due to gravitational fractionation is expressed as:

$$\delta_{\text{grav}}^X [‰] = \left[\exp\left(\frac{gz\Delta M_X}{RT} \right) - 1 \right] \cdot 10^3 \approx \frac{gz\Delta M_X}{RT} \cdot 10^3, \tag{2.30}$$

with ΔM_X the molar mass deviation of species X from air in kg mol^{-1} or the mass difference between two isotopologues [16], [30].

Thermal diffusion due to a temperature gradient in the firn leads to a thermal fractionation and as such to an enrichment of heavy isotopes at the colder end of the firn column. As an example, a rapid warming at the surface of the ice leads to an enrichment of heavy isotopes at the bottom of the firn column, while a cooling would have the opposite effect. The thermal fractionation is expressed as:

$$\delta_{\text{therm}}^X [‰] = \left[\left(\frac{T_{\text{s}}}{T_{\text{b}}} \right)^{\alpha_{\text{T},X}} - 1 \right] \cdot 10^3 \approx \Omega_X \cdot \Delta T, \tag{2.31}$$

with $\Delta T = T_{\text{h}} - T_{\text{c}}$ the temperature gradient between the hot and cold end of the firn column, $\alpha_{\text{T},S}$ the thermal diffusion constant for species X and Ω_X the thermal diffusion sensitivity of species X [41], [15]:

$$\Omega_X \approx \frac{\alpha_{\text{T},X}}{\overline{T}} \cdot 10^3. \tag{2.32}$$

$\overline{T}$ hereby denotes the mean firn temperature which can be calculated as [15]:

$$\overline{T} = \frac{T_{\text{h}} T_{\text{c}}}{T_{\text{h}} - T_{\text{c}}} \cdot \ln\left(\frac{T_{\text{h}}}{T_{\text{c}}} \right). \tag{2.33}$$

The thermal diffusion sensitivity Ω_X and the thermal diffusion constant α_{T} for stable nitrogen isotopes were determined empirically by measuring the thermal fractionation of equilibrated air at a known temperature gradient in a temperature range between $-60\,°C$ and $0\,°C$ by [42]:

$$\alpha_{\text{T,N}} \approx \left(8.656 - \frac{1232}{\overline{T}} \right) \cdot 10^{-3} \tag{2.34}$$

$$\Omega_{\text{N}} \approx \left(\left(\frac{8.656}{\overline{T}} - \frac{1232}{\overline{T}^2} \right) \right) ‰/°C. \tag{2.35}$$

Figure 2.3 shows the excursions of stable nitrogen isotopes due to thermal and gravitational fractionation for a firn column modeled with the CFM. The CFM is forced with surface temperatures and accumulation depicted in Figure 2.3(a). Firn densification is calculated according to Barnola. Figure 2.3(b) shows the change in lock-in depth with modeltime due to the change in surface temperature. Higher surface temperatures lead to a more shallow firn column, and thus, to smaller lock-in depths due to faster densification with higher temperat-
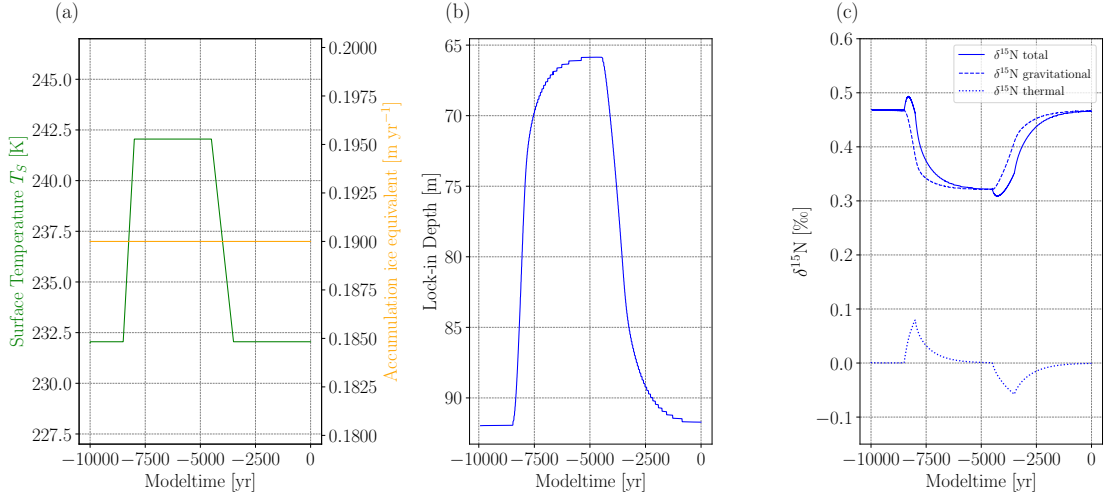
Figure 2.3: *Thermal and gravitational fractionation of stable nitrogen isotopes.* $\delta^{15}N$ *excursions calculated according to Equation (2.30) and (2.31) from firn column modeled with CFM using Barnola's densification model. (a) Temperature and accumulation forcing. (b) Change of lock-in depth with modeltime due to the change in the temperature forcing. (c) Thermal, gravitational and total fractionation of stable nitrogen isotopes.*

ures within the firn. This is closely related to the Arrhenius activation energy/theorem, which predicts a higher level of crystallization with higher temperatures. Gravitational fractionation is approximately linearly dependent on depth z (compare Equation (2.30)) and as such decreases/increases parallel to decreasing/increasing lock-in depths (Figure 2.3). A change toward warmer surface temperatures leads to a positive $\delta^{15}N_{\text{therm}}$ excursion since the heavier ^{15}N isotopes enrich at the colder end of the firn columns (lock-in depth). For a change toward colder surface temperatures the opposite effect is observed.

2.2.2.2 Firn-Air Transport Equation

The transport of gas is commonly described by the one-dimensional diffusion equation first introduced by [43] including only pure molecular diffusion and gravitational settling. The transport equation was further developed in [44], [20], [45], [29] additionally including thermal diffusion and the advection of air within the ice matrix. The firn-air transport equation solved in the CFM has the following form:

$$\frac{\partial C}{\partial t} = \frac{1}{s_{\text{op}}(t,z)} \frac{\partial}{\partial z} \left[s_{\text{op}}(t,z) \kappa_{\text{eff}}(t,z) \left(\frac{\partial C}{\partial z} - \frac{\Delta M_X g}{RT} + \Omega_X \frac{\mathrm{d}T}{\mathrm{d}z} \right) \right] - w_{\text{air}}(z) \frac{\partial C}{\partial z}, \qquad (2.36)$$

where C is the concentration of a gas species X, κ_{eff} is the effective molecular diffusivity of gas in porous snow and w_{air} is the advection rate of firn air [25]. The latter two terms of the first term on the right hand side are the gravitational settling term and thermal diffusion term describing the fractionation of isotopologues due to gravitational force and thermal diffusion.

13

In the CFM, the thermal diffusion sensitivity Ω_N for stable nitrogen isotopes was chosen to be $\Omega_N = 14.7 \cdot 10^{-3}\,\text{‰}/°C$ according to [42], which is approximately valid for an average firn air temperature of $-30\,°C$.

The effective diffusivity k_{eff} accounts for the fact that firn air needs to take a longer, more tortuous way through the pores as the open porosity decreases. For the experiments presented in this thesis, the following parameterization according to [46] is used:

$$k_{\text{eff}} = \gamma_N \cdot D(s) = \gamma_N \cdot c(23.7s - 2.84), \tag{2.37}$$

with $\gamma_N = 1.2638$ the free-air diffusivity of nitrogen gas relative to CO_2 [47], [44] and $D(s)$ the diffusion coefficient for CO_2 in relation to the total firn porosity s. c is a temperature and pressure correction factor ($c = 1013.25/p[\text{hPa}] \cdot (T[\text{K}])/253.16)^{1.85}$) [46].

The firn-air advection rate w_{air} is represented with two different parameterizations according to [48] and Darcy's law (also mentioned in [49]):

Firn air advection according to Darcy The parameterization of firn air advection according to Darcy is based on viscous flow of firn air through disordered porous medium (firn). The firn air pressure $p(z)$ increases with depth z in hydrostatic equilibrium according to the barometric equation:

$$p(z) = p_0 \exp\left(-\frac{M_{\text{air}}g}{RT}z\right), \tag{2.38}$$

where p_0 is the surface pressure, M is the molar mass of air, g is the gravitational acceleration, R is the gas constant and T is the temperature at depth z.

A deviation from the hydrostatic equilibrium results in a viscous air flow, which is described by Darcy's law:

$$v = -\frac{k}{\mu}\left(\frac{dp}{dz} - \frac{M_{\text{air}}g}{RT}p\right), \tag{2.39}$$

with k the permeability of firn and μ the dynamic viscosity of firn air [49].

Firn air advection according to Buizert Buizert looks into the bulk motion of firn air and describes the fluxes of firn air occurring in open and closed porosity as well as the flux between open and closed porosity during the close up of pores to isolated bubbles. The flux in the closed porosity is dominated by the downward transport of bubbles by the ice matrix with velocity $w_{\text{ice}} = A\rho_{\text{ice}}/\rho$, where A is the accumulation rate in ice equivalent and ρ and ρ_{ice} are the densities of firn and ice, respectively. The flux in the open porosity is determined by the advection rate of air w_{air} in open pores. The fluxes in open and closed porosity are [48]:

$$\Phi_{\text{op}} = s_{\text{op}}^* \cdot w_{\text{air}} = s_{\text{op}} \cdot \exp\left(-\frac{M_{\text{air}}g}{RT}z\right) \cdot w_{\text{air}}, \tag{2.40}$$

$$\Phi_{\text{cl}} = s_{\text{cl}} \cdot \frac{p_{\text{cl}}}{p_0} \cdot w_{\text{ice}}, \tag{2.41}$$
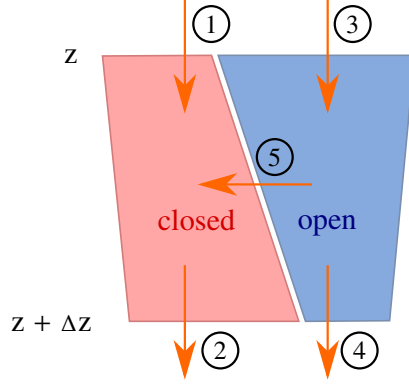
Figure 2.4: *Schematic of air fluxes in firn.* *The total and open porosities decrease and the closed porosity increases. Adapted from [48].*

with s_{op}^* is the effective open porosity accounting for the increasing pressure with depth. p_{cl}/p_0 describes the enhanced pressure in the closed porosity relative to the surface pressure. The fluxes occurring in firn between z and $z + \Delta z$ are depicted in Figure 2.4.

Φ_1 and Φ_2 depict bulk air transport in closed porosity, Φ_3 and Φ_4 bulk air transport in open porosity and Φ_5 describes the trapping of firn air in bubbles. Mass conservation requires that $\Phi_1 + \Phi_3 = \Phi_2 + \Phi_4$ which can be generalized to [48]:

$$\Phi_{op}(z) + \Phi_{cl}(z) = \Phi_{op}(z_{cod}) + \Phi_{cl}(z_{cod}) = \Phi_{cl}(z_{cod}). \tag{2.42}$$

Combining Equations (2.38), (2.39) and (2.42) allows to solve for the firn air velocity in open porosity [48]:

$$w_{air} = \frac{A\rho_{ice}}{s_{op}^*} \left(\frac{s_{cl}(z_{cod})p_{cl}(z_{cod})}{\rho_{cod}} - \frac{s_{cl}(z)p_{cl}(z)}{\rho(z)} \right). \tag{2.43}$$

Figure 2.5(c) shows the modeled nitrogen excursions at lock-in depth with time due to thermal and gravitational fractionation. $\delta^{15}N$ is modeled with the CFM using four different densification models (BAR, HLD, HLS, GOU) and the `firn_air` module which solves for the firn-air diffusion equation. The model is forced with constant accumulation and a double temperature ramp (Figure 2.5 (a)). The different densification models predict different lock-in depths which consequently results in higher $\delta^{15}N$ excursions for deeper lock-in depths due to advanced gravitational fractionation and vice versa (provided the accumulation stays constant in the presented example).
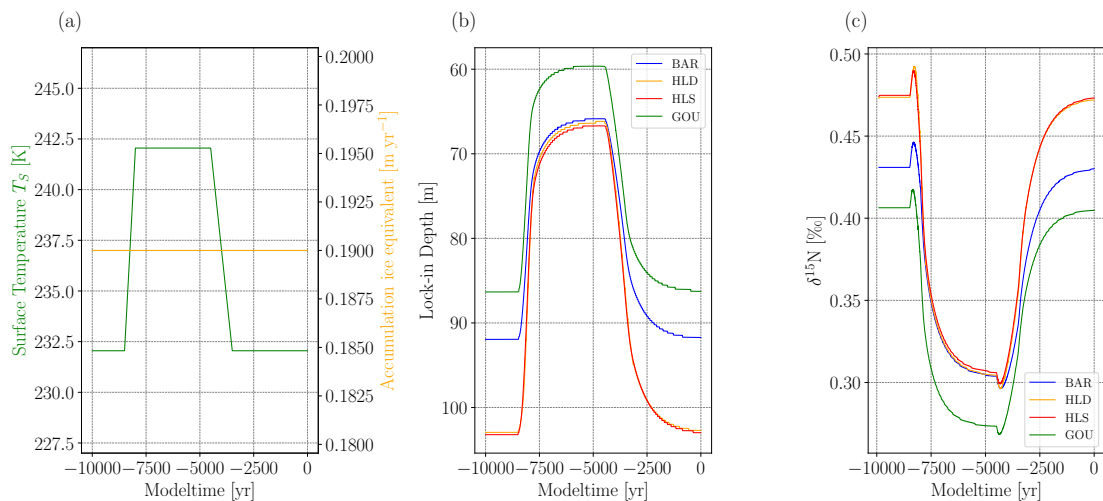
Figure 2.5: *Firn air diffusion.* *Firn air diffusion modeled using four different firn densification models and the* `firn_air` *module of the CFM which solves the firn-air transport equation. (a) Surface temperature and accumulation forcing. (b) Change of lock-in depth with modeltime for the four different densification models Barnola (BAR), Herron and Langway (HLD), Sigfus (HLS) and Goujon (GOU). The lock-in depth decreases with increasing temperature and vice versa. (c) Change of $\delta^{15}N$ at the lock-in depth with modeltime.*

2.3 Oxygen Isotopes and Temperature Reconstruction

Past surface temperatures are commonly inferred from stable water isotopes (δD and $\delta^{18}O_{ice}$) in polar ice [50], [10], [11]. The underlying fractionation processes that lead to varying abundances of stable isotopes with depth are complex and depend on various factors. Hence, $\delta^{18}O_{ice}$ varies with the temperature of the water vapor source, the atmospheric pathway the water molecules take and the condensation temperature: warm air holds more water vapor and thus a higher amount of heavier isotopologues. At the same time, heavy isotopologues are preferentially removed from the air with decreasing temperature e.g. through increasing elevation and latitude or seasonal temperature variability (Rayleigh distillation) which leads to a δ-value more depleted in the heavy isotopes and so more negative. [2], [51].

Previous studies used the correlation between $\delta^{18}O$ from precipitation and temperature of formation of precipitation/surface temperature to reconstruct past surface temperatures assuming a linear (or quadratic) relation [12], [10]:

$$T_S = \alpha \cdot \delta^{18}O_{ice} + \beta, \qquad \text{or} \qquad (2.44)$$

$$(T_S = \alpha^* \cdot \delta^{18}O_{ice}^2 + \beta^* \cdot \delta^{18}O_{ice} + \gamma^*), \qquad (2.45)$$

with α the slope of the linear function β the intercept. However, the present-day spatial slope describing the relation between surface temperature and $\delta^{18}O_{ice}$ is not constant over time [52],

H$_2^{18}$O
H$_2^{16}$O

-10 ‰

-20 ‰

-35 ‰

-45 ‰

-10 ‰

-10 ‰

-25 ‰

-30 ‰

-10 ‰

δ^{18}O $\approx$ 0 ‰ (SMOW)
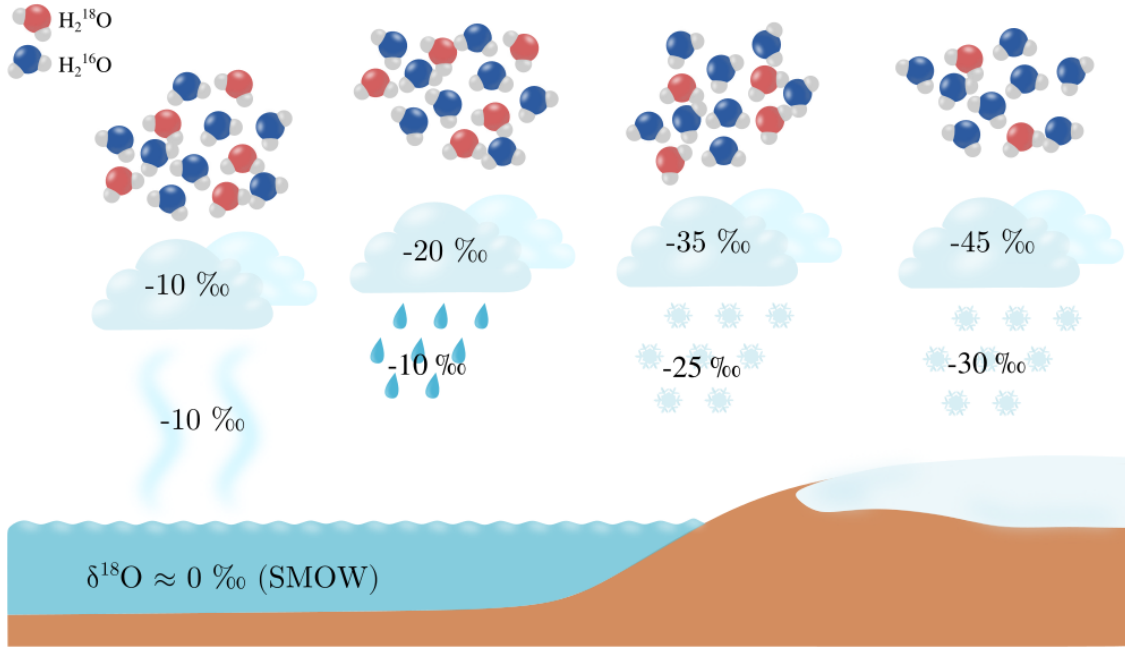
Figure 2.6: *Fractionation of stable water isotopes.* *Schematic of the fractionation of stable water isotopes due to evaporation and condensation. Due to the higher vapor pressure of lighter molecules, lighter water isotopes preferentially evaporate which results in a lower $\delta^{18}O_{vapor}$ value than the ocean (standard 0 ‰ SMOW) and thus to a more negative $\delta^{18}O_{ice}$. Condensed water is richer in heavy isotopes than the surrounding water vapor. Consequently, precipitation is more depleted heavier isotopes with increasing transport distance [51].*

and thus needs a calibration using complementary measurements such as borehole temperature measurements [53], [10] with the drawback of smoothing out fast surface temperature changes.

Reconstructing fast temperature changes can however be derived from stable inert gas isotopes (such as δ^{15}N) trapped in gas bubbles within the ice matrix (Chapter 2.2.2.1.
Hereinafter, the notation δ^{18}O is used for stable water isotope signals of ice core water samples.

2.4 Inverse Modeling

The aim of this project is to reconstruct surface temperature histories from δ^{15}N abundances in gas bubbles enclosed in ancient ice. For this purpose, the CFM which models firn densification, heat diffusion and gas diffusion is inverted by commonly used minimizers provided by the `scipy.optimize` library [54]. Two algorithms are chosen for the inversion of the CFM: the Nelder-Mead algorithm and a least squares method based on a trust region reflective algorithm. In the following two sections, it will be roughly explained how these algorithms work.

2.4.1 Nelder-Mead

The Nelder-Mead method is a numerical method to find the minimum or maximum of a function f. It is a direct method which means that it calculates the value of f and compares it to other values of f and does not use derivatives. The Nelder-Mead method is selected for this project since it is a robust method and was also used previously for the same type of inverse problem [24], [54].

The Nelder-Mead method uses a simplex which is a shape consisting of $n + 1$ vertices in n dimensions. This means for a function f dependent on two variables the simplex is a triangle, for a function dependent on three variables it is a tetrahedron, etc.

In the following, it will be explained how a local minimum of f dependent on two variables x_1 and x_2 is found using Nelder-Mead.

As a first step, three arbitrary points in space $\boldsymbol{u}$, $\boldsymbol{v}$ and $\boldsymbol{w}$ are picked. Then, f is evaluated at these three points and the points are subsequently renamed such that:

$$f(\boldsymbol{u}) < f(\boldsymbol{v}) < f(\boldsymbol{w}). \tag{2.46}$$

$\boldsymbol{u}$ thereby represents the best performing point and $\boldsymbol{w}$ the least best performing point for f.
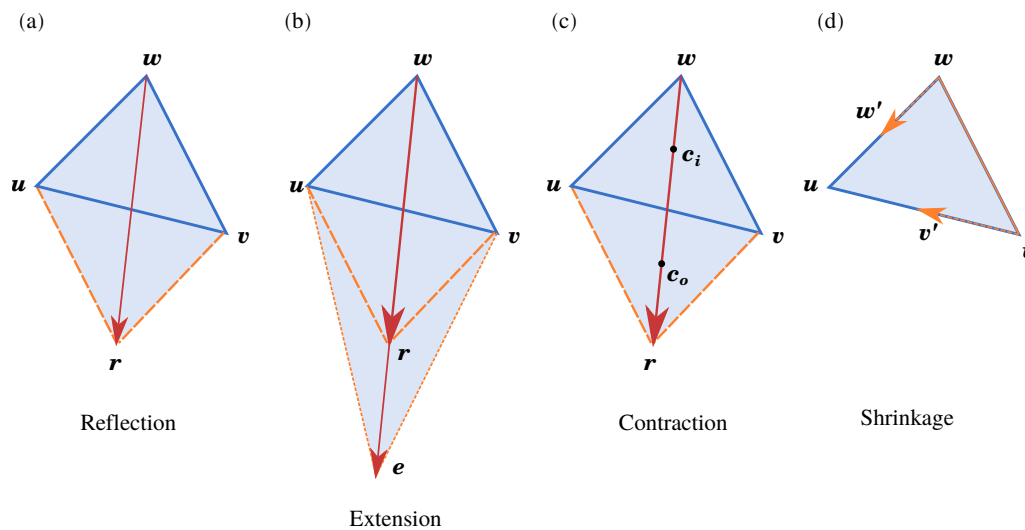
Figure 2.7: *Simplex operations of the Nelder-Mead algorithm. Adapted from [55].*

In the next step, the least best performing point $\boldsymbol{w}$ is reflected through the centroid of the remaining points $\boldsymbol{u}$ and $\boldsymbol{v}$ (compare Figure 2.7 (a)). The reflected point is hereinafter called $\boldsymbol{r}$. Then f is evaluated at $\boldsymbol{r}$. If $f(\boldsymbol{r})$ is smaller than $f(\boldsymbol{v})$ but larger than $f(\boldsymbol{u})$, then $\boldsymbol{w}$ is replaced with $\boldsymbol{r}$ and $\boldsymbol{r}$ becomes the worst performing point.

If $f(\boldsymbol{r})$ is smaller than $f(\boldsymbol{u})$ and $f(\boldsymbol{v})$, the reflected point is extended by the vector between the centroid (between $\boldsymbol{u}$ and $\boldsymbol{v}$) and the reflected point $\boldsymbol{r}$ in order to go further into the direction

which already seems to work out well (compare Figure 2.7 (b)). The extended point is called e. e replaces w if $f(e)$ is smaller than $f(r)$. If $f(e)$ is larger than $f(r)$ r replaces w.

In the case that the reflection point r performs worse than all other points u, v and w the simplex is contracted in two different ways using the contraction point c_i and c_o (compare Figure 2.7 (c)). c_i is the inside contracted point which is on 1/4 of the way between w and r and c_o is the inside contracted point which is on 3/4 of the way between w and r. f is evaluated at both points and if one of them outperforms v, the best performing point among them replaces w.

If all of these attempts fail, the simplex will shrink towards u (Figure 2.7 (d)) and the procedure starts from new [55], [56].

2.4.2 Least-Squares

The `least_squares` method provided by `scipy.optimize` solves a non-linear least squares problem

$$f(x) = \sum_i^N \|y_i - g_i(x)\|_2{}^2 = \sum_i^N \|r_i(x)\|_2{}^2, \tag{2.47}$$

where r_i are the residuals which are defined as the difference between observed values y_i and values predicted by a model $g_i(x)$.

The `least_squares` function provides three methods to solve the non-linear least squares problem (e.g. the Levenberg-Marquardt algorithm, the dog-box algorithm and the trust region reflective algorithm). For this project the trust region reflective algorithm is chosen since it is very robust and suitable for large problems [54].

The idea of the trust region reflective algorithm is to approximate f in a certain region (the trust region) with $\tilde{f}$ which is often chosen to be a quadratic approximation of f:

$$f(x) \approx \tilde{f}(x) = f(c) + \nabla f(c)^T(x - c) + \frac{1}{2!}(x - c)^T H(c)(x - c), \tag{2.48}$$

where ∇f is the gradient, H the Hessian matrix with respect to the independent variables and c being the center of the selected region. Then, the minimum of $\tilde{f}$ is determined within the trust region. The new point for the next iteration is then the point that minimizes $\tilde{f}$ within the trust region [57]. A schematic drawing of the trust region algorithm is shown in Figure 2.8.

In order to determine a suitable trust region radius it is tested how well the quadratic model fits f within the trust region. This is measured by comparing the actual reduction

$$ared = f(c) - f(t), \tag{2.49}$$

where t is the new trial point, with the predicted reduction

$$pred = \tilde{f}(c) - \tilde{f}(t). \tag{2.50}$$
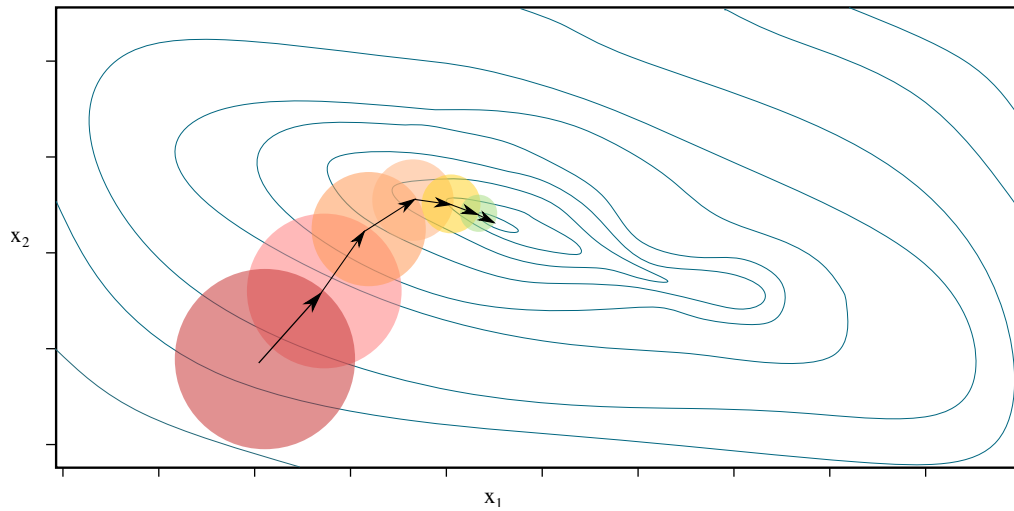
Figure 2.8: *Schematic drawing of trust region algorithm. The trust region reflective algorithm approximates the function f to be minimized by $\tilde{f}$ within a trust region (highlighted as colored circles). The point within the trust region that minimizes $\tilde{f}$ is the new center for the next trust region.*

Whether the trial step is rejected or accepted or the trust region radius is increased or decreased depends on the ratio between *ared* and *pred*. For ratios typically below 0.0001, the new trial point is rejected, and/or the trust region should be decreased if the ratio is below 0.25. The trust region is typically increased if the ratio is above 0.75 [58].

Chapter 3

Materials and Methods

The aim of this project is to deduce surface temperature histories in Greenland at North GRIP during the Last Glacial Maximum from stable nitrogen gas isotopes enclosed in ancient ice and to investigate the sensitivity of temperature to the usage of different densification models and different gas diffusion parameterizations. The main approach is thereby to model stable nitrogen gas isotope distributions using the `firn_air` module of the CFM and to exploit the correlation between stable water isotopes of ice and surface temperature or temperature of precipitation formation respectively. Assuming a linear relationship between surface temperature and $\delta^{18}O$ ($T = 1/\alpha \cdot \delta^{18}O + \beta$) one can fit $\delta^{15}N_{model}$ to $\delta^{15}N_{data}$ by using a minimizer (e.g. least squares) and finding the optimal parameters α_{opt} and β_{opt} (Figure 3.1). This chapter describes the complete workflow from data preprocessing, to running (and optimizing) the CFM and building the minimizers.
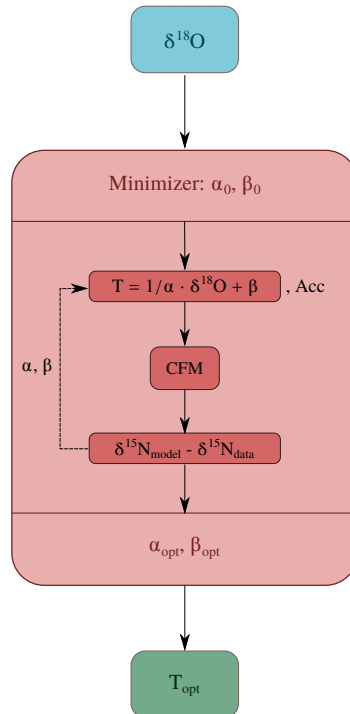
Figure 3.1: ***Workflow for surface temperature reconstruction.*** *Rough scheme of the workflow for finding the optimal surface temperature T_{opt} from stable nitrogen gas and stable water distributions.*

3.1 Data

Past surface temperature histories are reconstructed by using $\delta^{15}N$, $\delta^{18}O$ and accumulation data from North GRIP ice core drilling site located at $75.10\,°N$ and $42.32\,°W$ (Figure 3.2) covering a time period from 10 to $120\,kyr$ b2k. The whole datasets of measured $\delta^{15}N$ and $\delta^{18}O$ as well as the accumulation and temperature histories reconstructed by [1] are depicted in Figure 3.3. The used time chronology is the Greenland Ice Core Chronology 2005 (GICC05) and GICC05modelext, respectively. GICC05 is based on annual layer counting until $60.2\,kyr$ b2k. GICC05modelext is the extension of GICC05 for ages older than $60.2\,kyr$ and uses the ss09sea06bm timescale which is shifted by $705\,yr$ to younger ages [59], [60], [61], [62], [63]. The full data set used for this thesis and Python modules to read and preprocess data are available on `github`: `https://github.com/klimakathi/CFM_Kathi.git`

Note: Contrary to convention ages ages older then the year 2000 are indicated with negative values in this thesis, e.g. $120\,kyr$ b2k is indicated as $-120\,kyr$. Consequently, plots have to be read from left to right with older ages on the left hand side and younger ages on the right hand side.
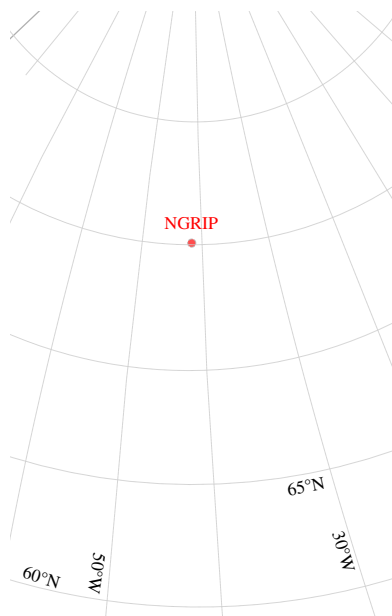
Figure 3.2: *Location of North GRIP ice core drilling site.*
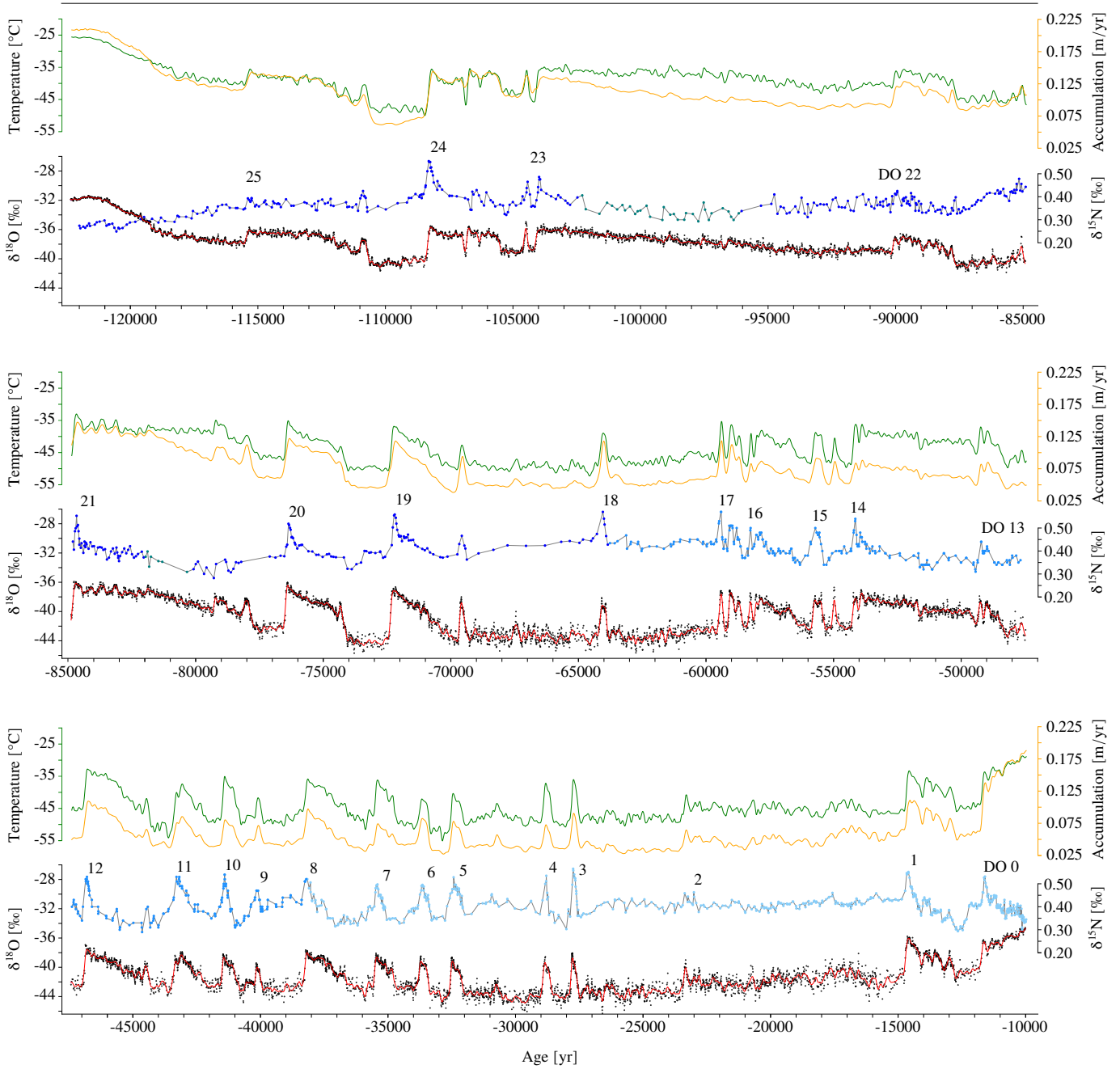
Figure 3.3: Full data set used for temperature history reconstructions during the Last Glacial. *Green: Accumulation rate in m ice/ yr [1] to agree with Kindlers temperature reconstruction.; Orange: Temperature reconstruction by [1] using $\delta^{15}N$ data and a firn densification model coupled with heat diffusion. Blue points: $\delta^{15}N$ on gas age scale measured by : ● [64], [65], [66], [67], [66], ● [1], ● [22], ● [1]; Black points: $\delta^{18}O$ on ice age scale. Red: Cubic smoothing spline through $\delta^{18}O$ data points with a cut-off frequency of $1/200\,\mathrm{yr}^{-1}$. Adapted and modified from [1].*

3.1.1 δ^{15}N Data

In order to measure isotopic compositions of δ^{15}N air bubbles are extracted from the ice and isotopic compositions are determined using Isotope Ratio Mass Spectrometry (IRMS) [1]. The full dataset of δ^{15}N as also used in [1] contains measurements from Climate and Environmental Physics Division (KUP) of the Physics Institute at the University of Bern and from Laboratoire des Sciences du Climat et de l'Environnement (LSCE), Gif-sur-Yvette published in [1], [65], [22], [67], [68], [64], [66] (compare Table 3.1, Figure 3.3). Uncertainties for δ^{15}N are 0.02 ‰ and 0.006 ‰ measured at KUP and LSCE, respectively (compare Table 3.1).

Data sets are available including δ^{15}N versus depth and depth versus ice and gas age on the GICC05modelext timescale [62], [63].

In order to read the data from the data set and get gas ages and ice ages of available δ^{15}N data points the module `read_d15N.py` is implemented. This module provides the methods `get_d15N_data` and `get_d15N_data_interval` which return δ^{15}N and corresponding gas age and ice age either for the full dataset or for a given ice age interval. The two methods exploit the SciPy class `scipy.interpolate.interp1d` in order to linearly interpolate gas ages and ice ages to the depths where δ^{15}N data points are available.

Period	Age [yr b2k]	NGRIP depth [m]	Measured at	Uncertainty [‰]
Holocene to DO 8	$9961 - 39746$	$1391.11 - 2092.52$	KUP [1]	0.02
DO 8 to DO 17	$39212 - 63972$	$2085.50 - 2463.83$	KUP [22]	0.02
DO 18, 19, 20	$63986 - 80162$	$2464.09 - 2620.24$	LSCE [65]	0.006
GI-21	$80383 - 82218$	$2623.07 - 2649.47$	LSCE [1]	0.006
GS-22, GI-21	$82281 - 89830$	$2650.45 - 2743.95$	LSCE [67]	0.006
GS-23, GI-22	$89875 - 95360$	$2744.5 - 2796.65$	LSCE [68]	0.006
GS-23	$95765 - 102524$	$2800.72 - 2873.87$	LSCE [1]	0.006
DO 23 to 25	$102668 - 122183$	$2875.44 - 3083.33$	LSCE [64], [66]	0.006

Table 3.1: *Overview of $\delta^{15}N$ measurements performed at North GRIP and corresponding uncertainties. GS and GI denote glacial stadial and glacial interstadial, respectively. Adapted from [1].*

3.1.2 δ^{18}O Data

δ^{18}O values versus depth and age are available from [69]. In order to read δ^{18}O values and corresponding ages from the dataset the module `read_d18O.py` is implemented. The methods `read_data_d18O` and `get_interval_data_noTimeGrid` read the whole data or data within a certain age interval respectively. In order to filter fast changes in δ^{18}O the module `smoothing_splines.py` is implemented which exploits the Python library `csaps` with the method `CubicSmoothingSpline` [70]. This module serves as low-pass filter and fits cubic splines to the data points [71]. The cut-off frequency is chosen to $f_{\text{cut-off}} = 1/200 \, \text{yr}^{-1}$ which means

that all frequencies higher than $f_{\text{cut-off}}$ are filtered out in order to reduce the influence of noise in the data.
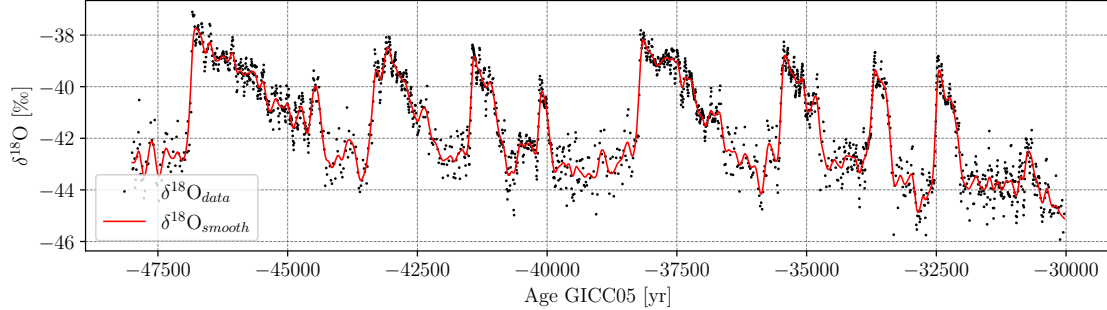
Figure 3.4: *Smoothed $\delta^{18}O$ signal using cubic smoothing splines.* *$\delta^{18}O$ smoothed with cubic smoothing splines using a cut-off frequency of $1/200\,\text{yr}^{-1}$.*

Cubic Smoothing Splines The cubic smoothing spline f is constructed based on the trade-off between minimizing the two functions

$$S = \sum_{j=1}^{n} w_j |y_j - f(x_j)|^2 \quad \text{and} \tag{3.1}$$

$$Q = \int \left[\frac{\mathrm{d}^2 f(t)}{\mathrm{d}t^2} \right]^2 \mathrm{d}t, \tag{3.2}$$

where y_j denote the data points f should be fitted to and w_j are weighing factors. The first term S is an error measure and the second term Q is roughness measure [**?**]. The smoothing spline f then minimizes

$$pS + (1-p)Q, \tag{3.3}$$

where p is the smoothing parameter calculated according to [71] as:

$$p = \frac{1}{1+\lambda} \quad \text{and} \tag{3.4}$$

$$2\pi f_{\text{cut-off}} = (\lambda \Delta t)^{\frac{1}{4}}, \tag{3.5}$$

with Δt the mean distance between the data points.

3.1.3 Accumulation Rates and Surface Temperatures

The net accumulation rate is recorded in the layer-thickness profile based on the measured δ^{18}O signal obtained from ice cores. The used accumulation rates are reconstructed by [1] who reduced the original accumulation rates of the SS09sea06bm chronology by up to 20 % in some time intervals to match measured δ^{15}N data with modeled δ^{15}N signals.

The surface temperatures presented in Figure 3.3 are the surface temperatures reconstructed by [1] who also exploited the correlation between $\delta^{18}O$ and temperature. By using a firn densification model coupled with heat and gas diffusion [1] calculated stable nitrogen gas isotope distributions and tried to find the optimal parameters α and β in order to find the best fit of modeled $\delta^{15}N$ distributions to $\delta^{15}N$ data. The reconstructed surface temperatures are used at a later point as a comparison to the surface temperature histories reconstructed in this thesis.

3.2 The Community Firn Model

The CFM is an open-source framework that provides several modules for the simulation of various physical processes in the firn, such as firn densification [32], [34], [33], gas diffusion [44], [20], [45], [29],, water isotope diffusion [72], heat transport [73], and meltwater percolation [74] and refreezing [74], [75]. The focus in this work is set on firn densification and firn-air diffusion.

The CFM is implemented in Python and runs on Python versions 3.6+. In this thesis CFM version 1.1.6 is used including the most recent adjustments for the Sigfus densification model of CFM version 1.1.11.

Density is calculated explicitly in the CFM:

$$\rho_{\text{new}} = \rho_{\text{old}} + \frac{d\rho}{dt} \cdot dt. \tag{3.6}$$

The model grid is a one-dimensional Lagrangian (particle/material-following) grid with a fixed number of volume elements. For each time step accumulation is added to the top of the firn column as new volume element, and one volume element is removed from the bottom.

The CFM runs using a .json file which specifies the configurations for the model run. Furthermore, it requires temperature and accumulation forcing input files. The forcing files must be csv formatted and contain temperature and accumulation forcing at the respective time steps. Using `timesetup: "interp"` (to be specified in the .json file) allows for specifying only years that denote a change in the temperature / accumulation forcing. The CFM then "uses a uniform dt and interpolates the input data onto the timeline that the model generates." [25]. A short example is presented in Table 3.2.

The most important parameters specified in the .json file used for these experiments are listed in Chapter A.

3.2.1 Running the CFM

The CFM run starts with a spin-up run which initializes the firn column and computes densification coupled with heat diffusion according to the chosen firn densification physics in a certain time interval specified in the .json file (`yearSpin`). The parameters calculated for the last time step during the spin-up are used to initialize the firn column for the main run which

	.csv
Time steps [yr]	-115000, -114991, -114978, -114969
Temperature forcing [°C]	-36.6, -36.7, -36.9, -37.1
Time steps [yr]	-115000, -114991, -114978, -114969
Accumulation [m ice equ./yr]	0.112, 0.113, 0.121, 0.122

Table 3.2: ***Formatting of temperature and accumulation forcing files.*** *Simple example for the formatting of temperature and accumulation forcing files including a temperature and accumulation rate curve between the years* -115000 *and* -114969.

uses the given input surface temperatures and accumulation rates. Specified outputs are saved in .hdf5 format containing a set of firn columns over a specified timegrid.

Spin Run   The spin run initializes a firn column defined by depth, density, age and temperature with a fixed grid length. The grid length of the firn column is defined over the initial thickness of the firn column (`H - HbaseSpin`, compare Chapter A) divided by the initial or mean accumulation in meters in ice equivalent per specified time step.

During the first time step in the spin run the Herron and Langway model is used which models the steady-state firn density, age profiles, and bubble close-off using the first or mean entry of the temperature and accumulation forcing files. It returns age and density for each firn/ice volume with corresponding depths. For the subsequent time steps the densification model specified in the configuration .json file is used. The CFM is forced with the first surface temperature and accumulation rate values in the .csv input files.

The CFM allows for the coupling of densification models to heat diffusion by enabling the heat diffusion module (”`HeatDiff`”: `true`). The heat diffusion module solves the heat diffusion equation according to Patankar's approach to solve the general differential equation [73]. All experiments are performed with enabled heat diffusion using the thermal conductivity of firn parameterized by [76].

For each time step a model grid update is performed. The spin up module returns the model outputs depth, density, age of the ice and temperature at the last time step of the spin up. These outputs are then used as initial state for the ”no-spin” or main run [25]. A flowchart explaining the procedures during the Spin-up run is depicted in Figure 3.5.

Main Run   The firn column of the main run is initialized with the parameters from the last time step of the spin run. Contrary to the spin run, it is possible to enable firn air diffusion in the main run. The firn air module can solve the firn air diffusion / firn air transport equation (Equation 2.36) for various gases which can be specified in the `AirConfig.json` file. For the experiments in this thesis the `"gaschoice"` is set to `d15N2` since the focus is on stable nitrogen gas isotopes. Furthermore, it is possible to specify the depth of the convective zone. `"ConvectiveZoneDepth"` is set to $1.5\,\mathrm{m}$ according to [26] which reflects a modern value for Greenland at North GRIP location. Additionally, it is possible to specify the
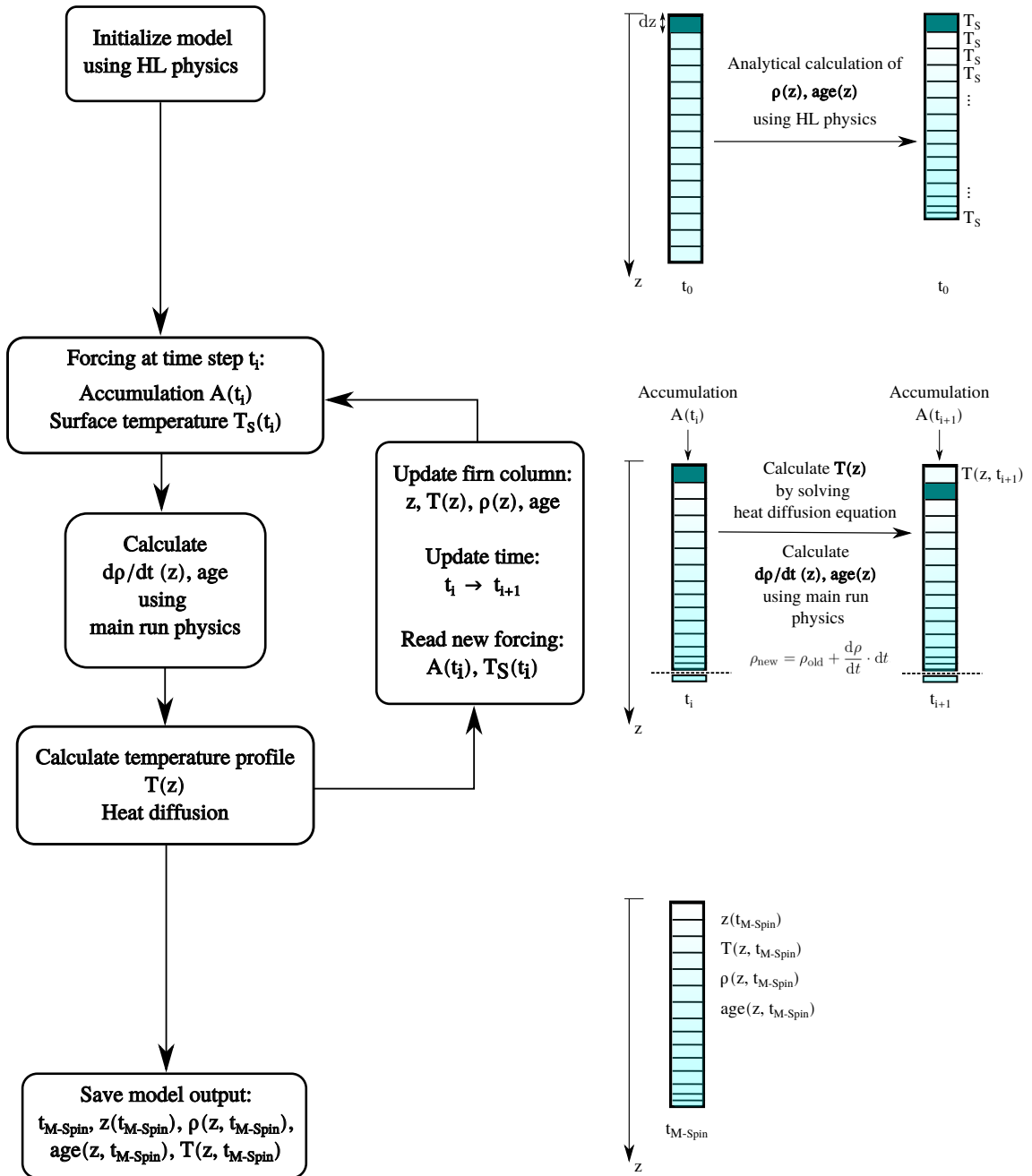
Figure 3.5: *Computation flow diagram of Spin-up run of the CFM.* *The spin-run of the CFM builds a firn column characterized by depth, density, age of the firn/ice and temperature. The firn column of the last time step is saved and used to initialize the firn column for the main run.*

Initialize model
from Spin-run
Output

Forcing at time step t_i:

Accumulation $A(t_i)$
Surface temperature $T_S(t_i)$

Calculate
$d\rho/dt$ (z), age
using
main run physics

Calculate temperature profile
$T(z)$
Heat diffusion

Firn air diffusion
Calculate $w_{firn}(z)$, $C_{15N}(z)$, $D(z)$,
gas age(z)

Update firn column:
z, $T(z)$, $\rho(z)$, age,
$w_{firn}(z)$, $C_{15N}(z)$, $D(z)$,
gas age(z)

Update time:
$t_i \rightarrow t_{i+1}$

Read new forcing:
$A(t_i)$, $T_S(t_i)$

Save model output:
t, z(t), $\rho(z,t)$, age(z,t), $T(z,t)$,
$w_{firn}(z,t)$, $C_{15N}(z,t)$, $D(z,t)$,
gas age(z,t)

$z(t_{M\text{-}Spin})$
$T(z, t_{M\text{-}Spin})$
$\rho(z, t_{M\text{-}Spin})$
age$(z, t_{M\text{-}Spin})$

t_0

z

Accumulation
$A(t_i)$

Accumulation
$A(t_{i+1})$

Calculate $\mathbf{T(z)}$
by solving
heat diffusion equation

$T(z, t_{i+1})$

Calculate
$d\rho/dt$ (z), age(z)
using main run
physics

$\rho_{new} = \rho_{old} + \dfrac{d\rho}{dt} \cdot dt$

t_i

Calculate $w_{firn}(z)$, $C_{15N}(z)$,
$D(z)$, gas age(z) by solving
firn air diffusion equation

t_{i+1}

z

t_0 t_1 t_2 t_3 t_4 ... $t_{M\text{-}Main}$

z

Figure 3.6: *Computation flow diagram of Main-up run of the CFM. Contrary to the spin run, it is possible to include firn air diffusion in the main run. The CFM* `solver.py` *module solves the firn air diffusion equation (Equation 2.36). The output is saved as a time series of firn columns with parameters as specified in the .json file.*

parameterization of the diffusion coefficient D (here: `"Diffu_param":` `"Schwander"` [46]),
the parameterization of the firn air advection (here: `"advection_type":` `"Christo"` [48])
and the types of firn air fractionation (here: `"thermal":` `"on"`, `"gravitational":` `"on"`).
The firn air diffusion equation is solved using the same `solver.py` module as for heat diffusion.
It returns the concentration C of stable nitrogen gas isotopes and the firn air advection rate
w_{air}. Figure 3.6 depicts the computation flowchart of the main run.

One major drawback of the firn air module for these experiments is that the firn air is initialized
from scratch in the main run since firn air diffusion is only applicable in the main run. Values
of ^{15}N are initialized with an array of ones. In order to get a full column with reasonable
values, which means $\neq 1$, the main run has to run for as many time steps as firn boxes are
present within the model grid. This leads to an unnecessary loss of modeled $\delta^{15}N$ data in
the beginning of the main run (and computation time). In order to overcome this problem a
module `SecondSpin.py` is implemented which will be introduced in Chapter 3.2.4.

3.2.2 Model Outputs

General Model Outputs   The CFM saves all outputs specified in the `.json` configuration
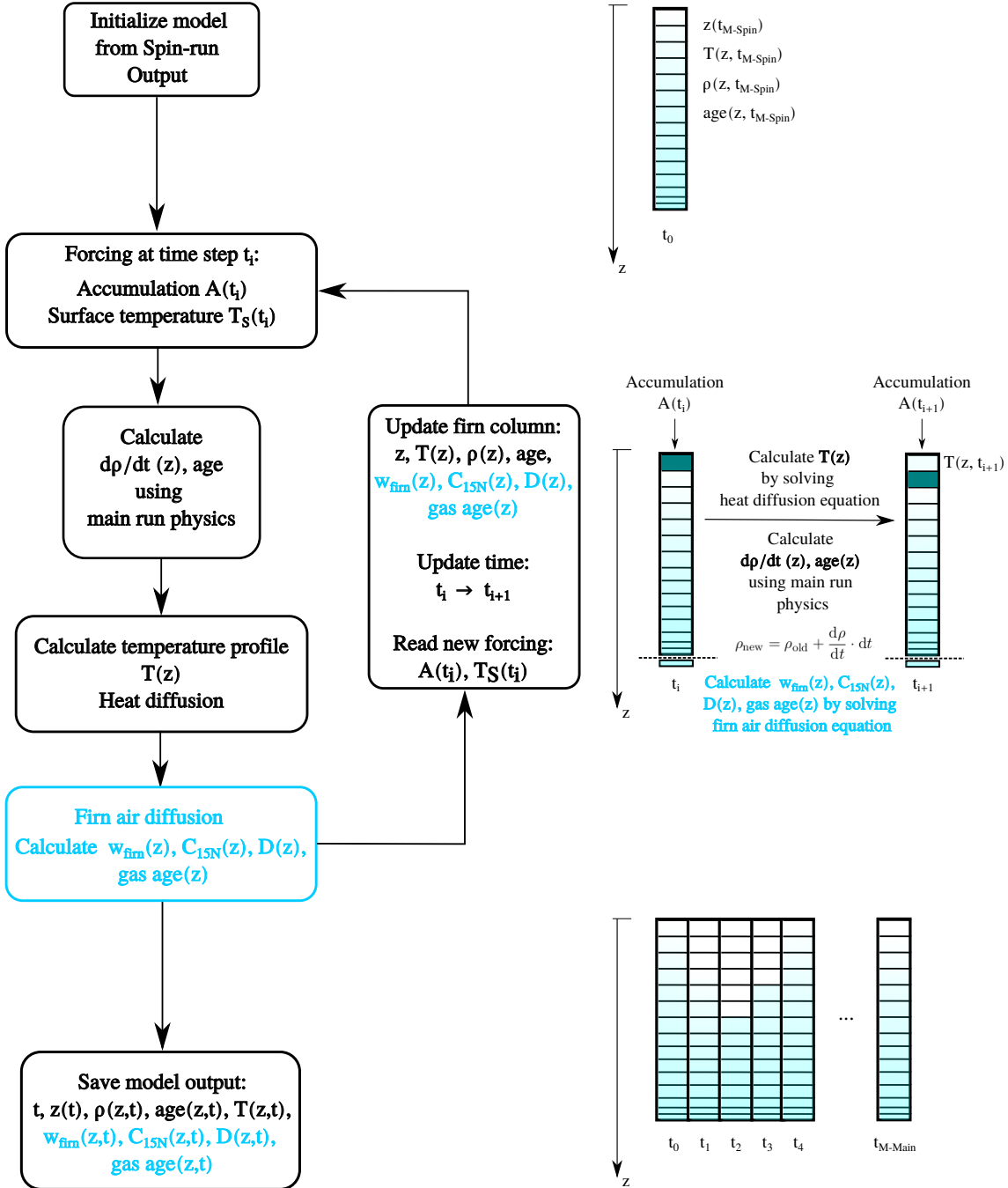file in an `results.hdf5` file. For the experiments of this thesis, the following outputs are
saved: "BCO", "Modelclimate", "age", "d15N2", "density", "depth", "diffusivity", "forcing",
"gas_age", "temperature", "w_air" and "w_firn". Most of the output files are saved as two-
dimensional arrays, with one dimension being the depth of the firn column and the other
dimension the modeltime. One-dimensional arrays (Modelclimate, forcing and BCO) only
have the modeltime dimension. The forcing is hereby consisting of two arrays containing the
values of the input forcing `.csv` files. Modelclimate is the temperature and accumulation
forcing interpolated to the modeltime. BCO is a set of several 1D arrays containing among
others the close-off depth and lock-in depth defined according to Martinerie [27], [31].

Figure 3.7 shows most of the model outputs of the CFM run using Barnola's densification
model and activated firn air diffusion module. Furthermore, it is shown how the model outputs
change with time due to a change in the surface temperature forcing. In Figure 3.7 (b) the
density-depth profile is shifted towards higher densities with the change of temperature forcing
toward higher values with is related to the Arrhenius activation energy theorem predicting
a higher level of crystallization within the firn with higher temperatures. The $\delta^{15}N$ isotope
signal in (c) first shows an almost linear progression for all times t_i starting from $\delta^{15}N= 0$
(atmospheric values) until the close-off depth is reached and the isotope ratios cannot change
anymore. For t_0 the first part of the curve is linear, since only gravitational diffusion happens
which has a linear dependence on depth (compare Equation (2.30)). For later times there is
a small deviation from a linear curve visible which is due to thermal diffusion induced by a
change in temperature forcing (compare Equation (2.31)). As the close-off depth decreases the
isotope signal gradually shifts toward lower $\delta^{15}N$ values. The equilibrium after the temperature
forcing is reached again when the $\delta^{15}N$ value in the ice does not change anymore. For both
$\delta^{15}N$ plots in (c) and (d), a drop to $\delta^{15}N= 0.0\,\permil$ is visible which is due to the fact that
^{15}N ratios are only initialized and modeled in the main run of the CFM. In order to yield
reasonable values for ^{15}N ratios after their initialization with an array of ones, the model

has to run for a certain amount of time until nitrogen gas isotopes diffused to the close-off and closed up isotopes advected down the ice column within the ice matrix. (e) depicts how the temperature within the firn/ice column changes over time due to the change in surface temperature forcing. The close-off depth in (f) has a very similar shape to the temperature forcing which is related to the fact that with higher temperatures, higher densities are reached, and thus smaller close-off depths.
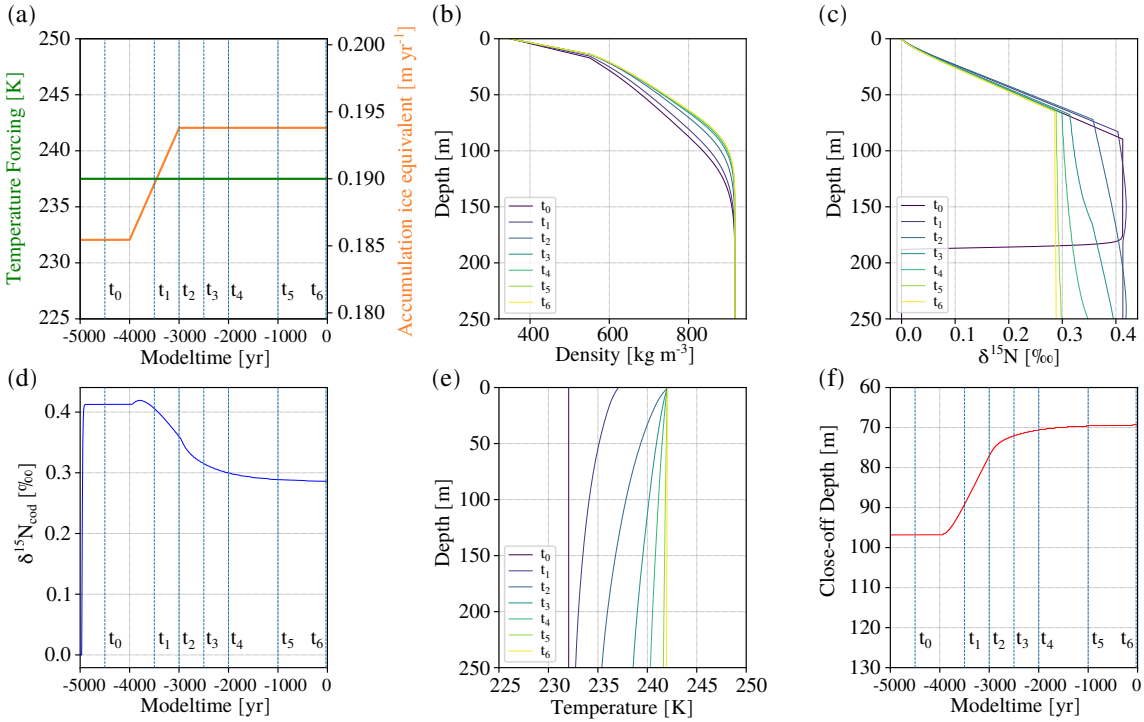
Figure 3.7: *CFM model outputs tracked with time using the firn densification model according to Barnola and the firn diffusion module.* *(a) Surface temperature and accumulation rate forcing. (b) Change of density with time depending on the temperature forcing. (c) Change of $\delta^{15}N$ with depth at different time steps during the model run. For t_0 the curve shows an abrupt jump to 0.0 ‰ which is an artefact of the initialization of $\delta^{15}N$ ratios with ones in the main run. (d) $\delta^{15}N$ at close-off depth. The same artefact as in (c) is present in the beginning of the model run. (e) Change of temperature within the firn column for different time steps in the model run. (f) Change of close-off depth with time.*

$\delta^{15}\mathbf{N}$ **and** $\Delta\mathbf{age}$ The parameter important for the temperature reconstruction by inverting the CFM is $\delta^{15}N$ at lock-in depth. The CFM gives lock-in depths and close-off depths according to Martinerie as output (BCO). It is then possible to determine the corresponding $\delta^{15}N$ value at lock-in or close-off as well as corresponding ice age and gas age at lock-in or close-off.

Knowing ice age and gas age at lock-in depth/ close-off depth allows then for the calculation of Δage.

The module `read_d15N.py` is implemented to read δ^{15}N at close-off depth, lock-in depth or the depth where the diffusivity becomes zero. It further returns corresponding ice age, gas age and Δage.

Figure 3.8 shows some exemplary outputs of δ^{15}N plotted at close-off depth, lock-in depth and depth where the diffusivity becomes zero against ice age (b) and gas age (c), respectively. Figure 3.8 (d) shows corresponding Δages. The CFM is forced with temperatures and accumulation rates depicted in (a) and ran with a time resolution of 2 yr using Barnola's firn densification model and the firn air diffusion model.

It is visible that δ^{15}N values plotted on ice age scale and gas age scale are shifted against each other. δ^{15}N on ice age scale describes the age of the ice when the nitrogen gas gets trapped in gas bubbles. δ^{15}N on gas age scale instead refers to the age of the nitrogen gas. It is assumed that gases travel almost instantaneously through the firn. The gas age at lock-in depth is thus 0 yr and at close-off depth a little bit older (in this example in the range between 15 yr and 65 yr).

δ^{15}N values for different depths (lock-in, close-off and zero diffusion) are very similar which is reasonable since the vertical motion of gases is hampered as soon as sealing layers appear (lock-in depth). δ^{15}N for the different depths on gas age scale are slightly shifted against each other which is most likely due to the different Δages associated with the respective depth (compare Figure 3.8(d)).

For very quick and big changes in temperature δ^{15}N are strongly oscillating for a short interval of time which is most probably due to some numerical instability when calculating firn air diffusion since no in-continuities occur in the close-off depth and lock-in depth, respectively (compare Figure B.1).

3.2.3 Speeding up the Community Firn Model

Running the CFM with activated firn air diffusion module and heat diffusion module requires 1220 s in computation time for the time interval from -50 kyr to -30 kyr (modeltime of 20 kyr), an initial firn column of 550 m and yearly time resolution. Since the model is supposed to be inverted, which requires several 10 to 100 model runs depending on the inversion method, and several inversions need to be performed, one goal of this project is to reduce the computation time of the model. Thereby, three different approaches are followed. The first approach is to try to compute on GPUs instead of CPUs allowing for parallel data processing and thus lower computation times [77]. The second approach is to identify the bottlenecks in the CFM code base and to optimize computation times using the Python library Numba which allows for faster computation times by translating NumPy code and a subset of Python code into fast machine code [78]. The third approach dealt with the reduction of the model grid length which is defined by the depth of the initial firn column, time step length and accumulation rate.
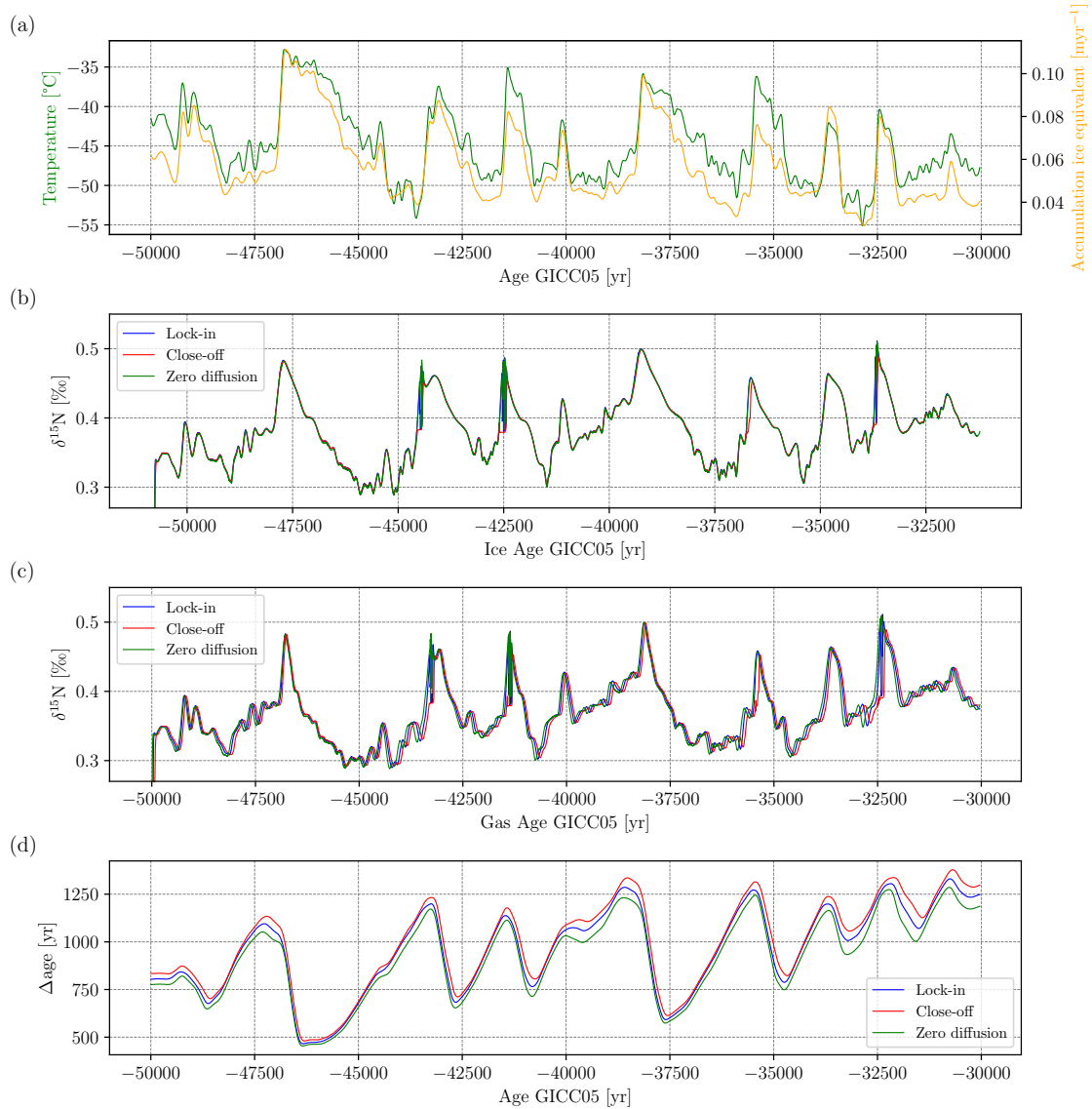
Figure 3.8: $\delta^{15}N$ *and* $\triangle age$ *model outputs from the CFM. (a) Surface temperature and accumulation rate forcing (from Figure 3.3). (b)* $\delta^{15}N$ *at lock-in depth, close-off depth a depth where diffusivity becomes zero plotted on ice age scale. (c)* $\delta^{15}N$ *at lock-in depth, close-off depth a depth where diffusivity becomes zero plotted on gas age scale. (d)* $\triangle ages$ *associated with the lock-in depth, close-off depth and depth with zero diffusivity.*

3.2.3.1 Hardware

The first approach of speeding up the model is to use GPUs instead of CPUs. The library CuPy allows for GPU-accelerated computing with Python and can accelerate operations up to 100 times. Furthermore, CuPy is highly compatible with NumPy and SciPy which means that most NumPy and SciPy operations can be replaced by `cupy` and `cupyx.scipy`. The major

drawback of this approach is that CuPy utilizes CUDA Toolkit libraries which only support a certain set of GPUs. The available GPU is an NVIDIA GeForce GTX 1080 Ti not being supported by CUDA.

3.2.3.2 Bottlenecks
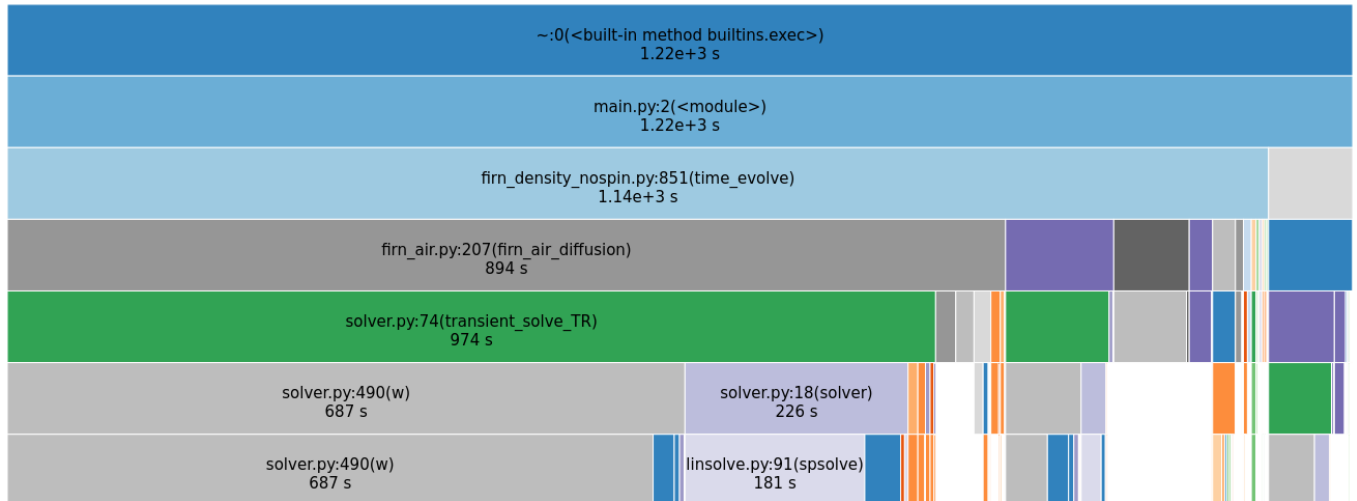
Figure 3.9: ***Profiling of CFM.*** *cProfile of CFM running with temperature and accumulation rate forcing from Chapter 3.1 in the time interval between -50 kyr and -30 kyr with an initial firn column of 550 m and yearly time resolution using Barnola's densification model and Buizert's firn air advection parameterization. The grid length of the model is 8888. The profiling is performed with* `cProfile` *and visualized with* `SnakeViz`*.*

As a second approach, the Python library Numba is used. Numba is a just-in-time compiler for Python that is able to transform Python code into machine code. It supports many NumPy operations but does not work with all variable types e.g. dictionaries, strings and tuples (check for accepted variable types on [79]). Since the CFM uses also other variable types than NumPy arrays (e.g. Python dictionaries, strings) a profiling of the code base is performed in order to identify the methods that are most heavy in computation time and to only rewrite these methods in Python code that can be compiled with Numba. The bottlenecks of the CFM are identified with `cProfile` which tracks the total time each method takes that is called during the model run. For the profiling, the CFM is running with temperature and accumulation rate forcing from Chapter 3.1 in the time interval between -50 kyr and -30 kyr with an initial firn column of 550 m and yearly time resolution using Barnola's densification model and Buizert's firn air advection parameterization. The results of the profiler are visualized in Figure 3.9. Out of a total model run time of 1220 s (top blue bar) the `firn_air` module uses most of the time with 894 s. The `firn_air` module calls the `solver` module which solves the firn diffusion

equation and calculates the advection rate of firn air with the function `w()`. `w()` uses a total time of 687 s which is why the focus is set on optimizing `w()`.

`w()` receives a dictionary as input which contains several firn parameters saved as NumPy arrays such as depth, temperature, open and closed porosity, the ice matrix advection rate, etc. Since Numba cannot deal with dictionaries, `w()` is rewritten such that it receives the NumPy arrays directly instead of the dictionary containing the arrays. `w()` then calls several NumPy operations which are all supported by Numba except `np.gradient()` and `np.size()` according to [79]. In order to overcome this problem the gradient is calculated outside `w()` and then given to `w()` as input. Furthermore, a separate function `calc_size()` is implemented only using NumPy operations supported by Numba in order to substitute `np.size()`.

After this procedure, `w()` could be compiled using Numba without any compilation errors, however the code ran slower than without using Numba (compare Figure 3.10(b)) which could mean that Numba falls back into object mode (variable types are indicated as "pyobject") because there is either a function called that is not supported by Numba or an unsupported variable type is used. Consequently, Numba cannot translate the Python code to machine code. After a thorough review of all variable types and used NumPy/Python operations no inconsistencies regarding supported NumPy operations or variable types (types would be denoted as pyobjects) could be found (compare `w_type_inspect.txt` and `test_numpy_operations.ipynb` on GitHub). The reason for this failure could be that there is still an incompatibility between the existing Python code and Numba that is not reported by `inspect_types()` and the compiler.

Figure 3.10 depicts the time tracking of `w()` (b) with a model run of the CFM using the model input from -50 kyr to -30 kyr (a). For the time tracking of `w()` and the most time consuming NumPy operations called by `w()` the `time` library is used [80]. It is visible that `w()` compiled with Numba (blue curve) takes more time than `w()` without using Numba (violet curve). Furthermore, the elapsed time for each time step is different which seems to correlate with the length of an array that the most time consuming NumPy operations called by `w()` (`np.transpose()` (denoted as T1), `np.reshape()` (denoted as reshape1 and reshape2)) are using as input: All of these functions use a NumPy array as input that has the length of `op_ind2`. `op_ind2` denotes all indices of the firn column array where the open porosity is unequal 0. It thus describes the firn column from the surface of the ice sheets til the lock-in depth (c). Since the lock-in depth highly depends on the temperature and accumulation rate input, the length of `op_ind` correlates with the CFM input and the lock-in depth, which also explains the variability in consumed time per function call in (c).

3.2.3.3 Model grid

As a third approach for the reduction of the total model run time the resolution of the firn column is reduced. This is achieved by decreasing the time resolution of the modeltime grid from 1 yr to 2 yr, 5 yr, 10 yr and 20 yr respectively. The reduction of the time resolution results in a lower resolution of the firn column array and thus in the reduction of total model run time (compare Figure 3.11) since the number of firn/ice volumes in the model grid is defined

(a)

(b)

(c)
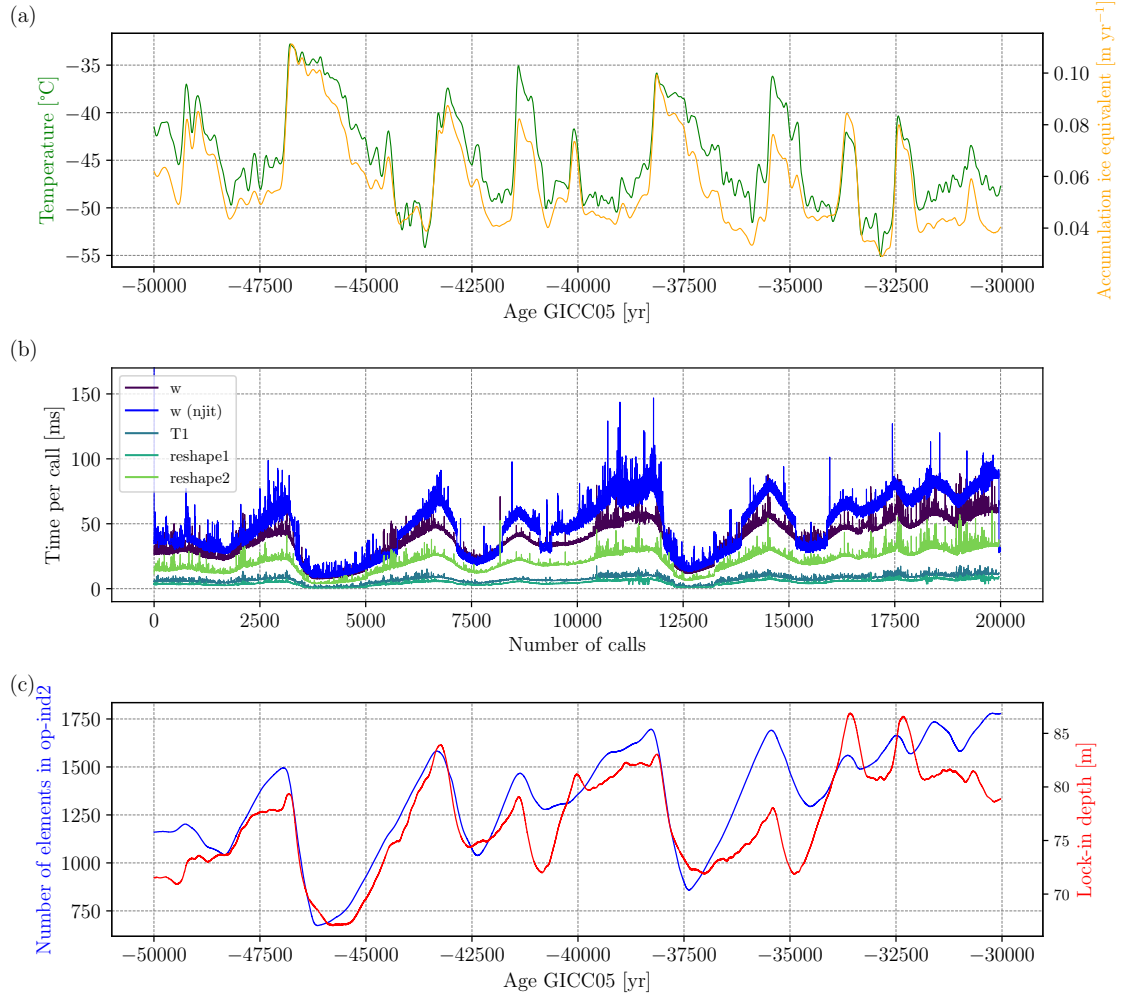
Figure 3.10: ***Time tracking of w()*** *(a) Surface temperature and accumulation rate input for the CFM. (b) Consumed time per function call of* ***w()*** *compiled with Numba (blue curve) and without Numba (violet curve). The green curves show time consumption by NumPy operations* ***np.transpose()*** *(T1) and* ***np.reshape()*** *(reshape1, reshape2) that are called by* ***w()*** *and which use an array of length of* ***op_ind2*** *as input.* ***op_ind2*** *describes the part of the firn column are the open porosity is unequal zero and thus correlates with the lock-in depth. The variability of the length of* ***op_ind2*** *explains the variability in time consumption per function call of* ***w()***, ***np.transpose()***, *and* ***np.reshape()***. *(c) Variability of length of array* ***op_ind2*** *and lock-in depth with time (and corresponding surface temperature and accumulation rate input).*

as [25]:

$$N = \frac{\mathtt{H} - \mathtt{HbaseSpin}}{\mathtt{bdot0}/\mathtt{stpsPerYear}}, \tag{3.7}$$

where H is the thickness of the ice sheet, HbaseSpin is the bottom height of the initial firn column, bdot0 is the first entry or mean of the accumulation rate per year in meters ice

equivalent and `stpsPerYear` is the number of time steps per year which define the modeltime grid. An experiment with the CFM is performed in order to investigate how a reduction
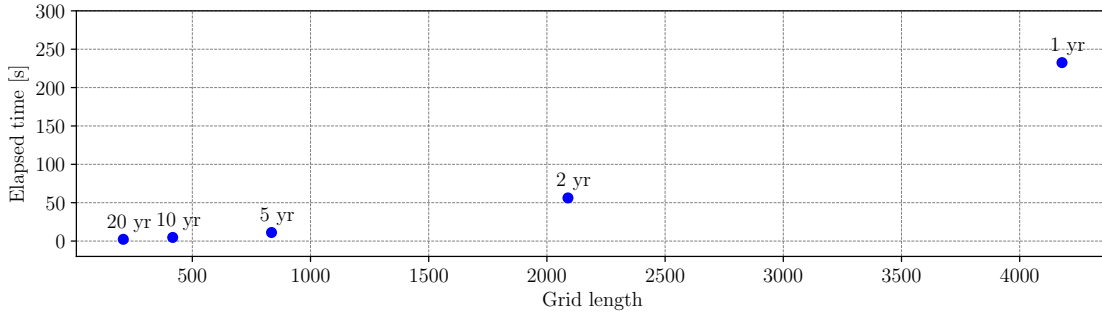
Figure 3.11: *Reduction of total model run time due to reduction of time resolution. A reduction of time resolution results in a decrease of the grid length of the firn/ice column and thus in a decrease in total model run time of the CFM. The CFM is forced with surface temperatures and accumulation rates depicted in Figure 3.12(a) and ran using Barnola's densification model and activated firn air module.*

in the model grid length affects the accuracy of modeled δ^{15}N. Thereby, a periodic surface temperature forcing with a frequency of $1/1000$ yr is used (see Figure 3.12 (a)):

$$T_\mathrm{S} = 240\,\mathrm{K} + 5 \cdot \sin\left(\frac{1}{1000\,\mathrm{yr}} \cdot 2\pi t\right). \tag{3.8}$$

Accumulation rates are chosen according to [72] and follow a logarithmic relation to temperature:

$$\ln(A) = -21.492 + 0.0811 \cdot T_\mathrm{S}. \tag{3.9}$$

The modeled δ^{15}N values at lock-in depth for different time resolutions are depicted in Figure 3.12(b). In order to measure uncertainties regarding the time resolution a standard deviation of δ^{15}N values at lock-in depth at 2 yr, 5 yr, 10 yr and 20 yr time resolution is calculated with respect to δ^{15}N values at 1 yr time resolution (which is assumed to deliver the most accurate results).

The standard deviations for a 2 yr and 5 yr time resolution are 0.0012 ‰ and 0.0055 ‰ respectively (see Table 3.3), which is within the smallest uncertainty of measured δ^{15}N (0.006 ‰) indicated in Table 3.1. For a 10 yr and 20 yr time resolution the standard deviations are clearly higher than the smallest uncertainty for measured δ^{15}N.
It is assumed that time resolutions with a standard deviation within or considerably smaller than the uncertainty range of measured data fulfill the criteria to yield reliable model results. Since a 2 yr time resolution results in the smallest standard deviation (approximately 4.5 times smaller than for 5 yr time resolution and 5 times smaller than the uncertainty for measured
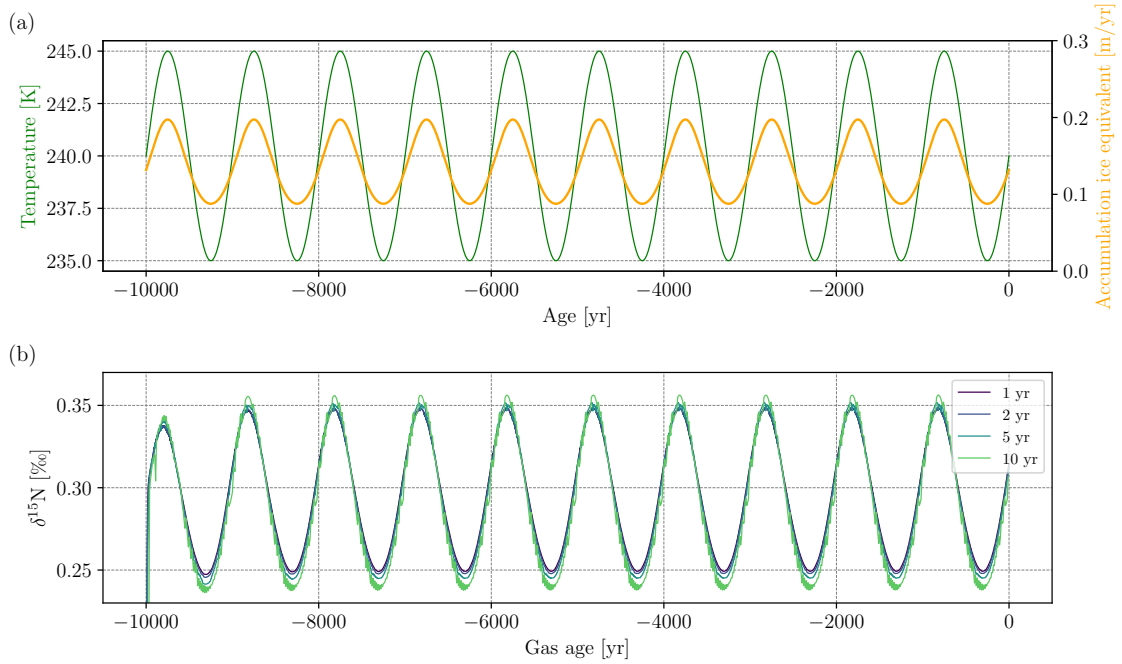
Figure 3.12: *Modeled $\delta^{15}N$ using different time resolutions. (a) Periodic surface temperature and accumulation rate forcing with a frequency of $1/1000\,\mathrm{yr}^{-1}$. (b) Modeled $\delta^{15}N$ at lock-in depth using the CFM with different modeltime resolutions. Note: $\delta^{15}N$ for time resolutions of $15\,\mathrm{yr}$ and $20\,\mathrm{yr}$ are not depicted because for both time resolutions $\delta^{15}N$ shows a very high variability and very high deviations from $1\,\mathrm{yr}$ resolution which would make the plot unreadable. However, standard deviations for all modeltime resolutions with respect to the $1\,\mathrm{yr}$ time resolution are specified in Table 3.3.*

δ^{15}N) and already a considerably lower model run time than the $1\,\mathrm{yr}$ time resolution (compare Figure 3.11) all following results are performed using a $2\,\mathrm{yr}$ time resolution.

Time resolution [yr]	2	5	10	20
Standard deviation σ [‰]	0.0012	0.0055	0.0134	0.0221

Table 3.3: *Uncertainties of modeled $\delta^{15}N$ using different time resolutions in the CFM.*

3.2.4 Second Spin

As mentioned in Chapter 3.2.4, it is not possible to include firn air diffusion in the spin run of the CFM and consequently no δ^{15}N values are calculated in the firn column. δ^{15}N values are initialized at the first time step of the main run with an array filled with ones. The drawback
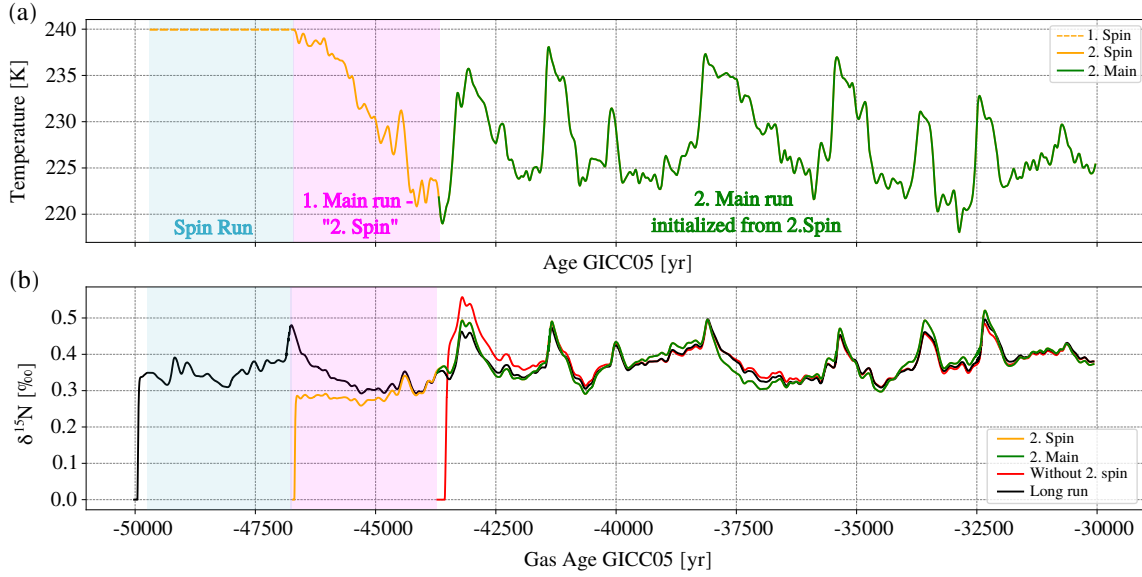
Figure 3.13: *Exemplary model run with and without second spin. (a) Temperature forcing including the constant temperature forcing (dashed orange line on blue background) the CFM creates internally for the spin run by using the first temperature value from the temperature forcing file. The solid orange curve on pink background is the temperature forcing used for the second spin. The green curve is the temperature forcing in the second main run which is initialized from the last time step of the second spin run. (b) The orange curve represents the $\delta^{15}N$ modeled by the CFM during the second spin. The green curve is the $\delta^{15}N$ modeled during the second main run. The red curve represents $\delta^{15}N$ running in the same time interval as the second main run (green) but without second spin. The black solid line represents a long run without second spin as comparison to the other model runs.*

of this procedure is that it takes a while until the nitrogen isotopes diffuse through the firn column and realistic δ^{15}N values at lock-in depth are yielded. In order to overcome this problem the module `secondSpin.py` is implemented. `secondSpin.py` reads all parameters of the firn column that are necessary to initialize the firn column (depth, age, density, age, temperature and grain size) at ca. 5000 yr after the main run started. This period of time is called the "second spin". `secondSpin.py` further reads also the parameters that are initialized for the firn air (diffusivity, firn air advection rate, ice matrix velocity, gas age and values of ^{15}N) at ca. 5000 yr after the main run started. All these parameters are then saved in the `spin.hdf5` file.

Then, a second CFM run is started at the time the first CFM main run stopped. The code in the CFM is slightly altered to allow for the initialization of all firn air parameters from the `spin.hdf5`. For this purpose the key `"SecondSpin": true/false` is introduced in the `.json` configuration file. If `"SecondSpin": true`, all firn and firn air parameters are initialized using `spin.hdf5` created in the previous main run (see Figure 3.14).

Following this approach allows for realistic δ^{15}N values from the beginning of the second main run. Figure 3.13 shows CFM runs with (green curve in (b)) and without second spin run (red curve in (b)) in comparison in a time interval from $-43\,800$ yr to $-30\,000$ yr. While the green
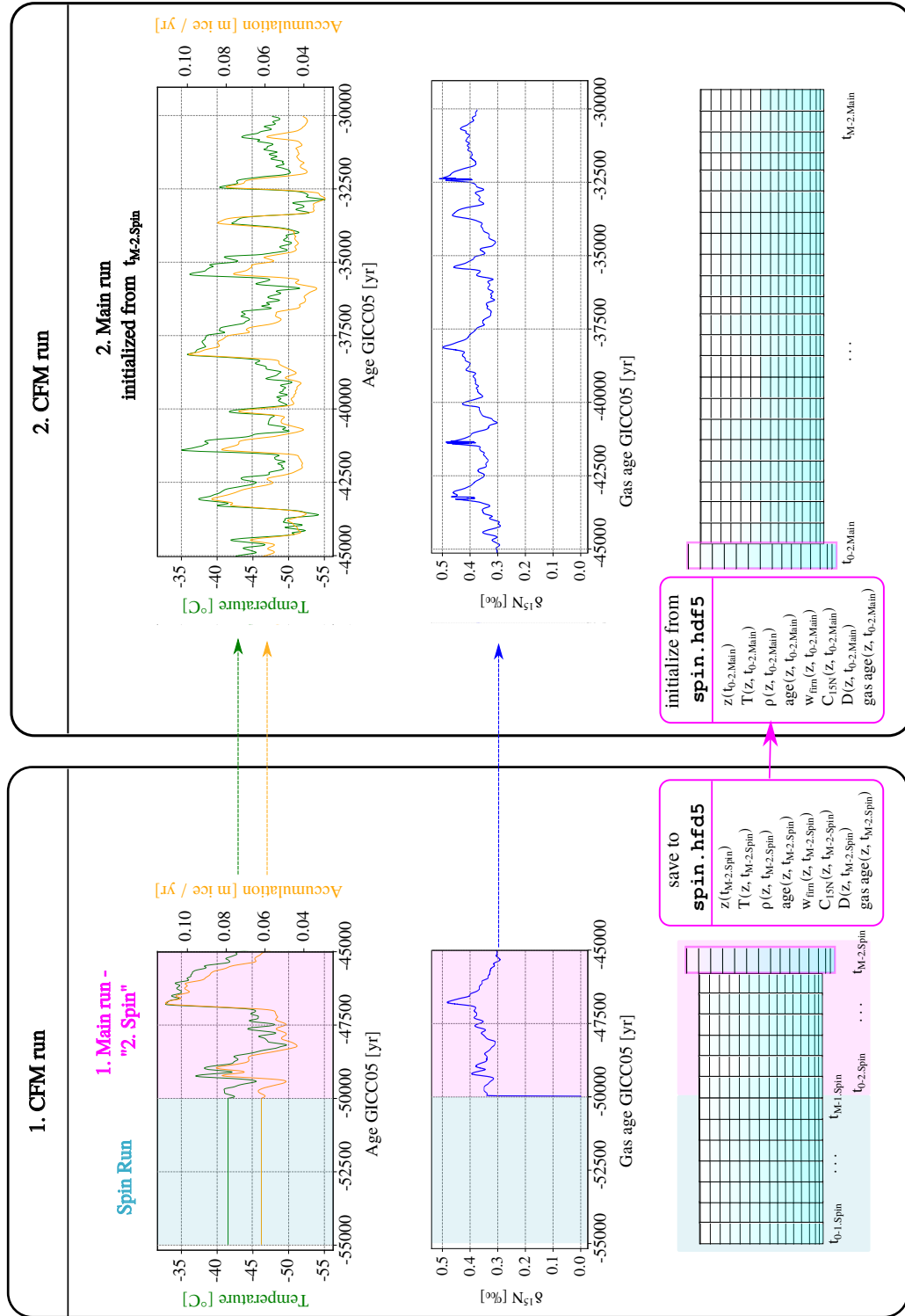
Figure 3.14: *Flow diagram for the CFM using a second spin.* *In order to prevent the model from producing unrealistic $\delta^{15}N$ values in the beginning of the main run, a second spin run is introduced which basically saves the parameters needed to initialize the firn (air) column at time step $t_{M\text{-}2.Spin}$. In a second run of the CFM the firn (air) column is initialized using these saved parameters.*

δ^{15}N curve is initialized from the second spin run (orange curve) the red curve is initialized from a normal spin run with constant temperature forcing (not depicted). It is visible that it takes around 2000 yr until the green and red curve meet. Furthermore one can clearly see the time interval in the beginning where the "firn air column" starts building up, both for the orange and the red curve. The black line is a comparison of firn (air) column that has already been built up for 6000 yr before the other two firn columns are initialized and build up. After the build up all three curves show similar δ^{15}N distributions. However, there are some intervals with a clear difference of up to 0.04 ‰ which is remarkable since all model runs are forced with the same surface temperatures just with a different starting time.

3.3 Minimizers

Paleo surface temperatures are reconstructed from δ^{15}N values by inverting the CFM with two commonly used/standard minimizers from the `scipy.optimize` library. The minimizers used are the `minimize` and the `least_squares` functions [54]. The optimizing method used for `minimize` is Nelder-Mead [56]. The input parameters for both parameters are the function f to be minimized and an initial guess of variables $\theta_0 = [\alpha_0, \beta_0]$. The general idea of the minimizer is to create a function f that calculates a surface temperature history from δ^{18}O data exploiting the linear relation between δ^{18}O and temperature. The resulting temperature history is then passed to the CFM which models firn densification, heat diffusion and gas diffusion processes, and returns δ^{15}N at lock-in depth. Depending on the minimizer used f subsequently returns either a self-defined cost function that calculates the mean squared error (MSE) between modeled δ^{15}N and δ^{15}N data (scalar output) or the absolute value of the difference between modeled δ^{15}N and δ^{15}N data (non-scalar output). Two modules `inversion_minimize_linear_SecondSpin.py` and `inversion_leastSquares_linear_SecondSpin.py` are implemented in order to reconstruct paleo surface temperatures using `minimize` and `least_squares`. As mentioned in Sections 3.2.2 and 3.2.4, the CFM only allows for gas diffusion calculations in the main run. In order to ensure a well-defined starting condition for the firn column (and firn air) a second spin run is needed. Consequently, the modules are structured such that two optimizations are performed successively: one for the first run of the CFM including first and second spin run, and one for the second CFM run, hereinafter called "Second Main" run. The first optimization minimizes f_{Spin} in a time interval of ca. 7000 yr before the desired time interval to be modeled in the second main run. The second optimization minimizes f_{Main} in the desired time interval. This procedure provides an already good first temperature guess for the second main run. Furthermore, it reduces the influence of the so-called "memory effect" which is the influence of earlier firn states on later firn states caused by temperature and accumulation rates at earlier time stages [24]. In the following, it will be explained in more detail how f_{Spin} and f_{Main} are structured and implemented (see also Figures 3.15 and 3.16).

In general, f_{Spin} and f_{Main} are structured quite similarly. The first guess for α and β is used to calculate the temperature forcing according to:

$$T = 1/\alpha \cdot \delta^{18}\text{O}_{\text{smooth}} + \beta. \tag{3.10}$$

The temperature is then saved as `input_T.csv` input file and passed to the CFM together with the accumulation rate forcing file `input_Acc.csv` which stays the same throughout the whole first optimization step. For each iteration the CFM runs with activated spin run. The CFM usually returns a spin up file `spin_SecondSpin.hdf5` and a results file `results_SecondSpin.hdf5`. In some cases, no output files are created because the CFM crashes which happens when the close-off depth is below the actual end of the modeled firn column. This can happen even though a big initial firn depth is set (550m) because the firn boxes can become very thin during time intervals with low surface temperatures accompanied by low snow accumulation rates. If no output files are created, no modeled δ^{15}N values exist and consequently no cost function is calculated which leads to an abortion of the minimizer. In order to overcome this problem a condition is added which checks whether a results file exists. If no results file exists the cost function is set directly to a high value (e.g. 100, but sometimes the value had to be adjusted to even higher values). In the case of a successful CFM run modeled δ^{15}N values at lock-in depth, ice age, gas age and Δage are read or calculated from the results file with `get_d15N_model()`. Since the number of available δ^{15}N model points is significantly higher than available data points (2 yr time resolution vs. a mean distance between data points of 60 yr), the modeled δ^{15}N signal is interpolated to available ice age time steps from the data set using `interpolate_model_to_data()`. In a next step the cost function is calculated. For `minimize` the cost function has to be a scalar value [54] and it is chosen as the MSE scaled with the uncertainty $\sigma_{\delta^{15}\mathrm{N}}$ of δ^{15}N data (see Table 3.1):

$$\widetilde{MSE} = \frac{1}{N} \cdot \frac{\sum_{i=0}^{N}(\delta^{15}\mathrm{N}_{\mathrm{data},i} - \delta^{15}\mathrm{N}_{\mathrm{model},\,i})^2}{\sigma^2_{\delta^{15}\mathrm{N},i}}, \tag{3.11}$$

with N the number of available data points in the selected ice age interval.

For `least_squares` the cost function is simply defined as the absolute value of the difference between modeled δ^{15}N and δ^{15}N data (residuals) and is non-scalar. The method `least_squares` then internally calculates a loss function from these residuals. `least_squares` has several options to calculate the loss function, and it is chosen to `"linear"`, which calculates the loss according to a standard least square problem [54]. The cost function is calculated using only δ^{15}N values in the second half of the time interval to prevent the minimizer from fitting δ^{15}N in a time interval where no reasonable firn column is developed yet.

For each iteration step the parameters α and β are altered as described in Section 2.4. Furthermore, all important parameters (α, β, modeled gas age, modeled ice age, modeled δ^{15}N and δ^{15}N data) are saved in a dictionary. If one of the termination criteria (maximum number of iterations reaches, tolerance by the change of the cost function, tolerance by the change of independent variables α and β, or the tolerance by the norm of the gradient is reached [54]) is fulfilled the iteration stops and the dictionary is saved as `.h5` file.

Next to the parameters saved in the `.h5` file, the `spin_SecondSpin.hdf5` file is rewritten as described in Section 3.2.4 to allow the firn (air) column to be initialized from the firn column of the last time step of the second spin run.

Then the second optimization step starts in the desired time interval starting at the last time step of the second spin run. A new accumulation file is saved for the new time interval and the corresponding δ^{18}O data is selected and smoothed. The first guess for the parameters α and

β are the optimum parameters $\alpha_{\text{opt, 2.Spin}}$ and $\beta_{\text{opt, 2.Spin}}$ determined by the minimizer in the first optimization step. Then, the CFM is started using the new temperature and accumulation input files and with `"SecondSpin": true` specified in the `.json` file, which makes the CFM initialize the firn column from the new spin file. Since no spin run is performed during the second optimization step f_{Main} is implemented in a slightly different way than f_{Spin}. The firn column initialized in the second main run corresponds to the temperature history in the last time step of the second spin. However, the minimizer changes the temperature curves with varying parameters α and β which means that there is a rapid jump in the temperature signal right after the initialization. Such a sudden jump in temperature would also cause a sharp change in the firn parameters and as such contribute to the memory effect. To reduce this effect a linear temperature ramp is inserted in the first $1000\,\text{yr}$ of the main run connecting the temperature at initialization with the temperature guess of the respective iteration step. That way, the firn column is slowly adjusted to the change in climatic condition and thus the CFM is also less likely to deal with numerical instabilities which sometimes occur during rapid and big jumps in temperature.

The following steps are the same as for f_{Spin}. The cost function is calculated from ca. $1000\,\text{yr}$ after the end of the linear temperature forcing. As for f_{Spin} all necessary parameters are saved in a dictionary for each iteration step and saved as `.h5` when the minimizer stops.
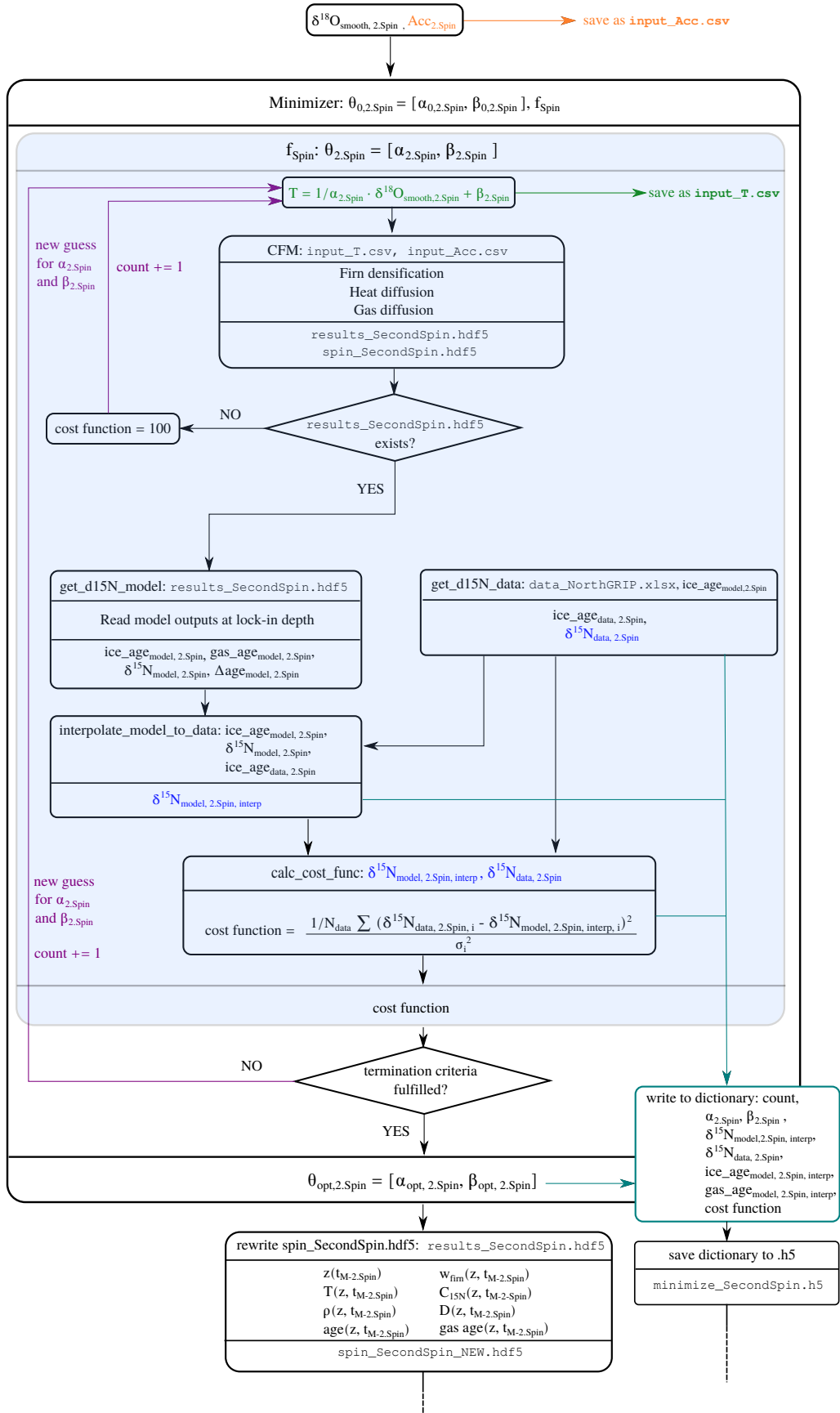
Figure 3.15: *Computation flow diagram for the inversion of the CFM using a common SciPy minimizer.* *To be continued in Figure 3.16.*
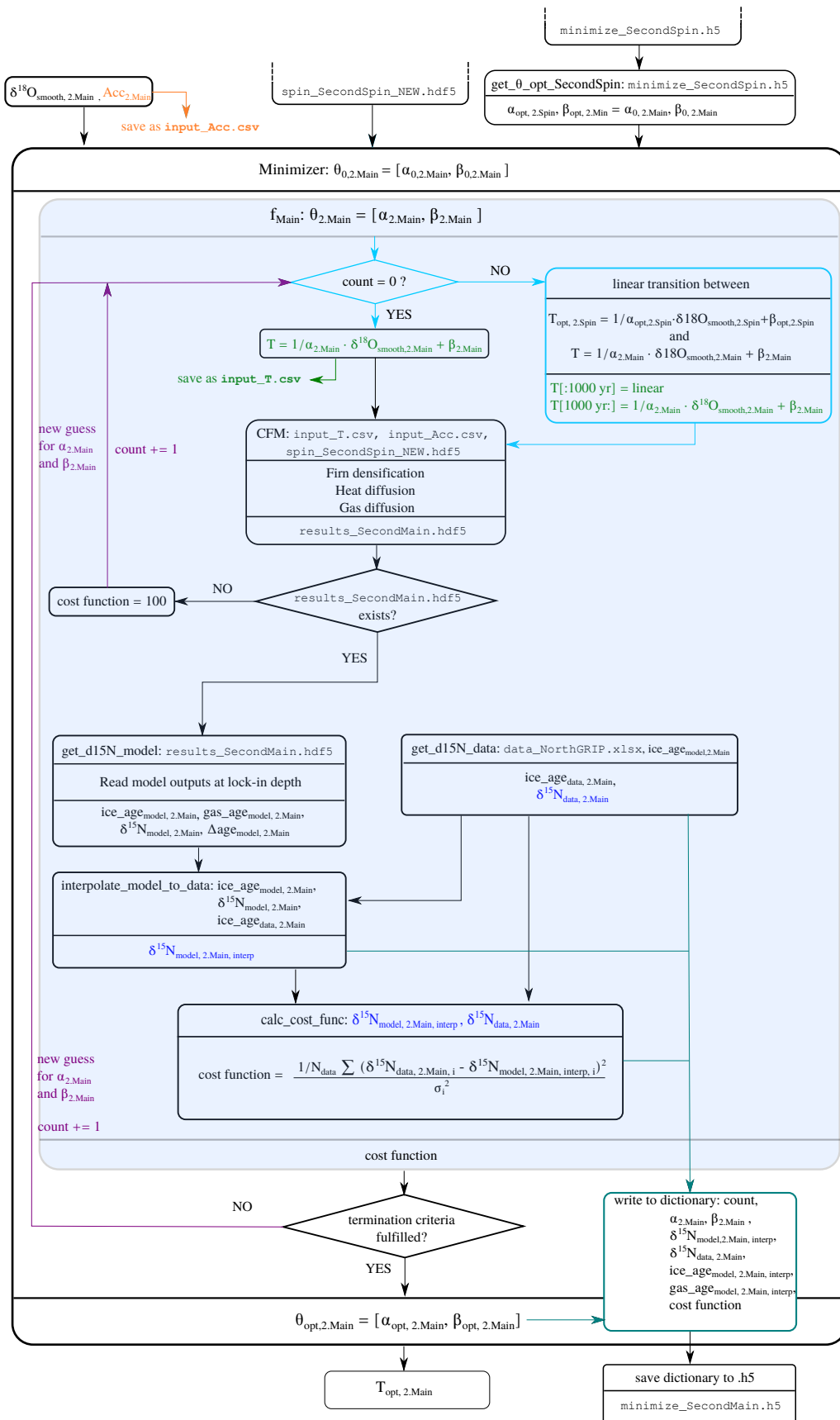
Figure 3.16: *Continuation of computation flow diagram in Figure 3.15.*

3.4 Experiments

The aim of this project is to obtain surface temperature histories at North GRIP from stable nitrogen isotopes by using different firn densification and gas diffusion models from the CFM and commonly used built-in minimizers provided by Python. Furthermore, it should be evaluated how small or large differences in surface temperature histories are depending on the choice of model and minimizer.

In order to assess this, several experiments are conducted which will be presented in the following.

3.4.1 Experiment 1: Comparison of Firn Densification and Gas Diffusion Models using Kindler's Surface Temperature History

As a first approach, the CFM is forced with surface temperature and snow accumulation rate histories for North GRIP during the Last Glacial (10 - 122 kyr b2k) reconstructed by [1] (see Section 3.1). Thereby, a set of four different firn densification models and four different gas diffusion models is used. The four densification models are Barnola, Herron and Langway, Herron and Langway with Sigfus Johnsen formulation, and Goujon. The first three firn air diffusion models are based on the firn air diffusion module of the CFM and either calculate the firn air advection according to [48] (referred to as "Christo" in the CFM) and [49] (referred to as "Darcy" in the CFM) or neglect firn air advection (referred to "zero" in the CFM). In the fourth gas diffusion model, the firn air diffusion module is not used and stable nitrogen isotope ratios are calculated according to Equations (2.30) and (2.31).

In order to compare the models with each other and to compare the models with previous studies ([1], [24]) the mean mismatch D_{mean} is calculated as in [24]:

$$D_{\mathrm{mean}} = \frac{1}{N} \sum_{i=0}^{N} \left| \delta^{15}\mathrm{N}_{\mathrm{data},i} - \delta^{15}\mathrm{N}_{\mathrm{model},i} \right|, \tag{3.12}$$

with N the number of available measured $\delta^{15}\mathrm{N}$ data points within the optimization time interval.

3.4.2 Experiment 2: Automated Firn Model Inversion Using Two Minimizers and Different Firn Densification and Gas Diffusion Models

For this experiment, the CFM is run with snow accumulation rates from [1] and surface temperatures reconstructed from smoothed $\delta^{18}\mathrm{O}_{\mathrm{ice}}$ as input (compare Equation 3.10). Different combinations out of four firn densification models and four gas diffusion models are used. The optimum parameters for α and β to fit modeled $\delta^{15}\mathrm{N}$ to measured $\delta^{15}\mathrm{N}$ are determined by inverting the CFM using the Nelder-Mead algorithm or the least squares algorithm (presented in Sections 2.4 and 3.3). In total, 32 inversion runs are performed for the full dataset provided by [1] according to the procedure described in Section 3.3. For these inversions, it is not accounted for the fact that α changes with time. This means, the optimization is performed

over the full data set without windowing resulting in a single set of α and β.

One aim of this experiment is to evaluate the performance of the two minimizers with respect to their suitability for the reconstruction of ancient surface temperatures from stable nitrogen isotope ratios. The evaluation of the minimizers is based on how well the modeled δ^{15}N values fit the measured δ^{15}N and how fast the algorithms converge. For this purpose, D_{mean}, $\widetilde{MSE}$ and the Pearson correlation coefficient r are calculated. r is determined using `scipy.stats.pearsonr` [81]. Furthermore, for each inversion the number of function calls as well as improvements (referred to as a decrease of the cost function ($\widetilde{MSE}$)) are documented. The second aim of this experiment is to assess how the choice of different firn densification models and different gas diffusion models influences the difference in reconstructed surface temperature histories.

All optimization runs are started with the same initial guess $\alpha_0 = 0.37\,\text{\textperthousand}\,\mathrm{K}^{-1}$ and $\beta_0 = 73\,\mathrm{K}$ and performed in the time interval 10 - 122 kyr b2k.

3.4.3 Experiment 3: Randomized Firn Model Inversion

This experiment is performed similarly to experiment 2. The optimization is run by randomly selecting a firn densification model out of BAR, HLD, HLS and GOU and a gas diffusion model out of Christo, Darcy, zero and FA-off for each iteration step of the optimization in order to test the temperature sensitivity to a randomly selected firn model and to investigate whether the least squares algorithm can deal with a variable function f to be minimized.

Chapter 4

Results and Discussion

4.1 Experiment 1: Comparison of Firn Densification and Gas Diffusion Models using Kindler's Surface Temperature History

In order to investigate the performance of different firn densification and gas diffusion models, various models are forced with the same input surface temperature histories reconstructed by [1]. The modeled δ^{15}N values are depicted in Figures 4.1 and 4.2.

Figure 4.1 shows modeled (coloured curves) and measured (black line with dots) δ^{15}N on gas age scale for the Barnola (BAR, blue), Herron and Langway (HLD, orange), Herron and Langway with Sigfus Johnsen formulation (HLS, pink) and Goujon (GOU, green) firn densification models with activated firn air diffusion module using firn air advection according to Buizert [48] ("Christo").

BAR shows a very similar trend to HLD and HLS which can be explained by the fact that all three of the models use the Herron and Langway formulation at least for the first densification zone. The three models show differences especially for rapid and large changes in surface temperature during DO events. Here, some numerical instabilities seem to occur for HLD and HLS. Furthermore, HLD reacts very slow to a (gradual) decrease in temperature after a rapid increase which was also noted by [25] who state that the HLD model is less suitable for transient climates with rapid changes in the climatic condition.

As seen from Figure 2.2 firn parameters such as the lock-in depth highly vary with the choice of the firn densification model which results in a variation in stable nitrogen ratios at lock-in depth which is also observed in this experiment.

The mean mismatches between measured and modeled δ^{15}N in this study are in general higher than the mean mismatches between measured and modeled δ^{15}N by [1] and [82] (compare Table 4.1) who used a firn densification model following the Barnola formulation [83], [34]. In fact, the Barnola model fits the measured δ^{15}N data best using the reconstructed temperature history from [1]. Differences between this study and [1] and [24] may stem from the used firn air diffusion model accompanied with a different parameterization of the thermal diffusivity and/or usage of a different e.g. firn conductivity parameterization. [24] calculated stable nitrogen isotope ratios from Equations (2.30) and (2.31) while the results presented here are

obtained using the firn air diffusion model which solves the firn air transport equation (compare Equation (2.36)).

	Kindler et al. 2014	Döring 2020	BAR	HLD	HLS	GOU
D_{mean} [permeg]	18	20	28	43	38	44

Table 4.1: *Comparison of the mean mismatch D_{mean} according to Equation (3.12) of the four different firn densification models (BAR, HLD, HLS and GOU) with previous studies of Kindler et al. (2014) [1] and Döring (2020) [24].*

Figure 4.2 shows again modeled and measured $\delta^{15}N$ and the surface temperature reconstructed by [1] which is used to force the CFM. For this experiment the CFM is run with firn densification according to Barnola [34] and different firn air diffusion models. "Christo", "Darcy" and "zero" refer to an enabled firn air diffusion module with firn air advection calculated according to [48] and Darcy [49] or firn air advection set to zero. "FA off" refers to a model run without activated firn air module. In this case $\delta^{15}N$ is calculated according to Equations (2.30) and (2.31).

It is notable that the modeled $\delta^{15}N$ agree better with measured $\delta^{15}N$ than in the previous experiment, which is also clear from the mean mismatch D_{mean} (compare Table 4.2). The best agreement is achieved with the last model run ($D_{mean} = 25$ permeg) which does not use the firn air diffusion module. This is probably because stable nitrogen isotope ratios are calculated using the closest approach to [1] to model $\delta^{15}N$. For the last model run the firn air diffusion module is not used and thermal and gravitational fractionation are calculated as described previously. Furthermore, as described in Section 2.2 also the parameterizations of the thermal diffusion sensitivity slightly differ for the two approaches for calculating stable nitrogen isotope fractionation which could be an additional reason for differences in modeled $\delta^{15}N$.

Even though the firn air transport equation is solved including the advection term, advection

	Kindler et al. 2014	Döring 2020	Christo	Darcy	zero	FA off
D_{mean} [permeg]	18	20	28	28	28	25

Table 4.2: *Comparison of the mean mismatch D_{mean} according to Equation (3.12) of the four different firn air diffusion models (Christo, Darcy, zero, FA off) with previous studies of Kindler et al. (2014) [1] and Döring (2020) [24].*

almost does not have an influence on the $\delta^{15}N$ values at lock-in depth. Modeled $\delta^{15}N$ using the firn air diffusion module provided by the CFM are very similar for all three configurations even though calculated firn advection velocities are quite different from each other and in the
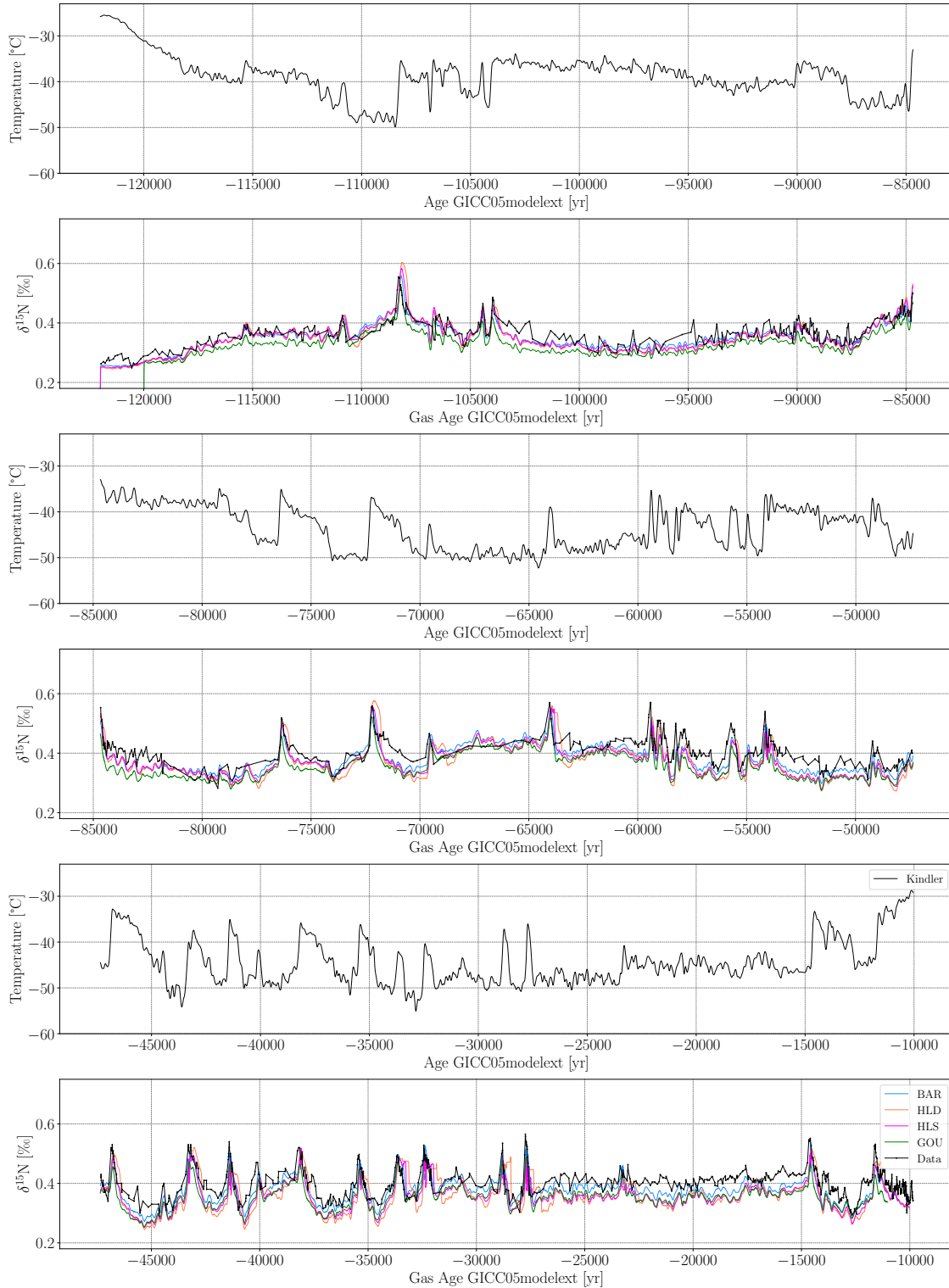
Figure 4.1: $\delta^{15}N$ modeled with the CFM using surface temperatures reconstructed by [1] as input and four different densification models (Barnola (BAR), Herron and Langway (HLD), Herron and Langway using Sigfus Johnsen formulation (HLS) and Goujon (GOU)). $\delta^{15}N$ are calculated with activated firn air module and Buizert's formulation for firn air advection.

51

order of magnitude of the velocity of the ice matrix. While for Christo's advection model the firn air advection increases with depth until the lock-in depth, an opposite effect is observed for the implemented Darcy model where firn air advection gradually decreases with depth and follows basically the ice matrix (compare Figure 4.2). The advection rate according to Christo becomes more apparent in warmer climates (compare Figure 4.3(a) with (b)). However, w_{air} ceases quickly within the upper 20 m of the firn column and then the firn air follows the velocity of the ice matrix.
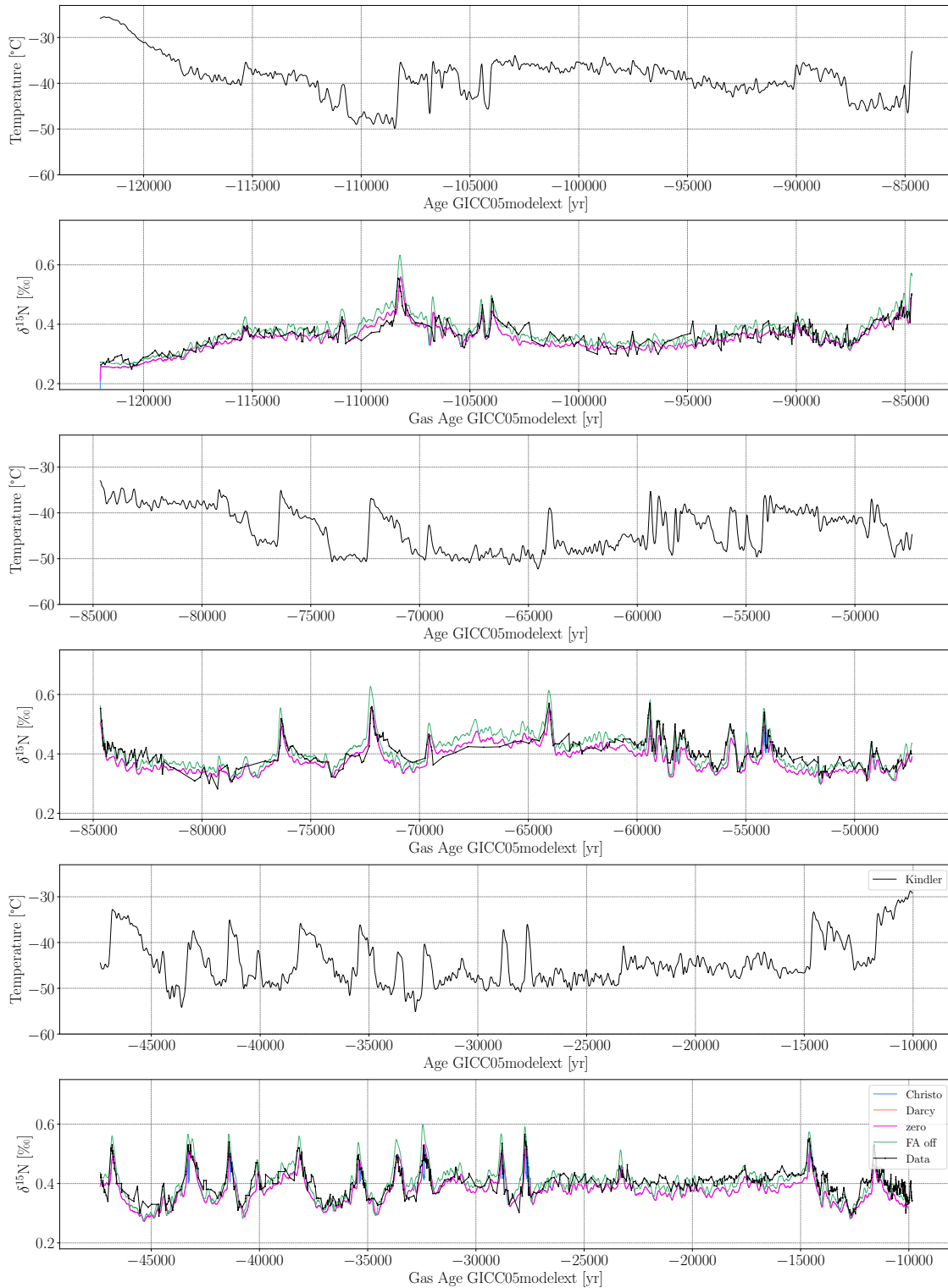
Figure 4.2: $\delta^{15}N$ modeled with the CFM using surface temperatures reconstructed by [1] as input, the Barnola firn densification model and four different gas diffusion models ("Christo"/"Darcy"/"zero": firn air diffusion module enabled with firn air advection according to Christo Buizert/ firn air advection according to Darcy/ no firn air advection; "FA off": firn air diffusion module disabled).
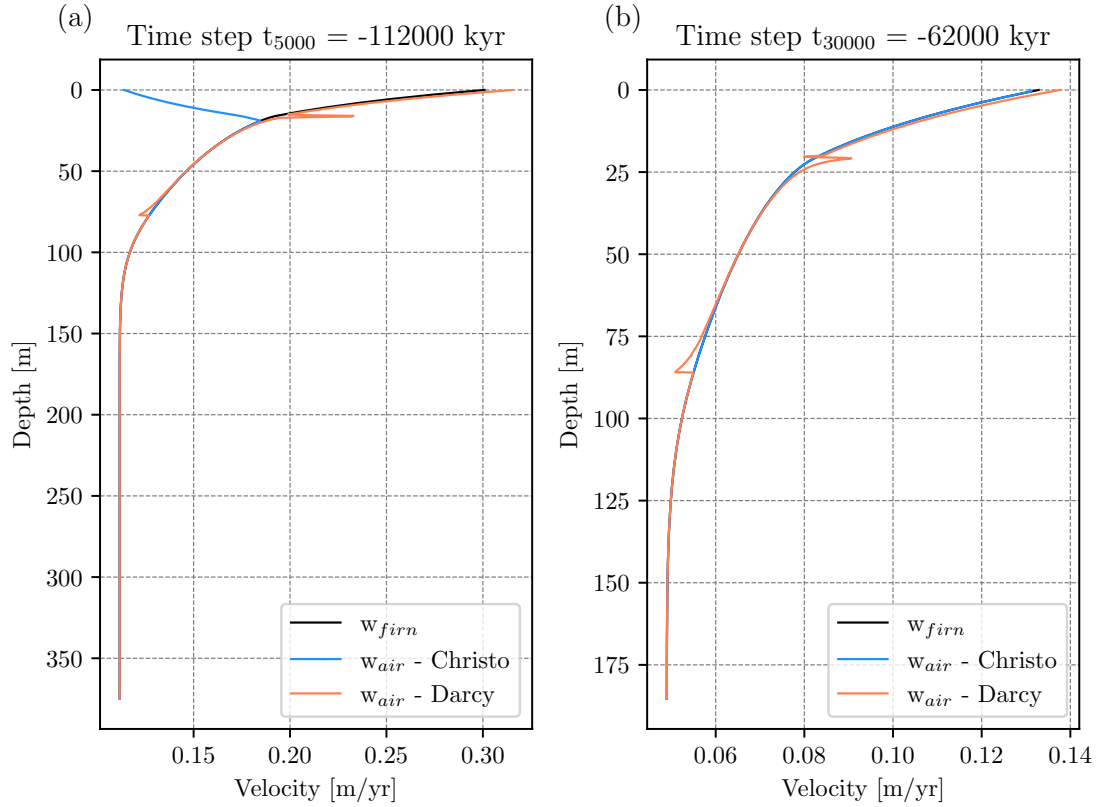
Figure 4.3: *Firn air advection rates for Darcy's and Christo's model for different time steps.* *Firn air advection rates and the downward velocity of the ice matrix (w_{firn}) are plotted against the depth of the firn column at time steps (a) $-112\,000$ yr and (b) $-62\,000$ yr. The excursions visible for Darcy's model (orange curve) at around 15 m depth stem from an almost Zero division occurring when the change in air pressure within the firn column due to the change in open porosity is calculated in the CFM.*

4.2 Experiment 2: Automated Firn Model Inversion Using Two Minimizers and Different Firn Densification and Gas Diffusion Models

This experiment is performed in order to investigate how well the two selected minimizers perform for the inversion of the CFM. In total 32 inversions are performed using a combination out of four different firn densification models (BAR, HLD, HLS, GOU), four different gas diffusion models (Christo, Darcy, zero, FA-off) and two minimizers (Nelder-Mead algorithm (NM), least squares (LS)).

The inversion is performed over a time interval between $-120\,000\,\mathrm{yr}$ and $-10\,000\,\mathrm{yr}$ using the inversion approach including the second spin as described in Section 2.4 and a single set of parameters α and β over the whole time interval for the second main run.

Tables 4.3 and 4.4 show the optimum parameters α and β found in the minimization time interval for the second spin and second main run, respectively. Furthermore, the tables indicate the cost functions calculated for the last iteration step, the mean mismatch for the first guess and the last iteration step, the number of calls of f_{Spin} and f_{Main} and the number of improvements (with respect to the cost function).

Figures 4.4 and 4.5 show reconstructed surface temperatures and $\delta^{15}\mathrm{N}$ at lock-in depth on gas age scale using the four different firn densification models and Christo's firn air diffusion model for a minimization performed with the Nelder-Mead algorithm and the least squares algorithm, respectively. Figures 4.6 and 4.7 show again reconstructed surface temperatures and $\delta^{15}\mathrm{N}$ for model runs performed using Barnola's firn densification model and four different gas diffusion models using the Nelder-Mead algorithm and the least squares algorithm, respectively. All corresponding Δages and $\delta^{15}\mathrm{N}$ on ice age scale are depicted in Figures C.1-C.4. In general, the modeled $\delta^{15}\mathrm{N}$ fits measured $\delta^{15}\mathrm{N}$ well during the second spin run (between $-122\,000\,\mathrm{yr}$ and $-113\,000\,\mathrm{yr}$) for all configurations with cost function values between 3.29 and $8.52\,\text{\textperthousand}^2$ in a time interval of $9000\,\mathrm{yr}$. However, α and β thereby vary widely for different minimizers but same firn densification and gas diffusion model configuration. For most of the cases, the least squares algorithm seems to find the better solution compared to the Nelder-Mead algorithm which can be seen from mostly lower cost function values (by a factor of up to 2.4) and mostly lower mean mismatch values. For all inversions the mean mismatch value is significantly decreased compared with the mean mismatch corresponding to the initial guess (from $D_{\mathrm{mean},0}$ between 94.72 and 196.83 permeg to D_{mean} between 9.81 and 44.14 permeg).

For the second main run, cost function and mean mismatch values are significantly higher than for the second spin run. Furthermore, both minimizers find different but sometimes similarly well performing optimum solutions for α and β. When comparing cost functions and mean mismatches of the Nelder-Mead algorithm and the least squares algorithm the least squares algorithm performs even slightly worse. However, the least squares algorithm clearly outperforms Nelder-Mead in terms of the number of function calls which results in a lower overall run time of the inversion.

Another interesting results is that especially for the time intervals between $-80\,000\,\mathrm{yr}$ and $-58\,000\,\mathrm{yr}$, and between $-32\,000\,\mathrm{yr}$ and $-23\,000\,\mathrm{yr}$ the Nelder-Mead algorithm overestimates

δ^{15}N by up to $0.14\,\text{‰}$ for the densification models coupled to the Christo firn advection model which could be due to a more sparse data set within these intervals. Even though the modeled δ^{15}N overestimates measured δ^{15}N by a lot, the cost function or D_{mean} are not affected too much by these values. For future optimizations it could thus be very useful to include some weighing factors for sparse data intervals into the cost function to avoid a bad fit in time intervals with sparse data.

The second aim of this experiment was to compare temperature histories resulting from the optimization of a range of different firn models and evaluate the fits of modeled to measured δ^{15}N.

By looking at cost function and mean mismatch values determined for the second main run in Table 4.4 one can see that the best fits of δ^{15}N were obtained for the Barnola model, followed by Goujon, and then Herron and Langway with Sigfus formulation. The worst fits were obtained using the Herron and Langway model which can be explained with the fact that Herron and Langway reacts slowly to sudden climatic changes.

With respect to gas diffusion no clear trend is visible in terms of cost function and mean mismatch.

In general, a wide spread in δ^{15}N calculated with different models in a certain time interval results in a wide spread of reconstructed temperatures in this time interval (compare Figures 4.4 and 4.6 in the time intervals between $-80\,000\,\text{yr}$ and $-58\,000\,\text{yr}$, and between $-32\,000\,\text{yr}$ and $-23\,000\,\text{yr}$). This makes sense in particular in terms of gravitational fractionation which depends on the depth of the lock-in. As explained in Section 2.2, higher temperatures lead to a more shallow lock-in depth and consequently lower contribution of gravitational fractionation to the total isotope fractionation and vice versa. A difference between modeled δ^{15}N distributions for different firn models implies therefore that differences in the reconstructed temperature histories can not only be explained by the usage of different firn models. Instead, a major reason for the difference in this case is that the global minimum resulting in the best fit of δ^{15}N is not found by the respective minimizer. This means that the "correct" temperature is not found in the first place because δ^{15}N values are already not perfectly fitted.

For well-fitted time intervals reconstructed temperatures are very similar to the temperature history reconstructed by [1]. While BAR, HLD, HLS, and GOU are very similar in δ^{15}N and show the same temperature histories and temperatures reconstructed for BAR, HLD and HLS are very similar (compare Figure 4.5, red, orange and blue curve lie on top of each other), temperatures reconstructed for GOU are shifted to lower values by about $3.5\,\text{K}$. The most significant difference between temperatures reconstructed by [1] and reconstructed temperatures with different firn models of the CFM is observed for all investigated firn models in a time interval between $-50\,000\,\text{yr}$ and $-45\,000\,\text{yr}$ (DO 12) with a maximum difference of $8\,\text{K}$ for the Goujon model. Temperatures reconstructed by different models vary in a range of up to $5\,\text{K}$ in time intervals with low variability in δ^{15}N or sparse data.

Christo, Darcy and zero show almost the same δ^{15}N and temperature histories (compare Figure 4.7). δ^{15}N calculated according to Equations (2.30) and (2.31) are generally shifted toward slightly lower values by up to $0.03\,\text{‰}$ resulting in temperatures shifted to slightly higher values by up to $3\,\text{K}$ compared to BAR, HLD and HLS.

Peaks in measured $\delta^{15}N$ are mostly fitted well in terms of the timing by the model, especially for $\delta^{15}N$ optimized by the least square algorithm. Some small deviations may result from the fact that the gas age is set uniformly to $0\,yr$ at lock-in depth and uniformly to $15\,yr$ at close-off depth by the CFM. As a result, Δages calculated from gas age and ice age at lock-in depth are likely to not being highly accurate resulting in the gas age scale also not being completely accurate. Δages and $\delta^{15}N$ plotted on ice age scale are shown in Figures C.1, C.2, C.3 and C.4.

When comparing the $\delta^{15}N$ fits with [1] and [24] one can see that the mean misfits obtained from this study are clearly higher (in a range from $24.88\,permeg$ to $49.49\,permeg$, compare Tables 4.3 and 4.4) than mean misfits obtained from [1] ($18\,permeg$) and [24] ($20\,permeg$). Figure 4.8 depicts a scatterplot modeled versus measured $\delta^{15}N$ values for all 32 combinations of firn densification and gas diffusion models. Blue and red dots differentiate between modeled $\delta^{15}N$ using the Nelder-Mead or least squares algorithm, respectively. The Pearson correlation coefficient is indicated for each scatter plot and minimizer. Compared to the Pearson correlation coefficient obtained by [24] (r = 0.93) and [1] (r = 0.92), the correlation coefficients of this study are lower. However, when forming the Pearson correlation coefficient from the data in the time interval between $-38\,000\,yr$ and $-31\,000\,yr$ as also presented in [24], the correlation coefficient for the Barnola model rises up to r = 0.915 and up to r = 0.906 for Herron and Langway (compare D.1). The correlation coefficients for Herron and Langway with Sigfus formulation remain approximately the same. Modeled and measured $\delta^{15}N$ for Goujon show in general very low correlation.

In previous studies, α and β were determined for much smaller time intervals (ca. $2000\,yr$), because these parameters are different for different DO events. As a consequence, previous studies either selected single DO events to find the optimum parameters α and β, or introduced a small shifting time window in order to be able to fit a larger time interval [22], [21], [15], [24]. In this study, one large time window is used resulting in a single set of α and β. As a consequence, there are time intervals where the modeled $\delta^{15}N$ fit the data well and intervals where the fit is not very accurate which is also seen from the Pearson correlation coefficients calculated for the small time interval (Figure D.1). Furthermore, misfits calculated for this study are generally larger than for [1] and [24].

Previous studies also allowed for an additional degree of freedom by parameterizing not only temperature but also the snow accumulation rate as $A = c \cdot A_0$, with A_0 the given accumulation rate and c a constant to be determined by the minimizer.

Model run 2. SPIN	α [‰K^{-1}]	β [K]	Cost function $\widetilde{\text{MSE}}$ [‰^{2}]	$D_{\text{mean},0}$ [permeg]	D_{mean} [permeg]	No. calls	No. improve-ments
BAR-Christo-NM	0.354	67.593	4.86	107.48	11.48	116	19
BAR-Christo-LS	0.577	26.479	3.38	107.48	10.12	44	8
BAR-Darcy-NM	0.353	67.899	4.9	107.53	11.53	141	29
BAR-Darcy-LS	0.54	31.039	3.47	107.53	10.09	58	13
BAR-zero-NM	0.383	59.557	4.49	107.56	10.85	157	44
BAR-zero-LS	0.577	26.479	3.38	107.48	10.12	44	8
BAR-FA-off-NM	0.389	59.879	5.37	94.92	11.77	133	33
BAR-FA-off-LS	0.455	45.907	4.37	94.92	10.49	34	6
HLD-Christo-NM	0.353	68.247	7.61	124.68	13.98	131	26
HLD-Christo-LS	0.548	30.423	4.27	124.68	10.47	70	17
HLD-Darcy-NM	0.351	68.869	7.64	124.82	14.05	134	34
HLD-Darcy-LS	0.532	32.42	4.41	124.82	10.61	70	17
HLD-zero-NM	0.36	66.176	7.39	124.84	13.75	139	33
HLD-zero-LS	0.54	31.42	4.36	124.84	10.64	70	17
HLD-FA-off-NM	0.49	39.99	5.15	112.38	11.37	186	55
HLD-FA-off-LS	0.409	55.548	7.66	112.38	13.62	35	6
HLS-Christo-NM	0.445	46.254	4.1	124.1	10.41	152	42
HLS-Christo-LS	0.542	31.214	3.53	124.1	9.81	56	12
HLS-Darcy-NM	0.392	57.791	4.87	124.23	11.54	148	37
HLS-Darcy-LS	0.542	31.216	3.53	124.23	9.81	62	15
HLS-zero-NM	0.394	57.375	4.77	124.26	11.43	151	36
HLS-zero-LS	0.548	30.464	3.5	124.26	9.81	69	16
HLS-FA-off-NM	0.392	59.12	6.08	111.81	12.43	145	38
HLS-FA-off-LS	0.451	46.864	4.99	111.81	11.14	35	7
GOU-Christo-NM	0.34	70.948	8.19	177.71	14.67	98	15
GOU-Christo-LS	0.695	13.619	3.4	161.31	10.69	39	10
GOU-Darcy-NM	0.34	70.965	7.69	177.75	14.21	107	16
GOU-Darcy-LS	0.864	3.024	3.29	196.83	44.14	31	7
GOU-zero-NM	0.34	70.965	7.7	177.78	14.22	108	13
GOU-zero-LS	0.71	12.517	3.39	161.53	10.69	41	11
GOU-FA-off-NM	0.309	82.897	8.51	165.2	14.55	122	25
GOU-FA-off-LS	0.591	24.114	6.72	148.24	13.94	30	6

Table 4.3: *Comparison of performance of Least Squares and Nelder-Mead for model runs with different parameterizations - Second spin run.*

Model run MAIN	α [‰K^{-1}]	β [K]	Cost function $\widetilde{\mathrm{MSE}}$ [‰^{2}]	$D_{\mathrm{mean},0}$ [permeg]	D_{mean} [permeg]	No. calls	No. improve-ments
BAR-Christo-NM	0.359	68.979	20.03	54.62	34.02	90	14
BAR-Christo-LS	0.584	25.636	11.13	25.61	25.43	27	4
BAR-Darcy-NM	0.589	25.008	11.04	56.88	25.09	151	41
BAR-Darcy-LS	0.54	31.189	11.25	24.69	24.88	30	8
BAR-zero-NM	0.589	25.023	11.03	47.05	25.06	148	40
BAR-zero-LS	0.584	25.636	11.13	25.61	25.43	27	4
BAR-FA-off-NM	0.622	23.078	10.92	47.13	25.11	212	61
BAR-FA-off-LS	0.498	39.17	12.69	30.71	25.62	28	6
HLD-Christo-NM	0.37	65.472	30.12	57.5	41.09	104	11
HLD-Christo-LS	0.586	25.46	16.95	37.71	36.91	32	5
HLD-Darcy-NM	0.578	26.31	16.77	57.49	36.02	146	46
HLD-Darcy-LS	0.532	32.422	17.23	35.91	35.93	22	4
HLD-zero-NM	0.578	26.268	16.71	54.65	35.77	149	41
HLD-zero-LS	0.54	33.0	27.14	35.87	49.26	26	6
HLD-FA-off-NM	0.606	24.703	18.01	36.09	37.73	157	40
HLD-FA-off-LS	0.483	41.668	20.87	41.48	37.33	35	8
HLS-Christo-NM	0.495	37.947	12.97	30.01	28.8	176	36
HLS-Christo-LS	0.542	31.028	12.55	31.58	29.95	25	3
HLS-Darcy-NM	0.542	30.956	12.48	38.87	29.19	148	41
HLS-Darcy-LS	0.537	31.714	12.51	30.85	29.38	24	4
HLS-zero-NM	0.537	31.547	12.45	38.37	28.94	131	34
HLS-zero-LS	0.548	30.465	12.82	31.05	31.06	25	6
HLS-FA-off-NM	0.565	29.404	13.34	42.88	30.54	169	35
HLS-FA-off-LS	0.473	43.407	15.32	30.2	30.42	28	5
GOU-Christo-NM	0.347	71.931	30.35	64.44	41.54	97	14
GOU-Christo-LS	0.68	14.364	12.06	30.49	27.32	49	11
GOU-Darcy-NM	0.623	19.743	11.77	65.26	26.21	207	72
GOU-Darcy-LS	0.734	9.88	12.39	39.61	27.39	33	10
GOU-zero-NM	0.62	20.077	11.77	65.33	26.17	195	65
GOU-zero-LS	0.624	19.624	11.76	31.02	26.13	49	13
GOU-FA-off-NM	0.321	83.274	46.73	92.12	49.49	107	17
GOU-FA-off-LS	0.651	19.541	14.2	25.09	32.3	45	11

**Table 4.4:** *Comparison of performance of Least Squares and Nelder-Mead for model runs with different parameterizations - Main run.*
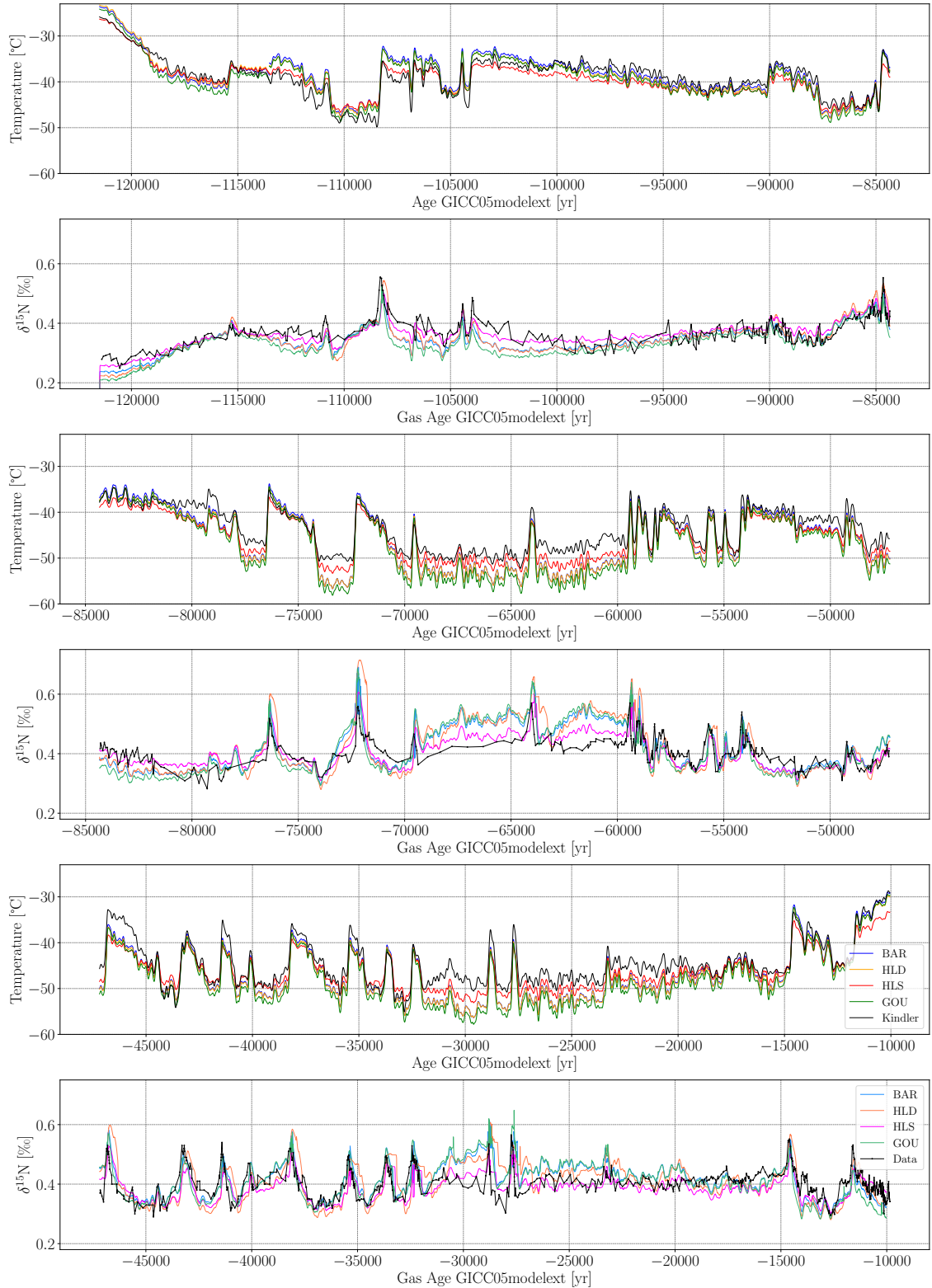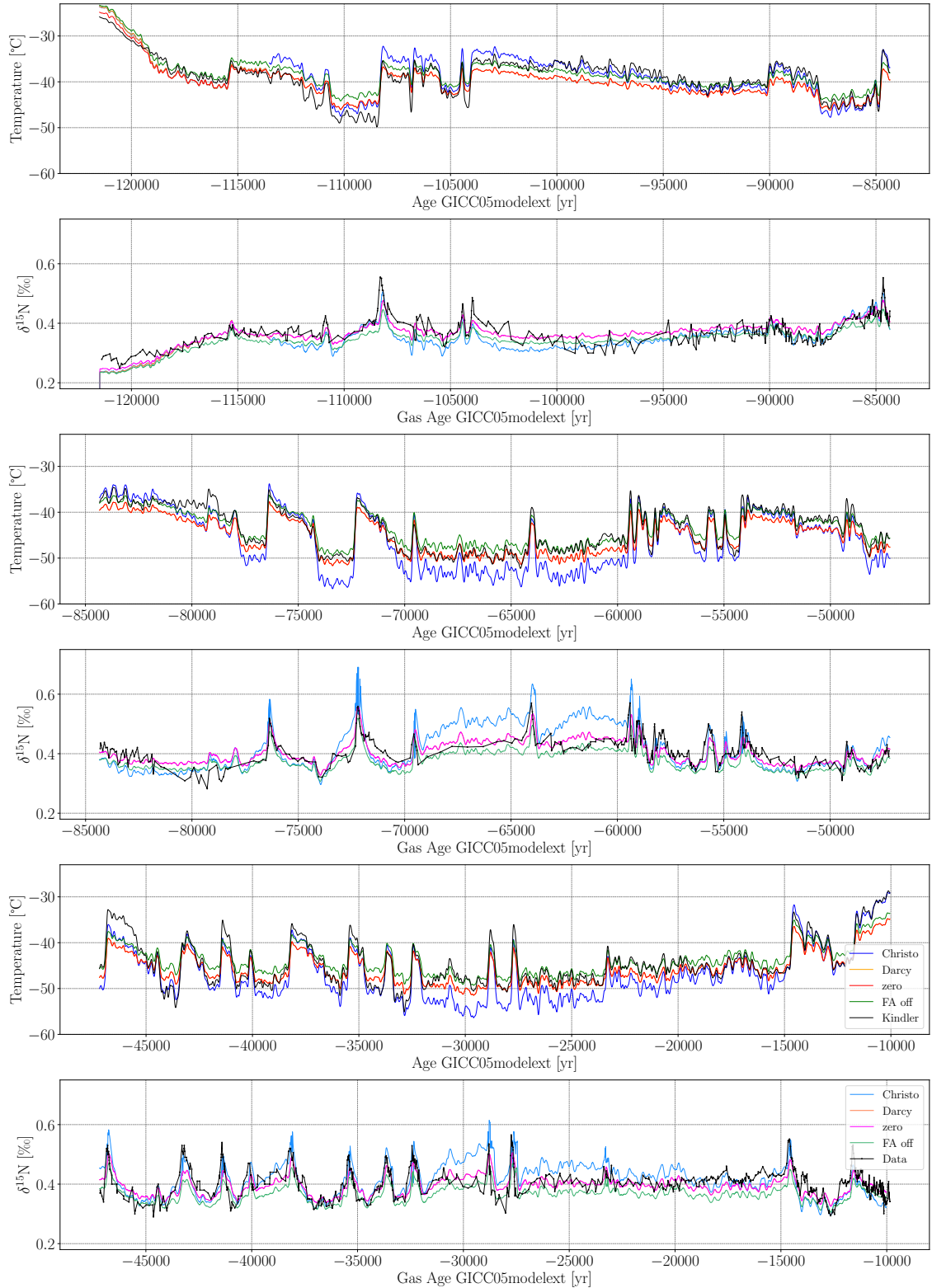
Figure 4.4: *Reconstructed surface temperatures for different densification models (Barnola (BAR), Herron and Langway (HLD), Herron and Langway with Sigfus formulation (HLS), Goujon (GOU)) using the Nelder-Mead algorithm and corresponding $\delta^{15}N$.*
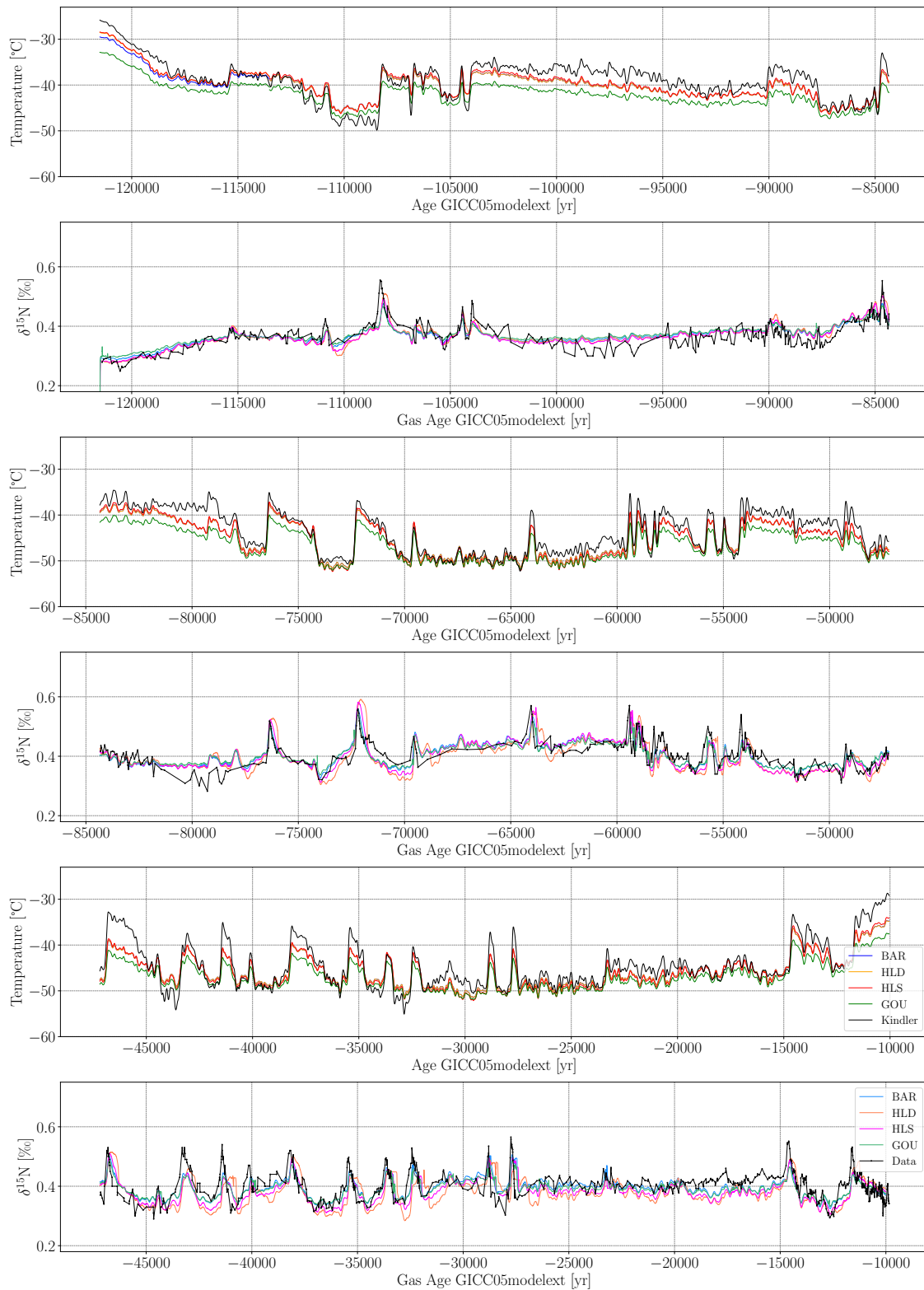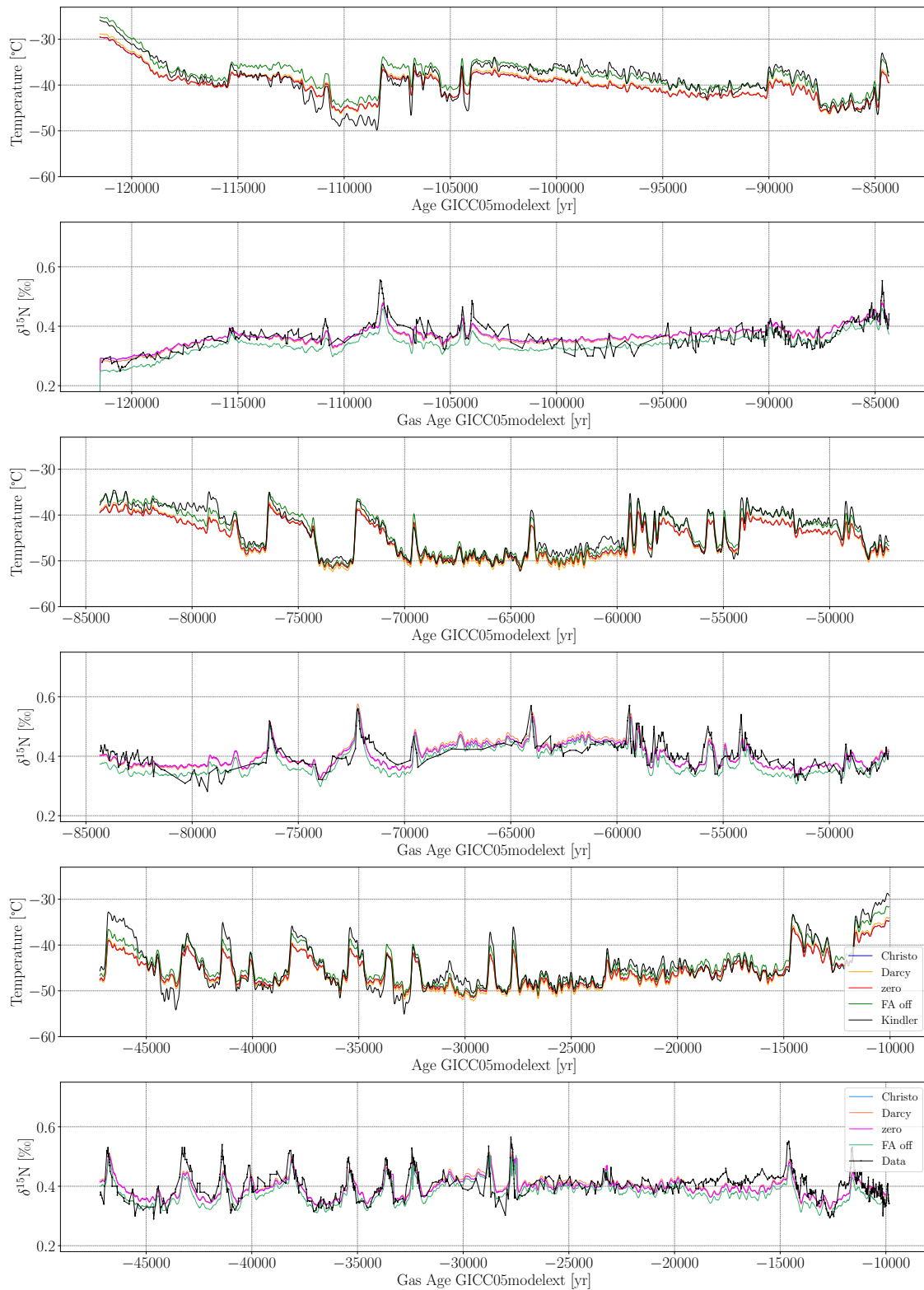
Figure 4.5: *Reconstructed surface temperatures for different densification models (Barnola (BAR), Herron and Langway (HLD), Herron and Langway with Sigfus formulation (HLS), Goujon (GOU)) using the least squares algorithm and corresponding $\delta^{15}N$.*

Figure 4.6: *Reconstructed surface temperatures for different gas diffusion models ("Christo"/"Darcy"/"zero": firn air diffusion module enabled with firn air advection according to Christo Buizert/ firn air advection according to Darcy/ no firn air advection; "FA off": firn air diffusion module disabled) using the Nelder-Mead algorithm and corresponding $\delta^{15}N$.*

Figure 4.7: *Reconstructed surface temperatures for different gas diffusion models ("Christo"/"Darcy"/"zero": firn air diffusion module enabled with firn air advection according to Christo Buizert/ firn air advection according to Darcy/ no firn air advection; "FA off": firn air diffusion module disabled) using the least squares algorithm and corresponding $\delta^{15}N$.*
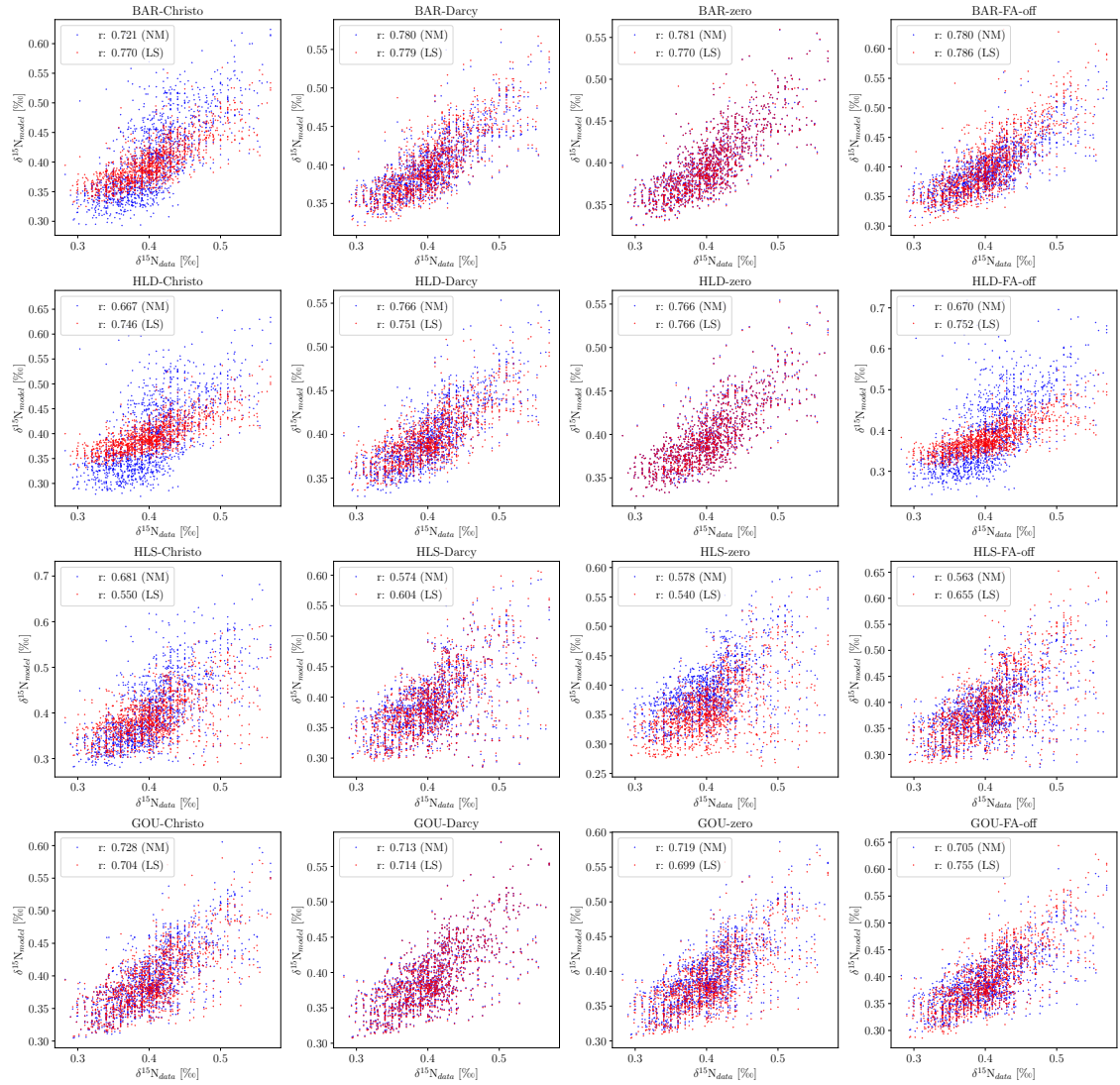
Figure 4.8: *Scatterplot of measured and modeled $\delta^{15}N$ for different combinations of firn densification and gas diffusion models.* *The best fit of modeled $\delta^{15}N$ is obtained by using either a least squares (LS) or Nelder-Mead (NM) algorithm.*

4.3 Experiment 3: Randomized Firn Model Inversion

This experiment is performed in order to test whether the data set can be fit using all firn models in various combinations at the same time by randomly selecting a firn model out of four and a gas diffusion model out of four for each iteration step of the optimization. For the optimization the least square algorithm is used. Figure 4.9 shows the modeled δ^{15}N on gas age scale in comparison to the measured δ^{15}N and reconstructed temperature in comparison to the temperature reconstructed by [1]. Overall, the modeled δ^{15}N agree well with measured δ^{15}N in time intervals where many measured data points are available. For time intervals with sparse data available from measurements the fit performs worse. As a consequence, reconstructed temperatures vary between $0\,$K and $3\,$K from temperatures reconstructed by [1] for time intervals with good agreement between modeled and measured δ^{15}N and between $2\,$K and $4.5\,$K for time intervals with bad agreement.

The parameters α and β, the cost function and mean mismatch of first guess and final iteration are indicated in Table 4.5. The Pearson correlation coefficient was calculated to $r = 0.730$, in the time interval between $-32\,000\,$yr and $-39\,000\,$yr the Pearson correlation coefficient rises to $r = 0.882$. In general, the cost function is slightly higher than cost functions for optimization runs performed in experiment 2. The mean mismatch is in a similar range.

Compared to previous optimization from experiment 2, very similar results could be obtained with similar mismatches. The least squares algorithm was able to find a solution from a variable function f to be minimized.

Model run MAIN	α [‰K^{-1}]	β [K]	Cost function [‰^{2}]	$D_{\mathrm{mean,0}}$ [permeg]	D_{mean} [permeg]
Random-LS	0.382	62.648	19.52	50.82	32.17

Table 4.5: *Performance of optimization run with randomly selected firn models.*
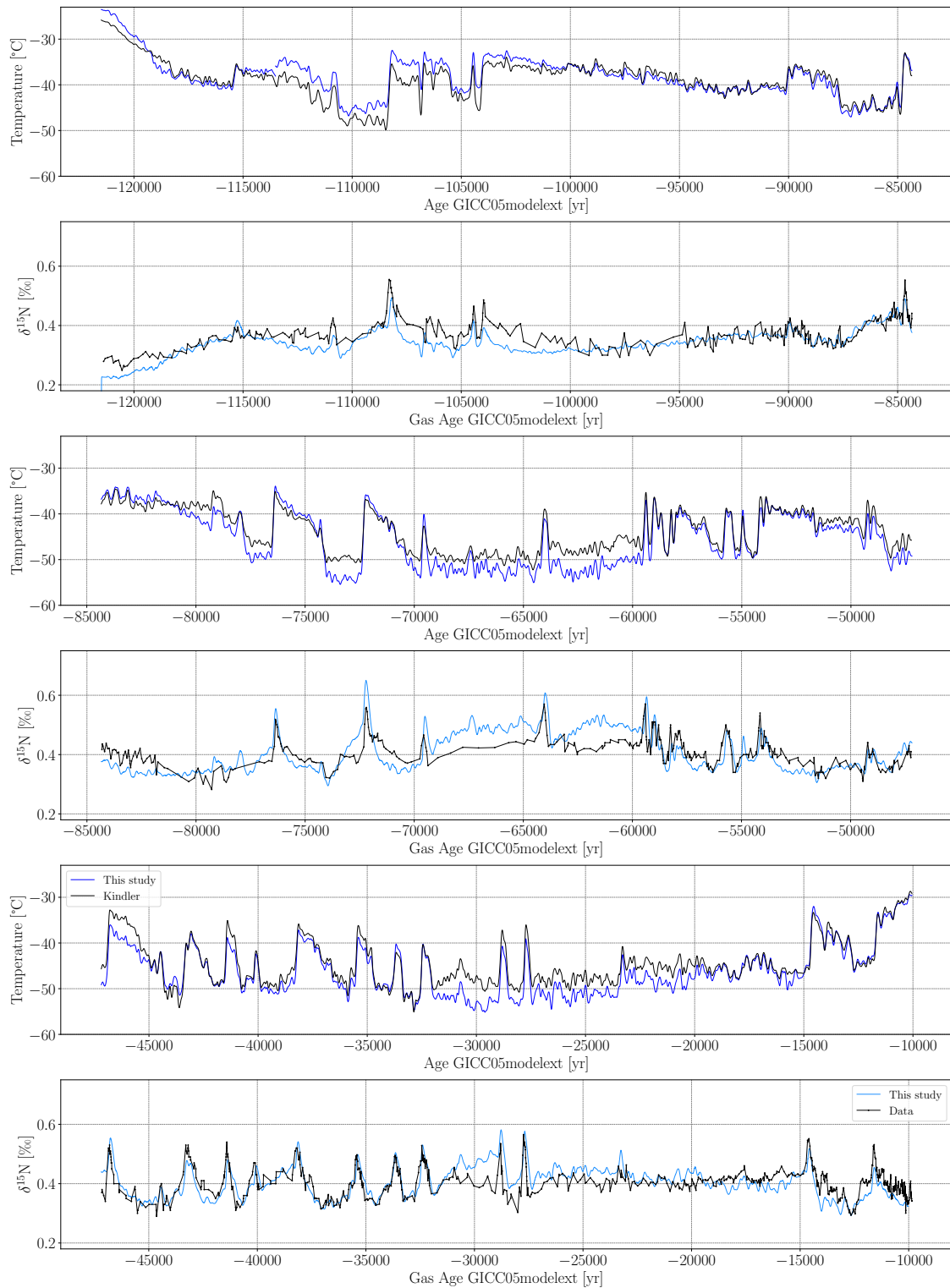
Figure 4.9: *Modeled $\delta^{15}N$ and reconstructed temperatures from an optimization run with randomly selected firn models for each iteration step.*

Chapter 5

Conclusion and Outlook

This final chapter sums up the results of this project and will give a short outlook for further experiments and improvements of the developed methodology.

During this project, the architecture of the CFM was investigated in detail with focus on firn densification and firn air diffusion.
One aim of this project was to identify bottlenecks of the model and to optimize model run times to make an inversion of the CFM more feasible. The `solver.py` module was identified as the main bottleneck of the CFM. It solves the heat diffusion differential equation and the firn air transport equation according to a numerical approach presented in [73]. The most time consuming function in `solver.py` is `w()` which calculates the firn air advection rate. Run times of `w()` vary for each time step iteration in the CFM and depend on the number of firn boxes in the model grid between the surface of the ice sheet and the lock-in depth of the firn column at the respective time step. Run times could not be improved by using the just-in-time compiler Numba. Instead, run times were decreased by a factor of 2 by reducing the grid length of the model by using 2 yr time steps instead of yearly time steps. Uncertainties in δ^{15}N resulting from this time resolution reduction lie within the measuring uncertainty of δ^{15}N (0.006 ‰ and 0.02 ‰, respectively). In addition, by introducing a second spin run, some time could be saved during the inversion procedure.
The CFM was inverted with the commonly used open-source least squares and Nelder-Mead algorithms provided by SciPy. The two algorithms often found differing parameters α and β which resulted however in most cases in an equally well solution in terms of cost function and mean mismatch. Nonetheless, the Nelder-Mead algorithm is more prone to bad fitting in time intervals with sparse measured δ^{15}N data which could be overcome by giving sparse data points a higher weight when calculating the cost function.
The presented inversion approach shows that the whole data set can be fit by using a single however not unique set of α and β with mean mismatches slightly worse than those calculated in [1] and [24]. However, similar results were achieved within the short time interval presented in [24] for the firn densification model according to Barnola.
The CFM was run using a set of four different firn densification models and four different gas diffusion models in order to investigate how reconstructed temperatures are affected by the firn model choice and to possibly evaluate how well the presented models are suited to model δ^{15}N at NorthGRIP.

The best performing inversion was achieved using the Barnola model, closely followed by Goujon and then Herron and Langway with Sigfus formulation. The optimization performed worst using the firn densification model according to Herron and Langway. From this finding it could be concluded that the Barnola model is the most suitable to describe firn physics at NorthGRIP.

All mean mismatches are higher than the uncertainty from measured stable nitrogen isotopes which is expected since only a single pair of α and β is used to fit the whole time interval between $-122\,000\,\text{yr}$ and $-10\,000\,\text{yr}$. Modeled $\delta^{15}\text{N}$ for different models also often differ from each other which makes it more difficult to draw conclusions on the temperature sensitivity with respect to the choice of firn model. However, for some model runs as presented in Figure 4.5 modeled $\delta^{15}\text{N}$ for different firn densification models are quite similar: from this it could be seen that the firn densification model according to Goujon expects by up to $3.5\,\text{K}$ lower temperatures than the other densification models. Reconstructed temperatures using Goujon are even up to $8\,\text{K}$ lower than the ones reconstructed by [1]. This means the choice of firn model has a notable influence on reconstructed surface temperatures which is worth further investigations.

The presented approaches allowed for an evaluation of how suitable different firn densification models are to reconstruct temperatures at NorthGRIP and how the choice of firn model influences the reconstructed temperatures. For future experiments it is important to enhance the performance of the fit of modeled to measured $\delta^{15}\text{N}$ which could be achieved by several approaches.

By using a shifting window spanning only short time intervals as also presented in [24] better fits within these time intervals could be obtained leading to a set of different parameters α_i and β_i for each window i. This would also better reflect the fact that the slope α changes over time.

The results could be further improved by using higher polynomials of $\delta^{18}\text{O}$ for temperature calculations and an additional parameter for the snow accumulation rate allowing for additional degrees of freedom for the solution.

Additional constraints on temperature could be set by modeling stable argon isotopes which is also possible with the CFM. Since thermal diffusivities for nitrogen and argon are different temperature gradients can be inferred from $\delta^{15}\text{N}$ and $\delta^{40}\text{Ar}$ which requires however a high precision of measured stable isotope ratios.

A more sophisticated approach would be to perform a Monte Carlo inversion as presented in [24] which allows for a temperature reconstruction completely independent of stable oxygen isotopes from water molecules in ice and thus overcomes the issue of inferring temperatures from non-temperature related signatures in $\delta^{18}\text{O}$.

In order to better understand which firn models are suitable for which ice core site it should be anticipated to perform the presented experiments also for other ice core drilling sites.

Appendix A

Configuration Files for the CFM

Most important parameters and comments on parameters in the configuartion .json file:

- `physRho` specifies the physics used for the calculation of firn densification. It is possible to select out of 13 different firn densification models. In the experiments presented here, the dynamic Herron and Langway firn densification model was used (`"HLdynamic"`).

- `TWriteInt` and `TWriteStart` denote the output time interval and the first time step to be written to the output file.

- `HeatDiff` is set to `True` in order to include heat diffusion. The `conductivity` option allows for the selection out of 13 different parameterizations for heat conductivity. The conductivity was set to `"Schwander"`.

- `yearSpin` is the period of time in years for the spin-up.

- `H` is the thickness of the ice sheet and `HbaseSpin` denotes the bottom depth of the modeled volume.

- `stpsPerYearSpin` and `stpsPerYear` are the number of time steps per year to be done during spin up and the actual model run.

- `grid_outputs` determined whether the model outputs are put on an equally spaced grid or not. `grid_outputs` was set to `False`.

- `spinup_climate_type` denotes whether the spin-up uses the first value (`"initial"`) or mean value (`"mean"`) of the input temperature and accumulation forcing files. It was set to `"initial"`.

- `no_densification` was set to `False` since the densification was supposed to be simulated.

- `FirnAir` was set to `True`. This runs the firn air module which uses also a .json configuration file (AirConfig.json)

- `outputs` specifies the model outputs. [`"density"`, `"depth"`, `"temperature"`, `"age"`, `"climate"`, `"BCO"`, `"isotopes"`] were selected. Note: The first column

of the output array is the model time. The initial model time value was originally set to -9999 in the CFM, this was changed to the initial model time step (first time step entry in the forcing files).

The parameters in the firn air configuration file were chosen as follows:

- `gaschoice` was set to `["d15N2", "d40Ar"]` in order to simulate δ^{15}N and δ^{40}Ar signals.

- `gravity` and `thermal` denote gravitational and thermal diffusion and were both set to `"on"`.

- `runtype` was set to `"transient"`.

- `Diffu_param` were calculated according to `"Schwander"`.

Appendix B

Model Outputs

Lock-in depth and close-off depth modeled with the CFM being forced with a temperature and snow accumulation rate history shown in Figure B.1(a). Lock-in depth and close-off depth are plotted to make sure that strong oscillations in δ^{15}N (Figure 3.8(c)) observed at ca. $-43\,000$ yr and $-41\,250$ yr each at the onset of a DO event are not due to a strong oscillation in lock-in depth.
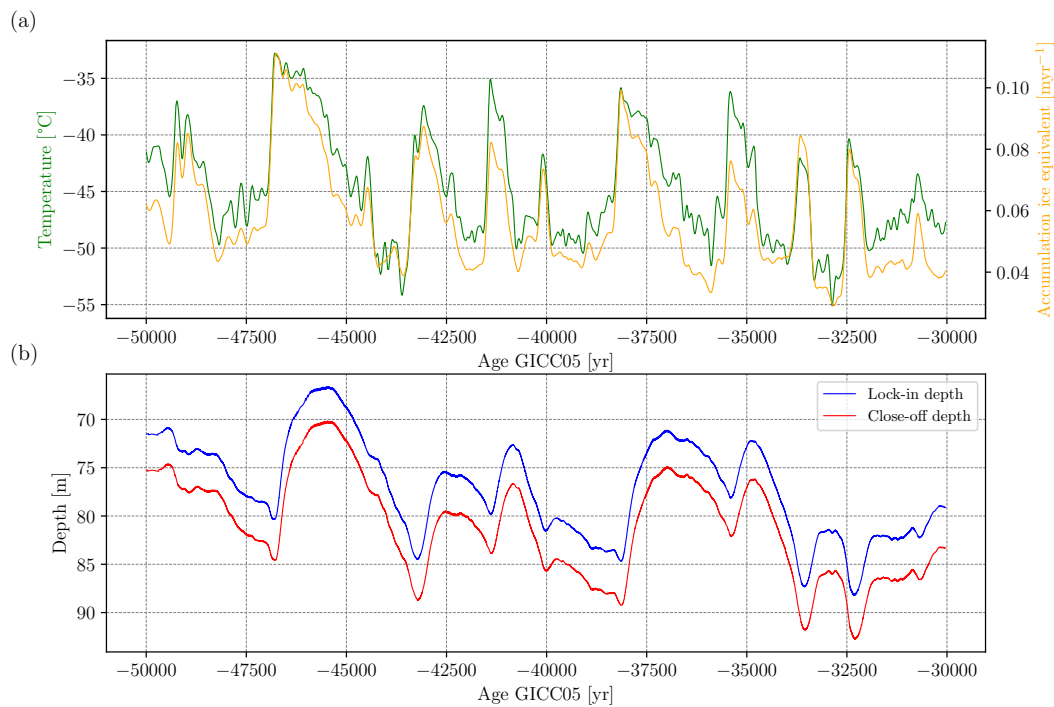
Figure B.1: *Lock-in depth and close-off depth modeled with the CFM.* *(a) Surface temperature and accumulation rate forcing (from Figure 3.3) for the CFM. (b) Lock-in depth and close-off depth plotted for each time step. No large in-continuities are present which could explain the strong oscillation of $\delta^{15}N$ in time intervals with a sudden and large jump in surface temperature as observed in Section 3.2.2.*

Appendix C

Comparison of firn models - Δage

δ^{15}N on ice age scale and Δages modeled with the CFM using two different minimizers (Nelder-Mead and least squares). In general, Δages roughly follow the trend of δ^{15}N - a sudden rise in δ^{15}N correlates with a rise in Δage. The values of δ^{15}N depend on the lock-in depth which is also correlated to Δage. A decrease in temperature leads to an increase of the lock-in depth and correlates with older ice/firn at lock-in depth and thus a higher Δage.
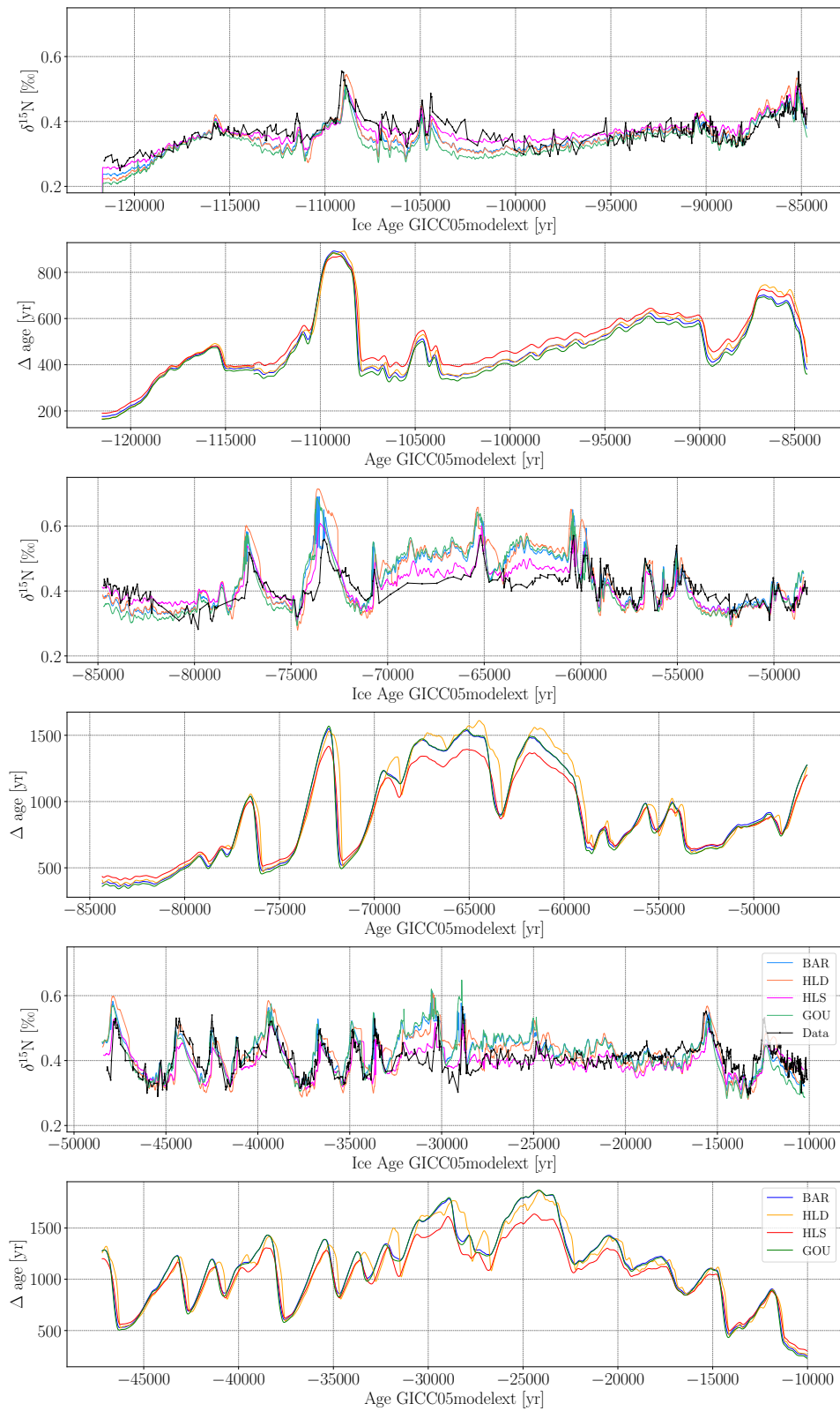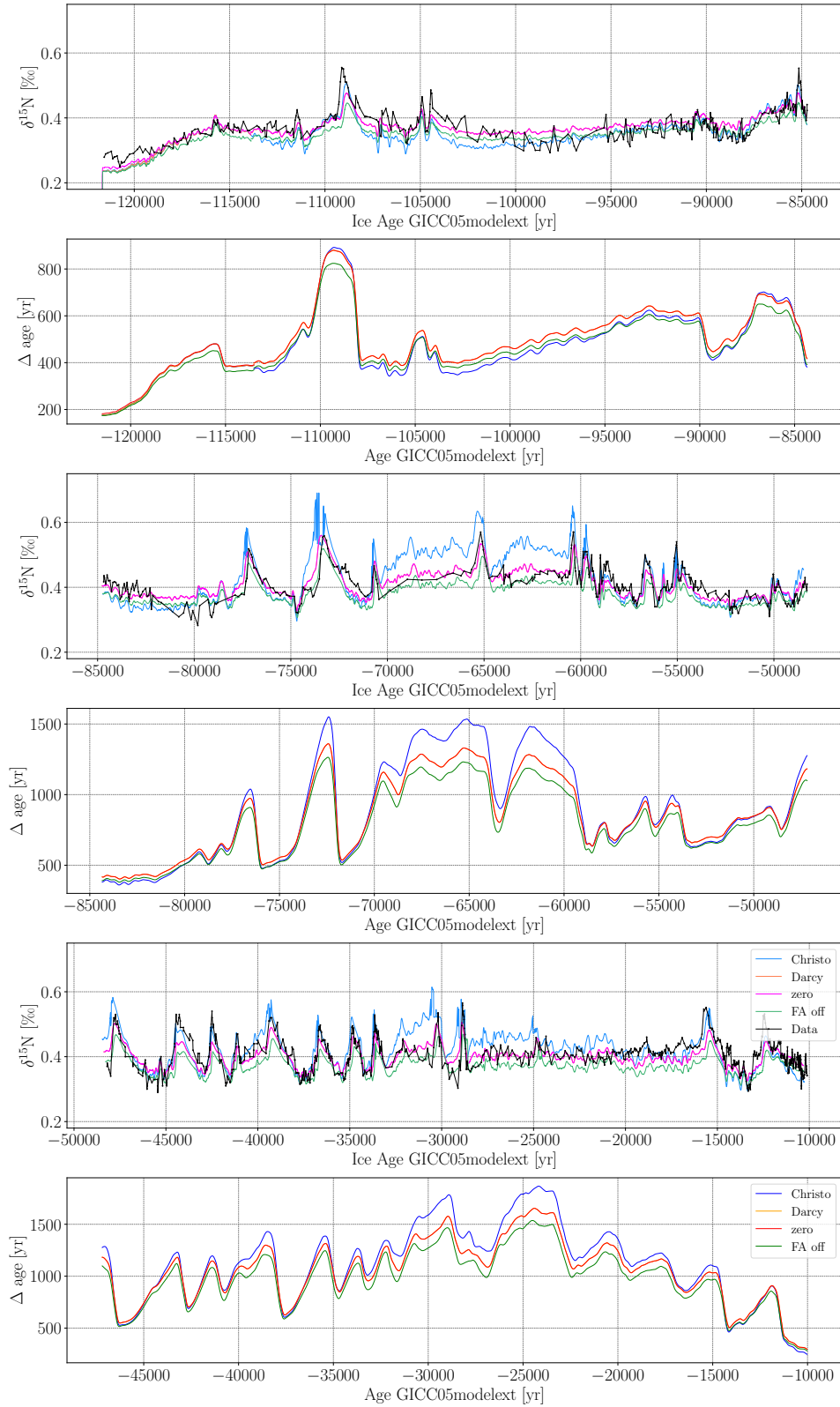
Figure C.1: *Reconstructed Δages for different densification models using the Nelder-Mead algorithm and corresponding $\delta^{15}N$ on ice age scale.*
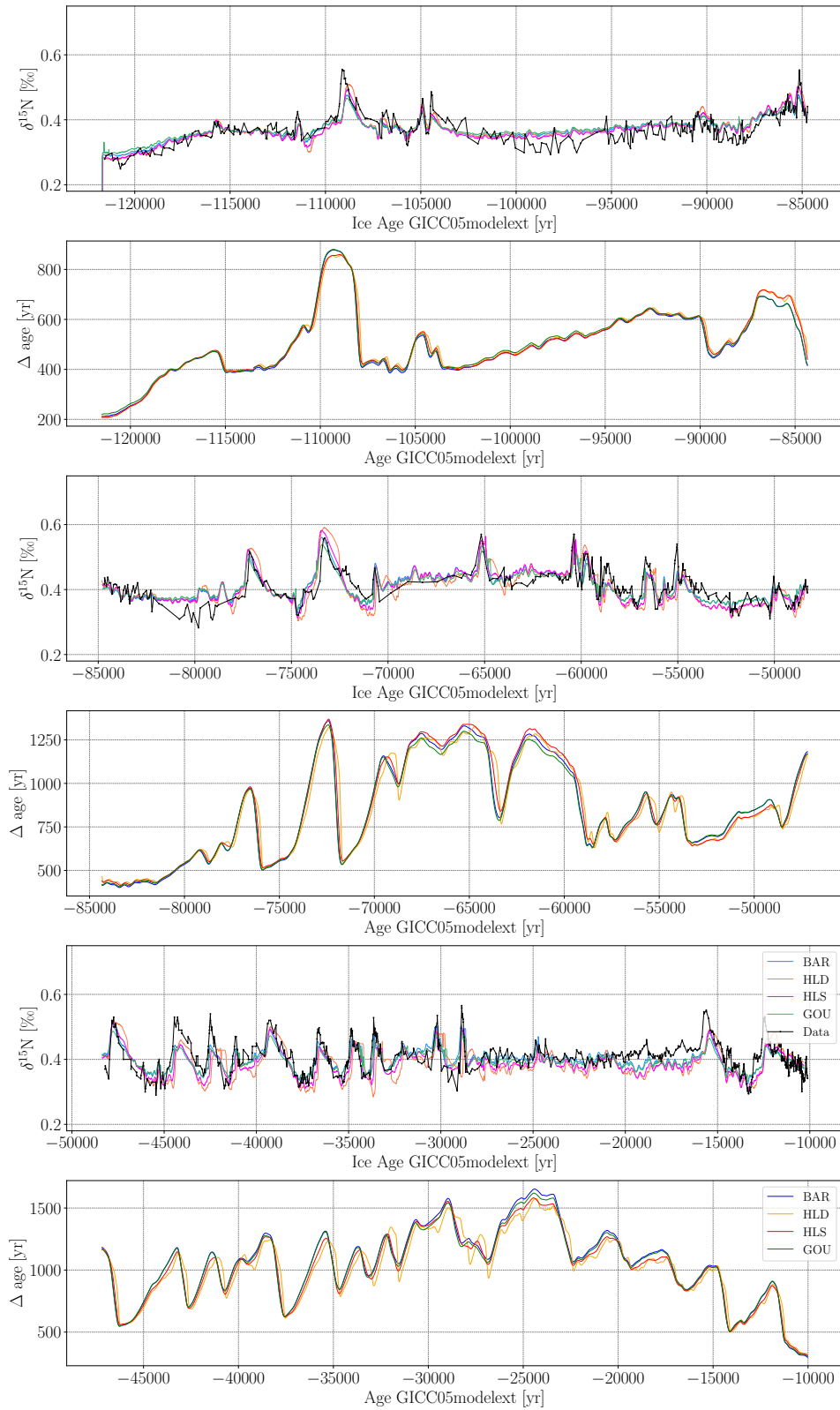
Figure C.2: *Reconstructed Δages for different densification models using the least squares algorithm and corresponding $\delta^{15}N$ on ice age scale.*

Figure C.3: *Reconstructed Δages for different gas diffusion models ("Christo"/"Darcy"/"zero": firn air diffusion module enabled with firn air advection according to Christo Buizert/ firn air advection according to Darcy/ no firn air advection; "FA off": firn air diffusion module disabled) using the Nelder-Mead algorithm and corresponding $\delta^{15}N$.*
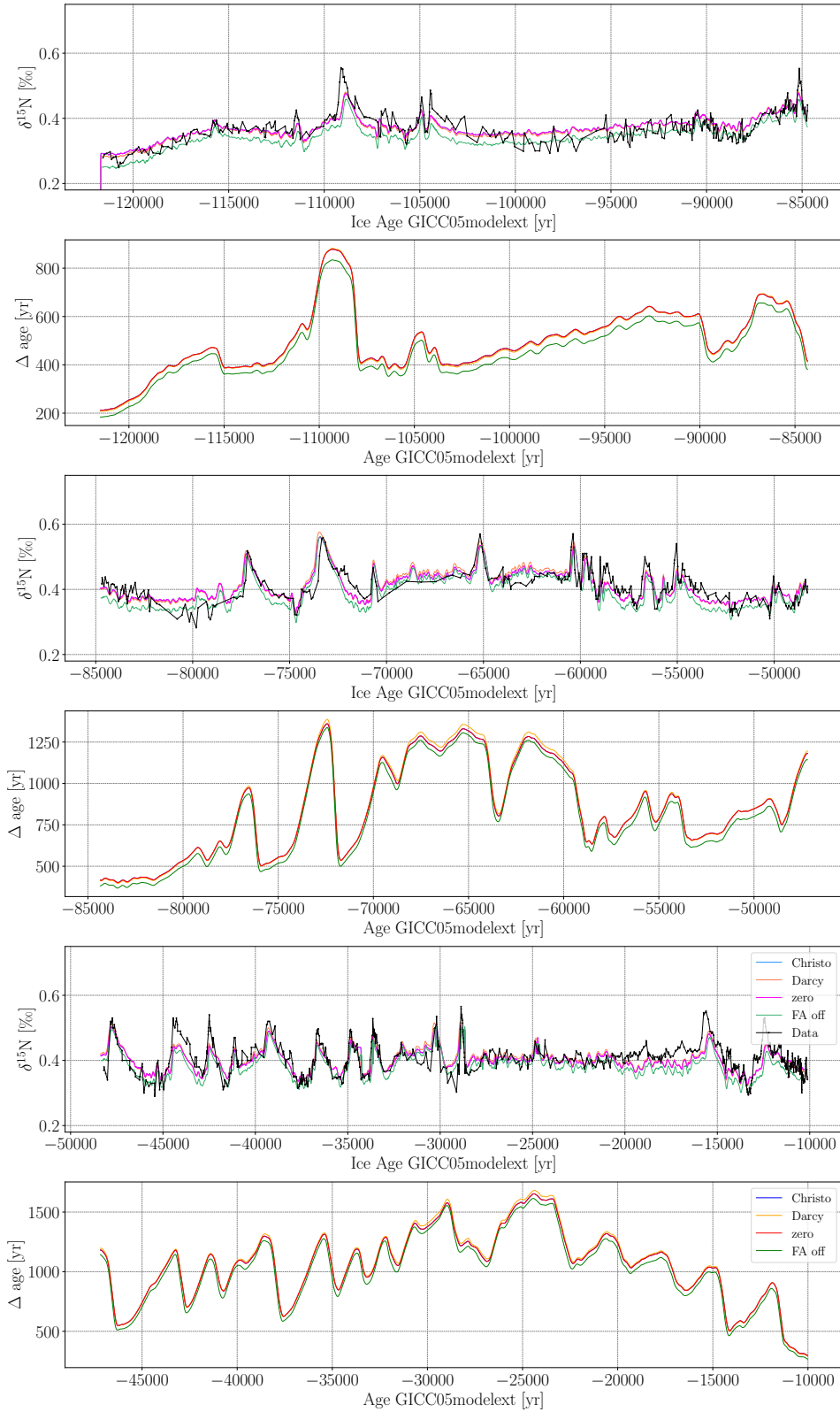
Figure C.4: *Reconstructed Δages for different gas diffusion models ("Christo"/"Darcy"/"zero": firn air diffusion module enabled with firn air advection according to Christo Buizert/ firn air advection according to Darcy/ no firn air advection; "FA off": firn air diffusion module disabled) using the least squares algorithm and corresponding $\delta^{15}N$.*

Appendix D

Pearson Correlation Coefficients

Scattterplots and Pearson correlation coefficients calculated from modeled and measured δ^{15}N in a time interval from $-38\,000\,\mathrm{yr}$ to $-31\,000\,\mathrm{yr}$.
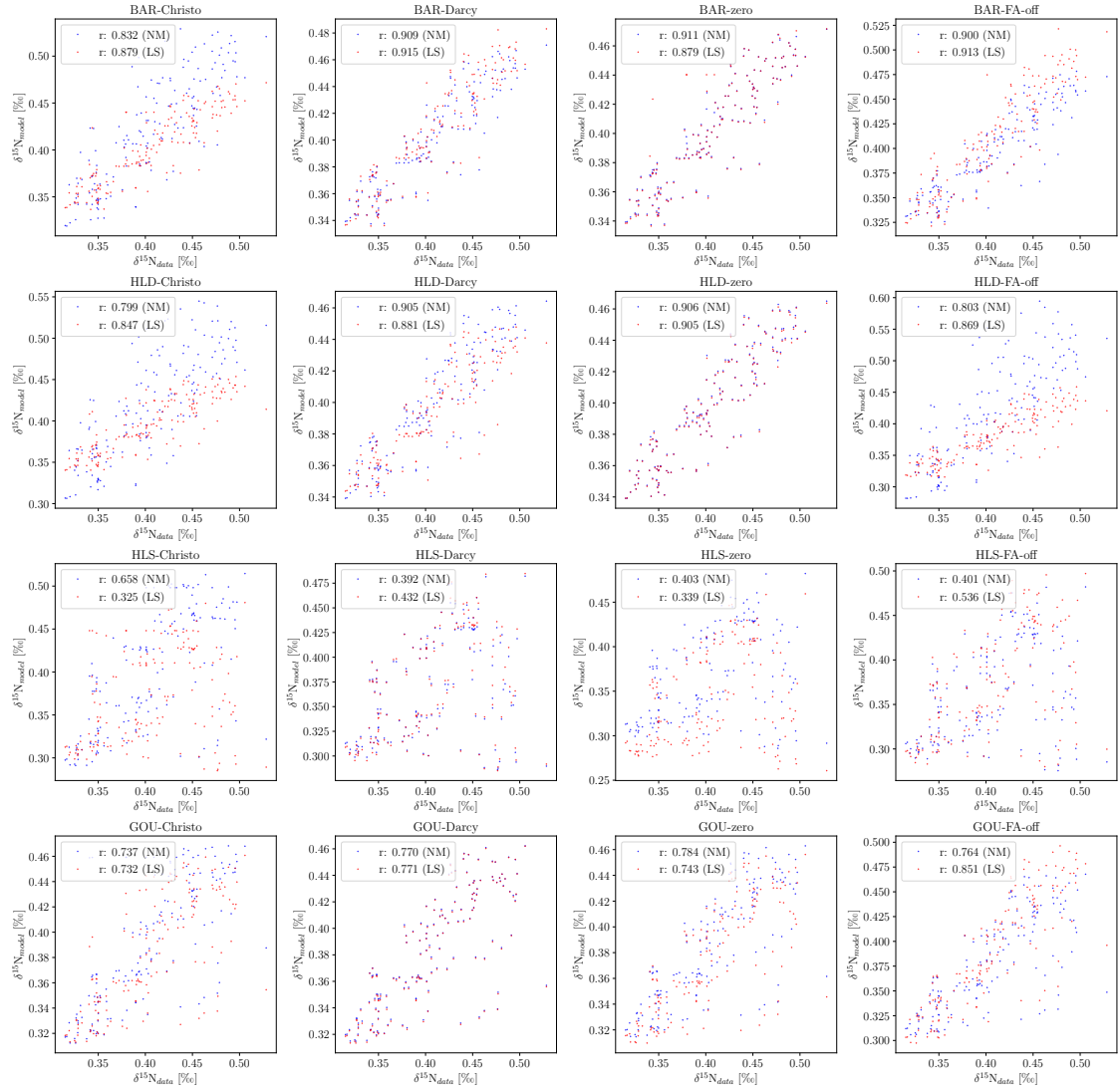
Figure D.1: *Scatterplot of measured and modeled $\delta^{15}N$ for different combinations of firn densification and gas diffusion models in a time interval from $-38\,000\,\mathrm{yr}$ to $-31\,000\,\mathrm{yr}$.*

Bibliography

[1] P. Kindler, M. Guillevic, M. Baumgartner, J. Schwander, A. Landais, and M. Leuenberger. Temperature reconstruction from 10 to 120 kyr b2k from the NGRIP ice core. *Climate of the Past*, 10(2):887–902, 2014.

[2] W. F. Ruddiman. *Earth's Climate: Past and Future*. W. H. Freeman and Company, New York, 3rd edition, 2014.

[3] J. D. Hays, J. Imbrie, and N. J. Shackleton. Variations in the earth's orbit: Pacemaker of the ice ages: For 500,000 years, major climatic changes have followed variations in obliquity and precession. *science*, 194(4270):1121–1132, 1976.

[4] J. Imbrie. Astronomical theory of the pleistocene ice ages: A brief historical review. *Icarus*, 50(2-3):408–422, 1982.

[5] J. L. Lean. Cycles and trends in solar irradiance and climate. *Wiley interdisciplinary reviews: climate change*, 1(1):111–122, 2010.

[6] A. Robock. Volcanic eruptions and climate. *Reviews of geophysics*, 38(2):191–219, 2000.

[7] J. Brugger, G. Feulner, and S. Petri. Baby, it's cold outside: Climate model simulations of the effects of the asteroid impact at the end of the cretaceous. *Geophysical Research Letters*, 44(1):419–427, 2017.

[8] W. F. Ruddiman, J. E. Kutzbach, and S. J. Vavrus. Can natural or anthropogenic explanations of late-holocene co2 and ch4 increases be falsified? *The Holocene*, 21(5):865–8879, 2011.

[9] S. J. Johnsen, D. Dahl-Jensen, N. Gundestrup, J. P. Steffensen, H. B. Clausen, H. Miller, V. Masson-Delmotte, A. E. Sveinbjörnsdottir, and J. White. Oxygen isotope and palaeotemperature records from six Greenland ice-core stations: Camp Century, Dye-3, GRIP, GISP2, Renland and NorthGRIP. *Journal of Quaternary Science: Published for the Quaternary Research Association*, 16(4):299–307, 2001.

[10] S. J. Johnsen, D. Dahl-Jensen, W. Dansgaard, and N. Gundestrup. Greenland palaeotemperatures derived from GRIP bore hole temperature and ice core isotope profiles. *Tellus B: Chemical and Physical Meteorology*, 47(5):624–629, 1995.

[11] K. M. Cuffey and G. D. Clow. Temperature, accumulation, and ice sheet elevation in central greenland through the last deglacial transition. *Journal of Geophysical Research: Oceans*, 102(C12):26383–26396, 1997.

[12] W. Dansgaard. Stable isotopes in precipitation. *Tellus*, 16(4):436–468, 1964.

[13] A. Mariotti. Atmospheric nitrogen is a reliable standard for natural 15N abundance measurements. *Nature*, 303:685–687, 1983.

[14] T. Sowers, M. Bender, and D. Raynaud. Elemental and isotopic composition of occluded O2 and N2 in polar ice. *Journal of Geophysical Research: Atmospheres*, 94(D4):5137–5150, 1989.

[15] M.C. Leuenberger, C. Lang, and J. Schwander. Delta 15N measurements as a calibration tool for the paleothermometer and gas-ice age differences: A case study for the 8200 B.P. event on GRIP ice. *Journal of Geophysical Research: Atmospheres*, 104(D18):22163–22170, 1999.

[16] H. Craig, Y. Horibe, and T. Sowers. Gravitational separation of gases and isotopes in polar ice caps. *Science*, 242(4886):1675–1678, 1988.

[17] R. Spahni, J. Schwander, J. Flückiger, B. Stauffer, J. Chappellaz, and D. Raynaud. The attenuation of fast atmospheric CH4 variations recorded in polar ice cores. *Geophysical Research Letters*, 30(11), 2003.

[18] S. Chapman and J. Larmor. The kinetic theory of simple and composite monatomic gases : viscosity, thermal conduction, and diffusion. *Proceedings of the Royal Society of London. Series A, Containing Papers of a Mathematical and Physical Character*, 93(646):1–20, 1916.

[19] S. Chapman and F.W. Dootson. XXII. a note on thermal diffusion. *The London, Edinburgh, and Dublin Philosophical Magazine and Journal of Science*, 33(195):248–253, 1917.

[20] J.P. Severinghaus, A. Grachev, and M. Battle. Thermal fractionation of air in polar firn by seasonal temperature gradients. *Geochemistry, Geophysics, Geoscience*, 2, 2001.

[21] C. Lang, M. Leuenberger, J. Schwander, and S. Johnsen. 16°C rapid temperature variation in central Greenland 70,000 years ago. *Science*, 286(5441):934–937, 1999.

[22] C. Huber, M. Leuenberger, R. Spahni, J. Flückiger, J. Schwander, T. F. Stocker, S. Johnsen, A. Landais, and J. Jouzel. Isotope calibrated Greenland temperature record over Marine Isotope Stage 3 and its relation to CH4. *Earth and Planetary Science Letters*, 243(3-4):504–519, 2006.

[23] A. J. Orsi, B. D. Cornuelle, and J. P. Severinghaus. Magnitude and temporal evolution of Dansgaard–Oeschger event 8 abrupt temperature change inferred from nitrogen and argon isotopes in GISP2 ice using a new least-squares inversion. *Earth and Planetary Science Letters*, 395:81–90, 2014.

[24] M. Döring. *Temperature reconstruction based on stable nitrogen and argon isotope measurements on Greenland ice cores*. PhD thesis, Universität Bern. Abteilung für Klima- und Umweltphysik, 2020.

[25] C.M. Stevens et al. The Community Firn Model (CFM) v1.0. *Geoscientific Model Development*, 13:4355–4377, 2020.

[26] C. Buizert. *Encyclopedia of Quaternary Science*, volume 2. Elsevier, Amsterdam, 2013.

[27] P. Martinerie, D. Raynaud, D.M. Etheridge, J. M. Barnola, and D. Mazaudier. Physical and climatic parameters which influence the air content in polar ice. *Earth and Planetary Science Letters*, 112(1):1–13, 1992.

[28] T. Blunier and J. Schwander. Gas enclosure in ice: age difference and fractionation. In *Physics of Ice Core Records*, pages 307–326. Hokkaido University Press, 2000.

[29] J. P. Severinghaus, Albert M. R., Z. R. Courville, et al. Deep air convection in the firn at a zero-accumulation site, Central Antarctica. *Earth and Planetary Science Letters*, 293(3):359–367, 2010.

[30] J. Schwander. *The Environmental Record in Glaciers and Ice Sheets*. Wiley, New York, 1989.

[31] P. Martinerie, V. Y. Lipenkov, D. Raynaud, J. Chappellaz, N. I. Barkov, and C. Lorius. Air content paleo record in the Vostok ice core (Antarctica): A mixed record of climatic and glaciological parameters. *Journal of Geophysical Research: Atmospheres*, 99(D5):10565–10576, 1994.

[32] M. M. Herron and C. C. Langway. Firn densification: An empirical model. *Journal of Glaciology*, 25(93):373–385, 1980.

[33] C. Goujon, J.-M. Barnola, and C. Ritz. Modeling the densification of polar firn including heat diffusion: Application to close-off characteristics and gas isotopic fractionation for Antarctica and Greenland sites. *Journal of Geophysical Research: Atmospheres*, 108(D24), 2003.

[34] J. M. Barnola, P. Pimienta, D. Raynaud, and Y. S. Korotkevich. CO2-climate relationship as deduced from the Vostok ice core: a re-examination based on new measurements and on a re-evaluation of the air dating. *Tellus B*, 43(2):83–90, 1991.

[35] P. Pimienta and P. Duval. Rate controlling processes in the creep of polar ice. *J. Phys. Colloques*, 48(C1):243–248, 1987.

[36] D. S. Wilkinson and M.F. Ashby. Pressure sintering by power law creep. *Acta Metallurgica*, 23(11):1277–1285, 1975.

[37] R.B. Alley. Firn densification by grain-boundary sliding: A first model. *J. Phys. Colloques*, 48(C1):C1–249–C1–256, 1987.

[38] E. Arzt. The influence of an increasing particle coordination on the densification of spherical powders. *Acta Metallurgica*, 30(10):1883–1890, 1982.

[39] L. Arnaud, J.M. Barnola, and P. Duval. Physical modeling of the densification of snow/firn and ice in the upper part of polar ice sheets. In *Physics of ice core records*, pages 285–305. Hokkaido University Press, 2000.

[40] J.P. Severinghaus and E.J. Brook. Abrupt climate change at the end of the last glacial period inferred from trapped air in polar ice. *Science*, 286(5441):930–934, 1999.

[41] S. Chapman and T.G. Cowling. *The Mathematical Theory of Non-uniform Gases - An Account of the Kinetic Theory of Viscosity, Thermal Conduction and Diffusion in Gases.* Cambridge University Press, 3rd edition, 1990.

[42] A. M. Grachev and J. P. Severinghaus. Laboratory determination of thermal diffusion constants for 29N2/28N2 in air at temperatures from −60 to 0°C for reconstruction of magnitudes of abrupt climate changes using the ice core fossil–air paleothermometer. *Geochimica et Cosmochimica Acta*, 67(3):345–360, 2003.

[43] J. Schwander, J. M. Barnola, C. Andrie, M. Leuenberger, A. Ludin, D. Raynaud, and B. Stauffer. The age of the air in the firn and the ice at Summit, Greenland. *Journal of Geophysical Research: Atmospheres*, 98(D2):2831–2838, 1993.

[44] C. M. Trudinger, I.G. Enting, D. M. Etheridge, R. J. Francey, V. A. Levchenko, L. P. Steele, D. Raynaud, and L. Arnaud. Modeling air movement and bubble trapping in firn. *Journal of Geophysical Research: Atmospheres*, 102(D6):6747–6763, 1997.

[45] J. P. Severinghaus and M. O. Battle. Fractionation of gases in polar ice during bubble close-off: New constraints from firn air Ne, Kr and Xe observations. *Earth and Planetary Science Letters*, 244(1-2):474–500, 2006.

[46] J. Schwander, B. Stauffer, and A. Sigg. Air mixing in firn and the age of the air at pore close-off. *Annals of Glaciology*, 10:141–145, 1988.

[47] C. M. Stevens, E.D. Waddington, H. Conway, and M. Koutnik. Investigations of physical processes in polar firn through modeling and field measurements, ProQuest Dissertations and Theses. 2018.

[48] C. Buizert. *The influence of firn air transport processes and radio-carbon production on gas records from polar firn and ice.* PhD thesis, Københavns Universitet. Niels Bohr Institutet, 2011.

[49] C. Buizert and J. P. Severinghaus. Dispersion in deep polar firn driven by synoptic-scale surface pressure variability. *The Cryosphere*, 10(5):2099–2111, 2016.

[50] D. Dahl-Jensen and S. J. Johnsen. Palaeotemperatures still exist in the Greenland ice sheet. *Nature*, 320(6059):250–252, 1986.

[51] Z. Sharp. *Principles of Stable Isotope Geochemistry.* Pearson Prentice Hall, New Jersey, 1st edition, 2000.

[52] J. Jouzel, F. Vimeux, N. Caillon, G. Delaygue, G. Hoffmann, V. Masson-Delmotte, and F. Parrenin. Magnitude of isotope/temperature scaling for interpretation of Central Antarctic ice cores. *Journal of Geophysical Research: Atmospheres*, 108(D12), 2003.

[53] C. Buizert, T. J. Fudge, William H. G. Roberts, E. J. Steig, S. Sherriff-Tadano, C. Ritz, E. Lefebvre, J. Edwards, K. Kawamura, I. Oyabu, H. Motoyama, E. C. Kahle, T. R.

Jones, A. Abe-Ouchi, T. Obase, C. Martin, H. Corr, J. P. Severinghaus, R. Beaudette, J. A. Epifanio, E. J. Brook, K. Martin, J. Chappellaz, S. Aoki, T. Nakazawa, T. A. Sowers, R. B. Alley, J. Ahn, M. Sigl, M. Severi, N. W. Dunbar, A. Svensson, J. M. Fegyveresi, C. He, Z. Liu, J. Zhu, B. L. Otto-Bliesner, V. Y. Lipenkov, M. Kageyama, and J. Schwander. Antarctic surface temperature and elevation during the Last Glacial Maximum. *Science*, 372(6546):1097–1101, 2021.

[54] P. Virtanen, R. Gommers, T. E. Oliphant, M. Haberland, T. Reddy, D. Cournapeau, E. Burovski, P. Peterson, W. Weckesser, J. Bright, Stéfan J. van der Walt, M. Brett, J. Wilson, K. J. Millman, N. Mayorov, Andrew R. J. Nelson, E. Jones, R. Kern, E. Larson, C. J. Carey, İ. Polat, Y. Feng, E. W. Moore, J. VanderPlas, D. Laxalde, J. Perktold, R. Cimrman, I. Henriksen, E. A. Quintero, C. R. Harris, A. M. Archibald, A. H. Ribeiro, F. Pedregosa, P. van Mulbregt, and SciPy 1.0 Contributors. SciPy 1.0: Fundamental Algorithms for Scientific Computing in Python. *Nature Methods*, 17:261–272, 2020.

[55] M. Chen. Stats 102A lesson 8-2 Nelder Mead method / Algorithm. `https://www.you tube.com/watch?v=vOYlVvT3W8o`, 2021. Last accessed: 2022-07-25.

[56] J. A. Nelder and R. Mead. A simplex method for function minimization. *The computer journal*, 7(4):308–313, 1965.

[57] P. Poupart. Cs885 Lecture 14c: Trust Region Methods. `https://www.youtube.com /watch?v=qaOKZkeutqE&t=616s`, 2018. Last accessed: 2022-07-26.

[58] C.T. Kelley. *Iterative Methods for Optimization*. Society for Industrial and Applied Mathematics, 1999.

[59] B. M. Vinther, H. B. Clausen, S. J. Johnsen, S. Ol. Rasmussen, K. K. Andersen, S. L. Buchardt, D. Dahl-Jensen, I. K. Seierstad, M.-L. Siggaard-Andersen, J. P. Steffensen, et al. A synchronized dating of three Greenland ice cores throughout the Holocene. *Journal of Geophysical Research: Atmospheres*, 111(D13), 2006.

[60] S. O. Rasmussen, K. K. Andersen, A. M. Svensson, J. P. Steffensen, B. M. Vinther, H. B. Clausen, M.-L. Siggaard-Andersen, S. J. Johnsen, L. B. Larsen, D. Dahl-Jensen, et al. A new Greenland ice core chronology for the last glacial termination. *Journal of Geophysical Research: Atmospheres*, 111(D6), 2006.

[61] K. K. Andersen, A. Svensson, S. J. Johnsen, S. O. Rasmussen, M. Bigler, R. Röthlisberger, U. Ruth, M.-L. Siggaard-Andersen, J. P. Steffensen, D. Dahl-Jensen, et al. The Greenland ice core chronology 2005, 15–42 ka. Part 1: constructing the time scale. *Quaternary Science Reviews*, 25(23-24):3246–3257, 2006.

[62] A. Svensson, K. K. Andersen, M. Bigler, H. B. Clausen, D. Dahl-Jensen, S. M. Davies, S. J. Johnsen, R. Muscheler, F. Parrenin, S. O. Rasmussen, et al. A 60 000 year Greenland stratigraphic ice core chronology. *Climate of the Past*, 4(1):47–57, 2008.

[63] E. W. Wolff, J. Chappellaz, T. Blunier, S. O. Rasmussen, and A. Svensson. Millennial-scale variability during the last glacial: The ice core record. *Quaternary Science Reviews*, 29(21-22):2828–2838, 2010.

[64] A. Landais, J. Jouzel, V. Masson-Delmotte, and N. Caillon. Large temperature variations over rapid climatic events in Greenland: a method based on air isotopic measurements. *Comptes Rendus Geoscience*, 337(10-11):947–956, 2005.

[65] A. Landais, J. M. Barnola, V. Masson-Delmotte, J. Jouzel, J. Chappellaz, N. Caillon, C. Huber, M. Leuenberger, and S. J. Johnsen. A continuous record of temperature evolution over a sequence of Dansgaard-Oeschger events during Marine Isotopic Stage 4 (76 to 62 kyr BP). *Geophysical Research Letters*, 31(22), 2004.

[66] E. Capron, A. Landais, J. Chappellaz, D. Buiron, H. Fischer, S. J. Johnsen, J. Jouzel, M. Leuenberger, V. Masson-Delmotte, and T. F. Stocker. A global picture of the first abrupt climatic event occurring during the last glacial inception. *Geophysical Research Letters*, 39(15), 2012.

[67] E. Capron, A. Landais, B. Lemieux-Dudon, A. Schilt, V. Masson-Delmotte, D. Buiron, J. Chappellaz, D. Dahl-Jensen, S. Johnsen, M. Leuenberger, et al. Synchronising EDML and NorthGRIP ice cores using δ18O of atmospheric oxygen (δ18Oatm) and CH4 measurements over MIS5 (80–123 kyr). *Quaternary Science Reviews*, 29(1-2):222–234, 2010.

[68] E. Capron, A. Landais, J. Chappellaz, A. Schilt, D. Buiron, D. Dahl-Jensen, S. J. Johnsen, J. Jouzel, B. Lemieux-Dudon, L. Loulergue, et al. Millennial and sub-millennial scale climatic variations recorded in polar ice cores over the last glacial period. *Climate of the Past*, 6(3):345–365, 2010.

[69] Centre for Ice and Climate. Data, icesamples and software. `https://www.iceandclimate.nbi.ku.dk/data`. Last accessed: 2022-07-10.

[70] E. Prilepin. CSAPS – Cubic Spline Approximation (Smoothing). `https://csaps.readthedocs.io/en/latest/`, 2020. Last accessed: 2022-07-27.

[71] I. G. Enting. On the use of smoothing splines to filter CO2 data. *Journal of Geophysical Research: Atmospheres*, 92(D9):10977–10984, 1987.

[72] V. Gkinis, C. Holme, E. C. Kahle, M. C. Stevens, E. J. Steig, and B. M. Vinther. Numerical experiments on firn isotope diffusion with the Community Firn Model. *Journal of Glaciology*, 67(263):450–472, 2021.

[73] S.V. Patankar. *Series in computational methods in mechanics and thermal sciences.* Hemisphere Publishing Corporation, 1st edition, 1980.

[74] V. Verjans, A. A. Leeson, C. M. Stevens, M. MacFerrin, B. Noël, and M. R. van den Broeke. Development of physically based liquid water schemes for Greenland firn-densification models. *The Cryosphere*, 13(7):1819–1842, 2019.

[75] V. R. Voller, C. R. Swaminathan, and B. G. Thomas. Fixed grid techniques for phase change problems: a review. *International journal for numerical methods in engineering*, 30(4):875–898, 1990.

[76] N. Calonne, L. Milliancourt, A. Burr, A. Philip, C. L. Martin, F. Flin, and C. Geindreau. Thermal conductivity of snow, firn, and porous ice from 3-d image-based computations. *Geophysical Research Letters*, 46(22):13079–13089, 2019.

[77] R. Patwardhan. CPU vs. GPU - best use cases for each. `https://www.weka.io/blog/cpu-vs-gpu/`, 2021. Accessed: 2022-07-13.

[78] Anaconda. Numba: A high performance Python compiler. `https://numba.pydata.org/`, 2018. Last accessed: 2022-07-16.

[79] Continuum Analytics. Numba 0.12.02 documentation. `https://numba.pydata.org/numba-doc/0.12.2/tutorial_types.html`, 2014. Last accessed: 2022-07-16.

[80] Python Software Foundation. time — time access and conversions. `https://docs.python.org/3/library/time.html`, 2022. Last accessed: 2022-07-19.

[81] The SciPy community. scipy.stats.pearsonr; SciPy v1.9.0 Manual. `https://docs.scipy.org/doc/scipy/reference/generated/scipy.stats.pearsonr.html`, 2022. Last accessed: 2022-08-06.

[82] M. Döring and M. C. Leuenberger. Novel automated inversion algorithm for temperature reconstruction using gas isotopes from ice cores. *Climate of the Past*, 14(6):763–788, 2018.

[83] J. Schwander, T. Sowers, J.-M. Barnola, T. Blunier, A. Fuchs, and B. Malaizé. Age scale of the air in the summit ice: Implication for glacial-interglacial temperature change. *Journal of Geophysical Research: Atmospheres*, 102(D16):19483–19493, 1997.